Stellar Motion
Near the Supermassive Black Hole in the Galactic Center

INAUGURAL-DISSERTATION

zur
Erlangung des Doktorgrades
der Mathematisch-Naturwissenschaftlichen Fakultät
der Universität zu Köln

vorgelegt von

Marzieh Parsa
aus Shiraz, Iran

Köln 2018

Berichterstatter:	Prof. Dr. Andreas Eckart Prof. Dr. J. Anton Zensus
Tag der mündlichen Prüfung:	10. Oktober 2017

Abstract

General relativity is the least tested theory of physics. The close environment of the supermassive black hole provides us with the perfect laboratory for the investigation of the predictions of this theory. Therefore, the Observation of S-stars in the Galactic center in the near-infrared wavelengths provides the opportunity to study the physics in the vicinity of a supermassive black hole and conduct unique dynamical tests of the theory of general relativity.

In my thesis, I use near-infrared high angular resolution adaptive optics images of the central stellar cluster acquired with the NACO instrument at the Very Large Telescope of the European Southern Observatory, from 2002 to 2015. In addition, I employ the published astrometric and line of sight velocity data obtained with the Keck telescope from 1995 to 2013.

I use the SiO maser sources in the wide field of view of the NACO S27 camera. The positions and motions of these maser sources and the position of Sgr A*, the supermassive black hole in the center of the Galaxy, is known in the radio regime. Therefore, I find the connection between the near-infrared data and the radio reference frame. Next, I connect the images of the S27 camera to the images of the S13 camera, in which the S-stars are observable in the central arcsecond, using six overlap stars. Moreover, I use the linear motion of five isolated S-stars to overcome the small distortion in the images of NACO. Then I focus on the three stars known to have the shortest orbital periods, i.e., S2, S38, and S0-102 (also known as S55). I extract the astrometric positions of these three stars in the near-infrared reference frame. Using the astrometric and radial velocity data, I calculate their six Keplerian orbital elements and the gravitational potential parameters of Sgr A*, simultaneously. To calculate the orbits, I apply the fourth-order Runge-Kutta integration technique on equations of motion with both the Newtonian and first-order post-Newtonian relativistic models. I use a minimum χ^2 method for the fitting procedure and evaluate the uncertainties by the Markov Chain Monte Carlo technique. The important results from the procedure are an estimate of the central mass of $M_{BH} = (4.15 \pm 0.13 \pm 0.57) \times 10^6\ M_\odot$ and the distance to the Galactic center of $R_0 = 8.19 \pm 0.11 \pm 0.34$ kpc.

In addition, since S2 is on an orbit with a short orbital period and a large eccentricity, it motivates me to develop a practical method to probe the general relativistic effects introduced by the strong gravitational potential of the supermassive black hole. I find a correlation between the deviation of a relativistic orbit from a Keplerian one and a suitable relativistic parameter. I choose the relativistic parameter $\Upsilon \equiv r_s/r_p$, with r_s being the Schwarzschild radius of the black hole and r_p the impact parameter, i.e., the closest approach. The deviation of a first-order post-Newtonian orbit from a Keplerian one can be seen as the changes of orbital

parameters, such as the semimajor axis, eccentricity, and the argument of periapse. The semimajor axis and eccentricity change when comparing the upper and lower halves of the orbit, and the argument of periapse changes when comparing the pre- and post-periapse halves of the orbit. To find the correlation, I use a first-order post-Newtonian approximation to simulate the orbits of several stars with a wide range of periapse distances lying inside the orbit of S2. The found correlation is then applied on S2.

For the orbit of S2, with the mass of the black hole and the orbital parameters calculated previously, I expect a relativistic parameter of $\Upsilon = 0.00065$ from theory. Using this new method, I find a value of $\Upsilon = 0.00088 \pm 0.00080$, which is within the uncertainty in agreement with the expected theoretical value. Moreover, for the variations in the argument of periapse of S2, I find $\Delta\omega = 14' \pm 7'$, which agrees with the theoretical periapse shift of $11'$. Finally, I rule out any other perturbing effect that could generate the similar results, such as the noise on the stellar positions, rotation of the image, or the drifts of the black hole. My analysis shows for the first time that the subtle effects predicted by general relativity on the orbits of stars close to the supermassive black hole, can be obtained from our current observations. S2 is the first star on an orbit around a supermassive black hole for which a post-Newtonian effect has been measured.

Zusammenfassung

Die Allgemeine Relativitätstheorie ist die am wenigsten getestete Theorie der Physik. Die nächste Umgebung eines supermassiven schwarzen Lochs bietet den perfekten Ort um die Vorhersagen der Allgemeinen Relativitätstheorie auf die Probe zu stellen. Daher eröffnet die Beobachtung der im Zentrum der Milchstraße befindlichen S-Sterne, im nahen infraroten Wellenlängenbereich, die Möglichkeit die Physik in der nächsten Umgebung eines supermassiven schwarzen Lochs zu erforschen und somit einzigartige Tests der Allgemeinen Relativitätstheorie durchzuführen.

In meiner Dissertation verwende ich durch die adaptive Optik hoch aufgelöste Bilder des zentralen Sternenclusters, aufgenommen im Zeitraum von 2002 bis 2015 im nahen Infrarot mit dem Instrument NACO der Europäischen Südsternwarte am Very Large Telescope. Zusätzlich verwende ich veröffentlichte astrometrische und Radialgeschwindigkeitsdaten, die mit dem Keck Teleskop im Zeitraum von 1995 bis 2003 aufgenommen wurden.

Ich konzentriere mich auf die drei Sterne mit den kürzesten bekannten Umlaufperioden, d.h., S2, S38 und S0-102 (auch bekannt als S55). Ich extrahiere die astrometrischen Positionen dieser drei Sterne im nahen infraroten Referenzbild. Ich verwende die SiO Maser-Quellen, die sich im großen Gesichtsfeld der NACO S27 Kamera befinden. Die Positionen und Bewegungen dieser Maser-Quellen und die Position von Sgr A*, dem supermassiven schwarzen Loch im Zentrum der Galaxie, sind im Radiobereich bekannt. Auf diese Weise finde ich eine Verknüpfung zwischen den Daten im nahen Infrarot und dem Radio Referenzbild. Danach verknüpfe ich die Bilder der Kamera S27 mit denen der Kamera S13, auf welcher die S-Sterne in der zentralen Bogensekunde beobachtbar sind, indem ich sechs Sterne übereinander positioniere. Des Weiteren verwende ich die Linearbewegung von fünf isolierten S-Sternen um für die geringe Verzerrung der NACO-Bilder korrigieren zu können. Unter Verwendung der astrometrischen und Radialgeschwindigkeitsdaten von S2, S38 und S0-102 bestimme ich gleichzeitig deren sechs Kepler-Umlaufbahn-Elemente und die Parameter zur Beschreibung des Gravitationspotentials des supermassiven schwarzen Lochs Sgr A*, in welchem sich der S-Sternhaufen befindet. Zur Berechnung der Umflaufbahnen wende ich die Runge-Kutta Integrationstechnik vierter Ordnung auf die Bewegungsgleichung an, sowohl mit Newtonschen als auch post-Newtonschen relativistischen Modellen erster Ordnung. Die Fitprozedur wird mit der Minimum-χ^2-Methode durchgeführt und die Ungenauigkeiten werden mit Hilfe der Markov Chain Monte Carlo Technik bestimmt. Die wichtigen Ergebnisse dieser Prozedur sind die Abschätzung der zentralen Masse $M_{BH} = (4.15 \pm 0.13 \pm 0.57) \times 10^6\ M_\odot$ und die Entfernung zum Galaktischen Zentrum $R_0 = 8.19 \pm 0.11 \pm 0.34$ kpc.

Die Tatsache, dass S2 sich auf einer Umlaufbahn mit kurzer Umlaufperiode und

hoher Exzentrizität befindet, motiviert mich dazu eine neuartige und praktische Methode zum Erproben der Effekte der Allgemeinen Relativitätstheorie starker Gravitationspotentiale zu entwickeln. Mein Ziel ist es, eine Korrelation zwischen der Abweichung der relativistischen Umlaufbahnen zu den Kepler-Umlaufbahnen und einem relativistischen Parameter zu finden. Hierzu wähle ich den relativistischen Parameter $\Upsilon \equiv r_s/r_p$, wobei r_s der Schwarzschildradius des schwarzen Lochs und r_p der Stoßparameter ist. Die Abweichung einer post-Newtonschen Umlaufbahn erster Ordnung von einer Keplerschen Umlaufbahn kann als Änderung der Umlaufbahnparamter, wie der großen Halbachse, der Exzentrizität und des Arguments der Periapsis angesehen werden. Die große Halbachse und die Exzentrizität ändern sich bei Vergleich der oberen und unteren Hälfte der Umlaufbahn, und das Argument der Periapsis ändert sich, wenn die vor- und nach-Periapsis Hälften der Umlaufbahn verglichen werden. Zur Bestimmung der Korrelation verwende ich eine post-Newtonsche Näherung erster Ordnung um die Umlaufbahnen mehrerer Sterne, mit einer weiten Auswahl an Periapsisabständen, die sich alle innerhalb der Umlaufbahn des Sterns S2 befinden, zu simulieren. Die gefundene Korrelation wird dann auf S2 angewandt.

Für die Umlaufbahn von S2 erwarte ich einen relativistischen Parameter $\Upsilon = 0.00065$ aus der Theorie, unter der Verwendung der zuvor bestimmten Masse des schwarzen Lochs und der Umlaufbahnparameter. Ich erhalte einen Wert des relativistischen Parameters von $\Upsilon = 0.00088 \pm 0.00080$, welcher innerhalb des Fehlers mit dem erwarteten theoretischen Wert übereinstimmt. Des Weiteren erhalte ich für die Änderung des Arguments der Perisapsis der Umlaufbahn von S2 einen Median mit einer absoluten Medianabweichung von $\Delta\omega = 14' \pm 7'$, welcher konsistent mit der theoretischen Periapsisänderung von $11'$ ist. Daraufhin schließe ich Störeffekte aus, die ähnliche Resultate erzeugen können, wie Abweichungen in den Positionen der Sterne und in der Rotation des Bildfeldes oder der Verschiebung des schwarzen Lochs. Meine Untersuchung zeigt zum ersten mal, dass die feinen Effekte, die von der Allgemeinen Relativitätstheorie für Sterne, die sich auf engen Umlaufbahnen um das schwarze Loch befinden, aus unseren Beobachtungen bestimmt werden können. S2 ist der erste Stern auf einer Umlaufbahn um das supermassive schwarze Loch, für den ein post-Newtonscher Effekt gemessen wurde.

Contents

Abstract i

Zusammenfassung iii

Contents v

1 Introduction 1
- 1.1 The Galactic Center . . . 1
  - 1.1.1 The Supermassive Black Hole in the Galactic Center . . . 1
  - 1.1.2 The Dynamical Components of the Galactic Center . . . 3
  - 1.1.3 The S-cluster . . . 6
- 1.2 Keplerian Orbits . . . 10
- 1.3 General Relativity and Black Holes . . . 12
  - 1.3.1 Post-Newtonian Approximation . . . 13
  - 1.3.2 Relativistic Interactions with a Supermassive Black Hole . . . 14
- 1.4 Observation and Data Reduction . . . 16
  - 1.4.1 Observations . . . 16
  - 1.4.2 Adaptive Optics . . . 17
  - 1.4.3 Data Reduction . . . 18
  - 1.4.4 Deconvolution . . . 19
- 1.5 Dissertation Outline . . . 20

2 Stellar Positions and Orbits in the Galactic Center 23
- 2.1 Introduction . . . 23
- 2.2 Observations . . . 24
- 2.3 Near-Infrared Data . . . 24
  - 2.3.1 Astrometric Accuracy . . . 27
  - 2.3.2 Connection between the NIR and Radio Reference Frames . . . 27
  - 2.3.3 Derivation of the Positions . . . 30
- 2.4 Newtonian and Relativistic Models . . . 37
- 2.5 Stellar Orbits . . . 41
- 2.6 Discussion . . . 43
  - 2.6.1 Comparison to the Litrature . . . 43
  - 2.6.2 Overcoming the Bias in the Orbital Fitting . . . 44

3 Relativistic Orbit of the Stars Near the Black Hole in the Galactic Center 47
- 3.1 Introduction . . . 47
- 3.2 Near-Infrared Data . . . 48

3.3 The Case of Simulated Stars . . . 48
3.4 Method for the Measurements of the PN Effects . . . 53
3.4.1 Squeezed States . . . 53
3.4.2 Periapse Shift . . . 57
3.4.3 Comparison of Methods . . . 58
3.5 The case of S2 . . . 59
3.6 Results . . . 61
3.6.1 The Simulated Stars . . . 61
3.6.2 The S2 Star . . . 63
3.7 Discussion . . . 64
3.7.1 Comparison with the Literature . . . 64
3.7.2 Justifying the Result . . . 69
3.7.3 Detectability of the PN effects . . . 70

4 Summary and Conclusion **71**

5 Appendix **73**
5.1 Justification of Control Method . . . 73
5.2 Minimun χ^2 Estimation . . . 74
5.3 Bootstrap . . . 75
5.4 Runge-Kutta Method . . . 75
5.5 Markov Chain Monte Carlo . . . 76

Bibliography **87**

List of Figures **93**

List of Tables **94**

List of Acronyms **95**

Acknowledgements **97**

Declaration **99**

Curriculum Vitae **101**

1 Introduction

1.1 The Galactic Center

1.1.1 The Supermassive Black Hole in the Galactic Center

The non-thermal radio point source Sagittarius A* (Sgr A*) was discovered in the beginning of the 1970's (Balick & Brown 1974) in the heart of the Milky Way. The possibility of the existence of a Supermassive black hole (SMBH) coinciding at the location of Sgr A* was considered shortly after its discovery. The strongest empirical proof of the existence of a SMBH in the center of our galaxy, are the stellar motions around Sgr A* (Eckart & Genzel 1997; Schödel et al. 2002; Ghez et al. 2003) and its faint accretion emissions. Supermassive black holes with masses between 10^6–10^{10} $M_\odot$ (Kormendy & Ho 2013) exist at the centers of most galaxies (see Graham 2016). Their number density and mass scale are consistent with the assumption that they used to be quasars, which were for a short time in the past highly luminous Active Galactic Nuclei (AGN) fuelled by the accretion of gas and stars. Some of the present-day galaxies host AGNs, but most of the present-day galactic nuclei are inactive, which means that the accretion of gas and stars has either almost stopped or it is non-luminous mode.

The SMBH associated with Sgr A*, has a mass of (M_{BH}) ~4 ×10^6 $M_\odot$ (Schödel et al. 2002; Eckart & Genzel 1996, 1997; Ghez et al. 2000; Eckart et al. 2002; Eisenhauer et al. 2003; Ghez et al. 2005, 2008; Gillessen et al. 2009b; Boehle et al. 2016; Gillessen et al. 2017) and is located at the distance of (R_0) ~8 kpc (Reid et al. 2007; Boehle et al. 2016; Gillessen et al. 2017) from us which makes it by far the closest case of a SMBH; ~100 times closer than the SMBH in Andromeda. Therefore, our Galactic center (GC) is a unique laboratory to study physical processes such as star formation, stellar dynamics, physics of the interstellar medium, accretion emissions, and the least tested theory of physics, general relativity (GR). Despite the name "black" hole, there is information reaching us from vicinity of the event horizon due to the accretion flow of gas and plasma around the black hole, which heats up the material and causes emission across the entire electromagnetic spectrum. Since the very strong dust extinction along the line of sight through the Galactic disk obscures the visible and ultraviolet (UV) regime, Sgr A* is the most accessible to high resolution observations at longer or shorter wavelengths (see Fig. 1.1), i.e. gamma, X-ray, infrared (IR), radio, and sub-millimeter. For example, the visual extinction is 30 mag, while the near-infrared (NIR) K-band (2.2 μm) extinction is only 3 mag.

The low-level accretion activity in the GC (between 10^{-9} to 10^{-7} $M_\odot$ yr^{-1} on the scale of hundreds to thousands of Schwarzschild radii (r_s), using radio polarization

measurements, Goddi et al. 2017) can be observed in the radio and mm wavelengths or in the X-ray. The spectra of the stars are approximately black body and cover only a restricted wavelength range; most of the emission of the stars is in the UV and some are in the IR. Therefore, stars must be observed in the IR, mostly in the K-band. Rapid advances of the IR astronomy in the last two decades has made it achievable to track the orbits of the stars in the crowded region around the SMBH and determine their masses, ages, and their evolutionary stages from their spectral type. Moreover, the line of sight velocities of the stars are measurable from their Doppler shift spectra.

Sgr A* is always visible and bright in radio. Therefore, high resolution studies using radio interferometry is possible. Making use of the Very Long Baseline Interferometry (VLBI) enables us to study the source structure. However, the source size in the radio regime can be broadened due to the interstellar scattering. After subtracting the interstellar scattering, the intrinsic size of Sgr A* at 3.5 mm is 13 r_s (Bower et al. 2006). At wavelengths of about 1 mm, the emission of Sgr A* becomes optically thin and the interstellar scattering is not dominant anymore. Furthermore, Falcke et al. (1998) noticed that a sub-mm excess in the spectrum of Sgr A* implies a scale of the order of a few Schwarzschild radii and that might offer the opportunity to image the event horizon against the background of this synchrotron emission using VLBI at mm/sub-mm waves.
Sgr A* is the main target for the ongoing and future tests of GR for several reasons:

1. Its environment is highly relativistic and its gravitational potential is larger than the gravitational potentials tested by any of the current tests.

2. Its mass and the distance to it have been measured accurately by the NIR observations.

3. Its shadow (which is essentially an image of the photon sphere lensed by the strong gravitational field around the black interior of the black hole within the event horizon) has the largest opening angle among any other black holes in the sky, which makes it resolvable with the mm and sub-mm VLBI observations.

There are three types of experiment for testing GR with the observations of Sgr A*:

1. The NIR monitoring of stars for the detection of the orbital precession with the current instruments and with the forthcoming instruments like GRAVITY for the Very Large Telescope (VLT) or the future 30-meter-class telescopes like the European Extremely Large Telescope (E-ELT) with improved resolution.

2. The high precision timing observations of the radio pulsars in the stellar cluster at the GC with the existing 100-meter-class radio telescope or the future facilities like the Square Kilometre Array (SKA).

3. The space-/time-resolved studies of the accretion flow of Sgr A* and taking the image of a black hole using the Event Horizon Telescope (EHT), a global very long baseline interferometer consists of mm and sub-mm telescopes.

Studying the SMBH in the GC and its stellar environment is of great importance since it can be a representative of similar systems in the Universe. It will give

insights to other SMBHs and the role of stars in their vicinity in feeding and the evolution of them in the galactic nucleus.

***Figure 1.1**: Mosaic of the GC taken by the Spitzer's Infrared Array Camera (IRAC) showing a few 10^5 stars. In the optical, the extinction by dust hides the GC. This is a false-color image. Blue: 3.6 μm, green: 4.5 μm, orange: 5.8 μm, and red: 8.0 μm. Therefore the cool and old stars are in blue and the hot dust is shown in red. Both bright and dark filamentary clouds can be seen. The brightest white spot in the middle of the image is the very center where the SMBH is located. The scale of the image is ~273 pc × 196 pc. Image credit: NASA, JPL-Caltech, Susan Stolovy (SSC/Caltech) et al.*

1.1.2 The Dynamical Components of the Galactic Center

The SMBH dominates the gravitational potential inside its radius of influence r_h of about 3 pc. The radius of influence is the radius where the gravitational potential of the SMBH without the stars is equal to the gravitational potential of the nucleus without the SMBH, i.e. $-GM_{BH}/r_h = \phi_\star(r_h)$. If we consider a singular isothermal distribution for the nucleus with a stellar mass density of $\rho_\star = \sigma_\star^2/2\pi G r^2$ and with a constant velocity dispersion of $\sigma_\star$, then the radius of influence is $r_h = GM_{BH}/\sigma_\star^2$. Studying the stars well outside the radius of influence of the SMBH (100 pc scale) can define the boundary conditions for the inner GC; this means that they can play the role of the control sample for distinguishing the effects of the SMBH from the stellar phenomena.

The GC is the center of the Galactic bulge with a typical length scale of ~2 kpc. It is made of an old (~10 Gyr) stellar population. Further out of the radius of influence of the SMBH, the star-forming region of the Milky Way (100–200 pc) is located (Figer et al. 2004). The star formation is most likely fed by the sizeable reservoir of molecular gas, the central molecular zone in the inner ~200 pc (Serabyn & Morris

1996). Thus the population of the GC is a mixture of the old bulge, intermediate-age, and young stars from recent star formation epochs (Philipp et al. 1999; Mezger et al. 1999; Figer et al. 2004). Half of these young stars are in three young ($\lesssim$ 5 Myr) clusters: The Quintuplet with projected distance of ~30 pc away from the center, the Arches also with projected distance of ~30 pc away, and the central cluster around the SMBH (Figer 2003).

The radius of influence of the SMBH in the GC is as far as 3–5 pc (see Fig. 1.2, Alexander 2005, 2011). There is very little gas within this radius. Beyond the influence of Sgr A*, 10–100 pc, there are a few 10^8 stars, giant molecular clouds (GMCs) and young binaries (Perets et al. 2007). At the border of the radius of influence (~1.5–4 pc) there is a ring of dense molecular cloud streamers called circum-nuclear disk (CND). The CND (with a mass of a few 10^6 $M_\odot$, Becklin et al. 1982; Güsten et al. 1987; Herrnstein & Ho 2002) and a three-armed structure called Sgr A West (also known as the "mini-spiral") are bordered by a young supernova remnant, Sgr A East (see Fig. 1.3) and surrounded by a number of giant molecular clouds on a scale of 5–100 pc (Güsten & Downes 1980; Mezger et al. 1996). The inner 0.5 pc is made of low-mass red and massive blue giants (the products of recent star formation Bartko et al. 2010), and low-mass main sequence stars (B-dwarfs). The existence of fainter main sequence stars and compact remnants, i.e. white dwarfs (WD), neutron stars (NS), and stellar black whole, is presumed. The red giants and the B-dwarfs have an isotropic distribution while blue giants (a few 100 massive OB stars) are in one or maybe two warped and rotating disks (Levin & Beloborodov 2003; Genzel et al. 2003). There is a sharp cut off of their distribution at 0.04 pc. In the inner 0.04 pc (1 arcsec) the distinct S-cluster exists, which is consisting of mostly B-dwarfs (main sequence B-stars) on isotropic orbits (see 1.4). The distribution of the low-mass faint main sequence stars, dark stellar remnants, and particularly a few tens of sollar mass stellar black holes (the "dark cusp") below the current detection limit is unclear.

The SMBH at the GC is at the lower limit of the SMBH masses detected so far (Kormendy & Ho 2013). The supermassive black holes with masses $M_{BH} \lesssim 10^7$ $M_\odot$ are expected to be enveloped by a dense dynamically relaxed cusp of old stars in keeping with the observed M_{BH}–σ relation for the mass of the black hole and the velocity dispersion of the spheroid of the host galaxy (Ferrarese & Merritt 2000; Gebhardt et al. 2000). The only directly detectable tracers of the faint old population are the red giants (K magnitude $\lesssim$ 16). The observed distribution of the red giants in a core inside ~0.5 pc at the GC is flat or even dip instead of rising towards the center (Do et al. 2009; Buchholz et al. 2009; Bartko et al. 2010). The cusp is mainly composed of massive young stars. The reason of it is puzzling and unclear. One explanation could be that some selective mechanism destroys (Amaro-Seoane & Chen 2014) or rejuvenates the old stars so that they apear as hot stars (Hansen & Milosavljević 2003). So far none of these proposed mechanisms are plausible and a in situ star formation is favorable (Alexander 2005). An alternative explanation is that there is no cusp and the GC is not relaxed. A major perturbation that ejected the stars from the GC would increase the relaxation time beyond the Hubble time. Therefore the GC is still returning to its equilibrium through the 2-body relaxation (Merritt et al. 2010). A galactic merger could be such a perturbation (Milosavljević et al. 2002). However there is no other indication of such a major merger.

Scenarios have been suggested to describe the existence of young stars through

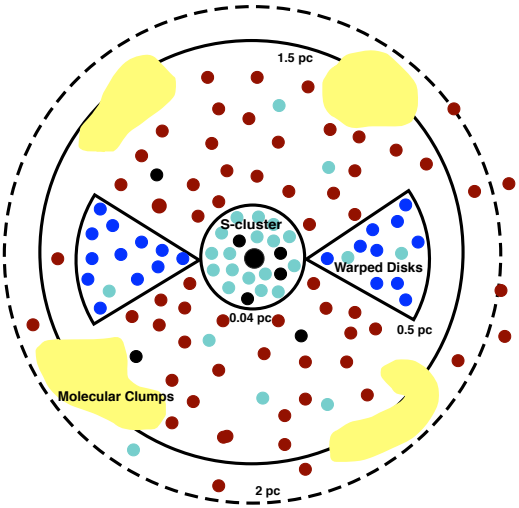

***Figure 1.2**: Not-to-scale schematic of the GC showing the dynamical components close to Sgr A*. The stars are shown with small circles. The colours show their spectral types; dark red: red giants, dark blue: blue giants, and light blue: B-dwarfs. Blobs show the gas clouds. The large black circle in the center is the SMBH.*

star formation (Morris 1993; Morris et al. 1999; Genzel et al. 2003; Levin & Beloborodov 2003; Milosavljević & Loeb 2004; Nayakshin & Cuadra 2005), although strong tidal interactions with the SMBH should suppress star formation in the central region. As an example, Jalali et al. (2014), using hydrodynamic simulations, shows that the strong orbital compression of the molecular clumps existing in the CND in their highly eccentric orbits about the SMBH, increases the gas densities to values higher than the tidal density of the SMBH. Therefore, star formation can occur near the SMBH. IRS 13N, located 0.1 pc away from the SMBH at the GC, which consists of young stellar objects (YSOs) with ages of less than a million year, can be an example (Eckart et al. 2004, 2013; Mužić et al. 2008). Another possibility to explain the existence of young stars in the central ~0.5 pc is an inspiraling cluster scenario (Gerhard 2001). However, this scenario is unlikely, since the tidal field of the SMBH can disintegrate even a dense stellar cluster before reaching the center unless it is held together by an intermediate black hole (IMBH; with a M_{BH} between 100–10^6 $M_\odot$) (Hansen & Milosavljević 2003). So far there is no evidence of the existence of an IMBH in the GC. Moreover, there is a steep cut off in the distribution of the young stars at ~0.5 pc and there is no tidal tail of stripped stars (Paumard et al. 2006), which is expected in this scenario. In general, the in situ fragmenting gas disk scenario is more in favor of the observations and modeling.

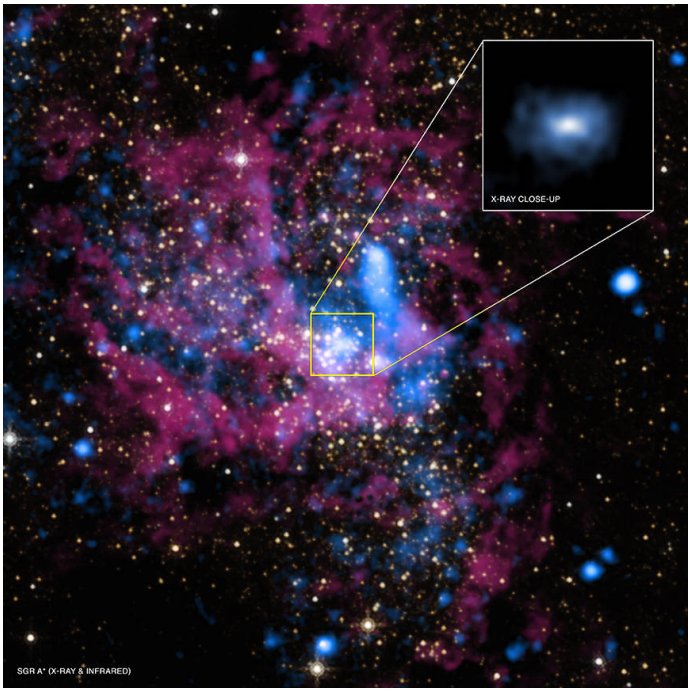

***Figure 1.3**: Multi-wavelength image of the GC containing the X-ray emission from the Chandra telescope in blue and the infrared emission from the Hubble Space Telescope (HST) in red and yellow. The inset is Sgr A* in the X-ray, covering a region of ~0.15 pc wide. The diffuse X-ray emission is from the hot gas captured by the black hole and being pulled inwards. Image credit: X-ray: NASA/UMass/D.Wang et al., IR: NASA/STScI*

1.1.3 The S-cluster

In the inner ~0.04 pc of the GC, there is not any bright giants and only a population of faint blue stars are observed, which are known as the "S-stars" or "S-cluster" after their identifying labels.

Studying the S-cluster, by means of fitting Keplerian orbits to their motion is the most powerful evidence for the compactness of the central dark mass. The optimum band for the observation of these stars is ~2.2 μm, where the extinction is less than 3 mag. Using adoptive optics at the 8m-class telescopes, the intrinsic resolution of the instrument is ~50 mas, which enables the measurements of stellar orbits with semimajor axes of similar sizes corresponding to an orbital period of a few tens of years. The proper motion of the S-stars was presented by Eckart & Genzel (1996) for the first time and soon after the orbits of a handful of stars were determined (Eckart & Genzel 1997; Ghez et al. 1998; Schödel et al. 2002, 2003; Ghez et al. 2005; Eisenhauer et al. 2005a). Before long, the orbits of more than

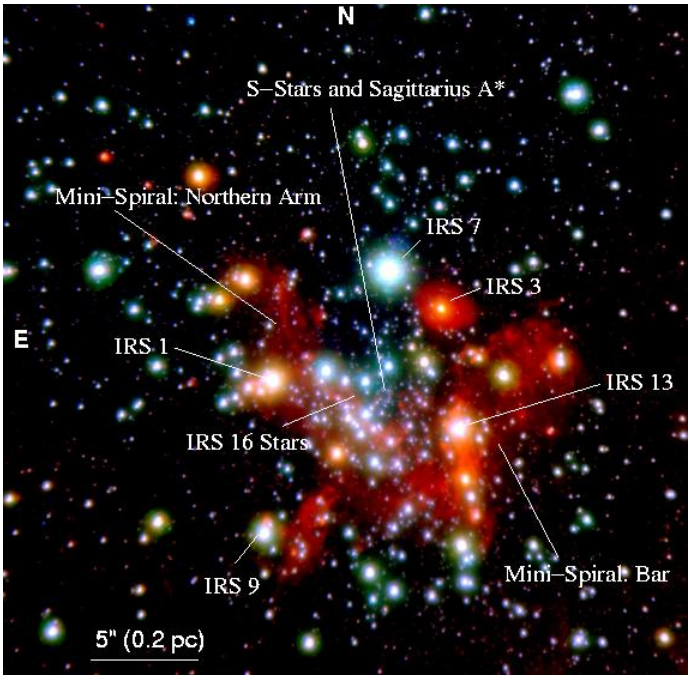

***Figure 1.4**: Central parsec of the GC, using the NIR camera and adoptive optics system of NACO/European southern observatory (ESO) VLT. The images of H, K, and L′ band (at 2.18 μm, 2.36 μm, and 3.8 μm) were combined to obtain a pseudo-color image. Image credit: University of Cologne.*

twenty stars were fully known (Gillessen et al. 2009b; Meyer et al. 2012; Boehle et al. 2016). Up until now, 84 stars ranging from S1 to S175 (plus R34 and R44) are found to be associated with the S-cluster and the number of the determined stellar orbits (including some of the disk members) in the central ~1 arcsec is about forty (Gillessen et al. 2017). Figure 1.5 shows seventeen of these determined orbits. Most of these forty stars (thirty two of them) are on randomly oriented orbits with a thermal eccentricity distribution (members of the S-cluster). Thirty of these are spectroscopically confirmed early-type stars (the remaining two have unknown spectral type, i.e. S39 and S55/S0-102) and the rest are late-type stars (S17, S21, S24, S38, S85, S89, S111, S145). Among the forty stars with determined orbits, eight stars have been identified as members of the stellar disk (S66, S67, S83, S87, S91, S96, S97, and R44, Yelda et al. 2014).

The members of the S-cluster are main sequence B-stars with a few tens of sollar masses, which are sometimes naively associated with the young stars farther out. However, they are considerably different from the young disk stars. The disk stars are on approximately circular co-rotating orbits while the S-stars are on randomly

oriented elliptical (higher eccentricity) orbits. Furthermore, the S-stars are early B-stars while the disk stars are bright massive O-stars. The brightest S-stars are much fainter and long-lived than the young disk stars. Some authors have considered a disk origin for the S-stars (Milosavljević & Loeb 2004; Löckmann et al. 2009; Madigan et al. 2009; Griv 2010) but they do not provide a compelling scenario for the inverse mass segregation, where the lower mass stars are more to the center than the massive stars.

A proposed scenario to explain the origin and nature of the S-stars is that they migrated to the central arcsec from the field (outside of the central parsec), so they are unassociated to the disk stars. But as it is already discussed above, migration scenarios are not conclusive. Another interesting suggested scenario is the dynamical capture of binaries travelling to the center by the SMBH tidal disruption (Hills 1988). Such binaries are scattered in parabolic orbits and the point of the tidal disruption becomes the periapse distance for the captured star. This could additionally unravel the origin of the hypervelocity stars (HVSs) in the Galactic halo (Perets 2011). There is a number of evidence to reinforce this suggestion. One is the luminosity function (LF) of the S-stars, which is similar to the one observed in the field and is different from the flat LF of the disk stars (Genzel et al. 2010). Another evidence is the high eccentricity of the S-stars, which is not expected from an isotropic distribution (Gillessen et al. 2009b). Also, the number of the observed S-stars (~ forty) is consistent with the number of the HVS (see Brown 2015). However, the 2-body relaxation is not fast enough to divert the massive binaries from the field to the center to maintain the number of the S-stars. An explanation can be the existence of massive perturbers (GMCs) in the distance of ~5–100 pc (Perets et al. 2007).

Not long ago, a fast-moving infrared excess source within the cluster has been discovered on a highly eccentric orbit towards the black hole (Gillessen et al. 2012). Strong evidences suggest that this source, called the Dusty S-cluster object (DSO) (Eckart et al. 2013) or G2 (Gillessen et al. 2012) is a member of the cluster. Further monitoring of the DSO to detect the potential effect on the activity of the SMBH has raised many different scenarios and interpretations of the data about the nature of the source. The prime argument is whether the DSO is a dust-enshrouded star, which has kept its compact nature and is continuing its motion along the same orbital trajectory as is suggested by Eckart et al. (2013) (see also Witzel et al. 2014; Valencia-S. et al. 2015; Shahzamanian et al. 2017; Zajaček et al. 2017) or it is, as Gillessen et al. (2012) (see also Gillessen et al. 2013a,b; Pfuhl et al. 2015; Plewa et al. 2017) suggest, a gaseous and dusty coreless cloud of a few Earth masses, which is tidally stretched after going through its periapse passage in 2014. Some even suggest that the origin of the DSO/G2 is likely related to the precursor source G1, since there is some similarities in their orbital evolution, though their orbits are not identical (Plewa et al. 2017). The Keplerian orbital parameter of the DSO is very well constrained (see Valencia-S. et al. 2015) and since the source seems to be compact and still following the same orbit, the dust enshrouded scenario is more plausible. Moreover, in the anticipation of the possible tidal disruption of a gas cloud, many tried to observe the increased activity of Sgr A*, but no additional activity has been observed.

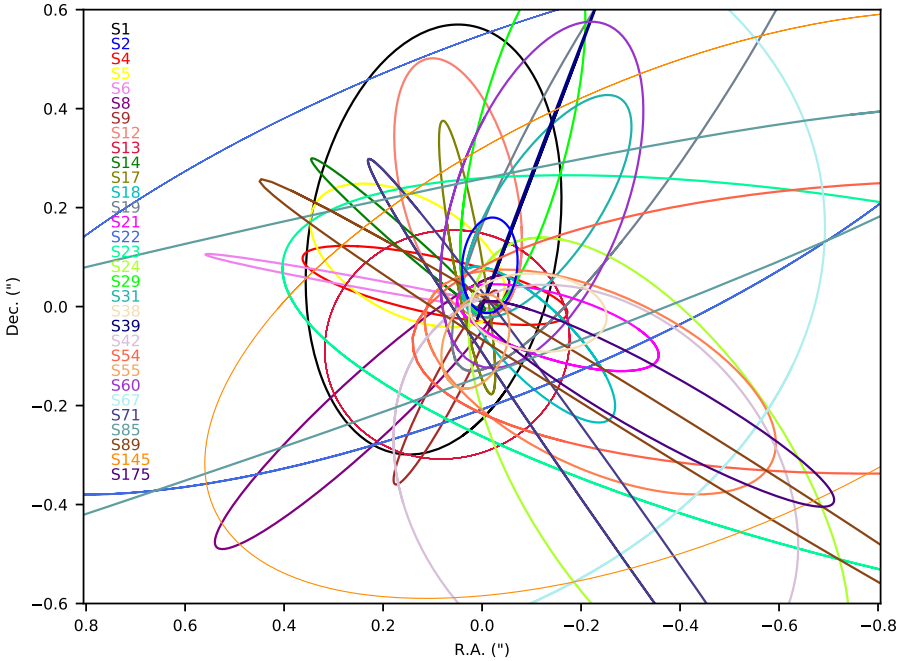

***Figure 1.5**: Best-fit stellar orbits of 31 stars around Sgr A* in the central ~0″.6. The fitting procedure is done by Lauritz Tizian Thomkins for 23 stars and the rest of the orbital parameters are taken from Gillessen et al. (2017, Table 3).*

1.2 Keplerian Orbits

For studying and modeling the stellar phenomena, in most cases the stars can be regarded as point masses dominated by the gravity. The very large difference between the mass of a star and that of a SMBH simplifies the studies as a result of negligible star-star gravitational interactions. To simplify matters, in most processes the Newtonian dynamics are sufficient and the GR effects can be neglected.

The motion of a star relative to a black hole can be expressed in a form of a Keplerian orbit, which is an ellipse, parabola, or hyperbola with a two-dimensional orbital plane in a three-dimensional space. It is a solution to a special case of a two-body problem known as the Kepler problem with three assumptions:

1. The bodies are spherically symmetric and can be treated as point masses.
2. No external or internal forces acting upon the bodies other than their mutual gravitation exists.
3. When compared to the central body, the mass of the orbiting body is insignificant.

This solution can be expressed via six orbital elements known as the "Keplerian elements" (Fig.1.6). A position and velocity vector in three dimensions known as the orbital state vectors characterize the motion of an object. The orbital parameters can be obtained from the state vectors or vice versa. In contrast to the state vectors, five of the total six orbital elements are constant, which makes using the orbital elements more convenient. Two of the orbital elements define the size and shape of the orbit:

- Semimajor axis a
- Eccentricity e

Three angles (Euler angles) define the orientation of the orbital plane in three dimensions:

- Inclination i, defined as an angle between the orbital plane and the reference plane (the plane of the sky here)
- Longitude of the ascending node Ω, defined as the angle between the reference direction (North within the frame of our work) and the ascending node on the reference plane
- Argument of periapse ω, defined as the angle between the ascending node and the periapse in the orbital plane

And Finally:

- True anomaly ν, defined as the position of the orbiting body along the trajectory measured from the periapse

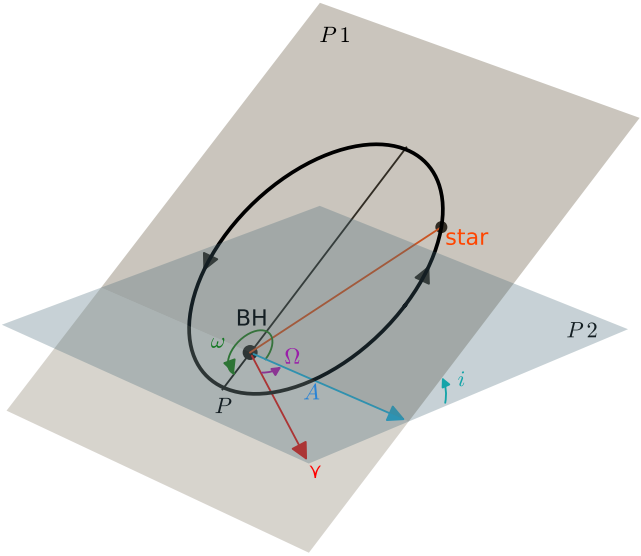

***Figure 1.6**: Keplerian orbital elements for a star revolving a black hole. Here BH is the central black hole, P1 is the orbital plane, P2 is the plane of the sky, ϒ is the reference direction, A is the ascending node, P is the periapse, i is the inclination, ω is the argument of periapse, and Ω is the longitude of the ascending node.*

There are several alternatives to the true anomaly such as the mean anomaly M or the time of the periapse passage T_p.

In order to find the position of a star at each epoch, "Kepler's equation" has to be written and solve. The "Kepler's equation" is defined as:

$$M = E - esinE, \tag{1.1}$$

where E is the eccentric anomaly. Eccentric anomaly is the angle that defines the position of a body on a Keplerian orbit, while mean anomaly M is an angle in an imaginary circular orbit corresponding to the eccentric anomaly. M and e are known parameters, and the equation has to be solved for E. However, since sine is a transcendental function, there is no algebraically solution to the equation. This means that the approximate value of E has to be found numerically by finding the root of the following equation iteratively

$$f(E) = E - esinE - M. \tag{1.2}$$

One possibility is to use the Newton's method (also known as the Newton–Raphson method). The method starts with $f(E)$, the derivative $f'(E)$, and an initial value E_0 as an approximate solution. In this case, the initial value of $E_0 = M$ is sufficient. However, for $e > 0.8$, $E_0 = \pi$ should be used. A better approximation is determined by

$$E_{n+1} = E_n - \frac{E_n - esinE_n - M}{1 - ecosE_n}. \tag{1.3}$$

The iteration is continued until a desired accuracy is obtained. The idea behind this method is that if the initial guess is close enough to the solution, then its tangent line approximates the function. The intercept of this tangent line is a better approximation to the solution than the initial guess. If the initial guess is close enough to the solution and the derivative at the initial value exist, the method will usually converge. The rate of convergence is quadratic, if the multiplicity of the root is 1, similar to the case here. Otherwise, the convergence rate is linear. There is a method to preserve the quadratic convergence rate in these cases.

1.3 General Relativity and Black Holes

General relativity is the geometric theory of the gravitation by Albert Einstein in 1915 (Einstein 1915). It provides a unified description of the gravity by generalizing special relativity and the Newton's law of gravitation as a geometric property of the space-time. The relation of the curvature of the space-time to the energy and momentum of the matter and radiation is specified by the Einstein field equation, which is a system of ten partial differential equations in the form of a tensor equation. The solution to these equations is the components of the metric tensor for a given stress-energy in the space-time. The trajectory of the particles, with mass or massless (photons) are then calculated using the geometric equations. General relativity predicts that a sufficiently compact mass can affect the space-time to form a black hole. However, the idea of a massive body that even light cannot escape from it was already proposed by John Michell. A few months after the development of GR, Karl Schwarzschild found a solution to the Einstein field equation, which describes a static black hole (Schwarzschild 1916). During the golden age, other solutions to the Einstein field equation for the charged (Reissner 1916; Nordström 1918), spinning (Kerr 1963) or spinning and charged (Newman et al. 1965) black holes were found.

General relativity has been tested by many different experiments, from the Eddington's solar eclipse expedition in 1917 to the modern observations of the binary pulsar systems. However, all these tests are in the weak-field regimes, while general relativity is untested in the strong-field regime. Near-infrared observations of the stars and pulsars are tests of the weak-field regime ($r \ll r_g$) too. In this regime, using a parametrized post-Newtonian (PN) formalism with the Newtonian gravity is sufficient, while for the strong-field regime ($r \sim r_g$) tests such as the observations of the accretion flow, careful modeling of the space-time is needed. The tests of GR with the gravitational wave observations of the extreme mass-ratio inspirals (EMRIs) are also in this regime.

Black holes have no "hair". According to the "no hair" theorem, black holes are

uniquely described by the three parameters of the Kerr-Newman metric, namely the mass, angular momentum, and electric charge. All other information about the matter inside the black hole (or "hair") vanishes behind the event horizon. An event horizon is a virtual boundary that disconnects the interior of a black hole from the its exterior. General relativity has predicted the existence of the event horizon, but there has been no proof of it so far. Other important physical properties of a black hole are the singularity (where the spacetime curvature becomes infinite) and photon sphere (a spherical boundary where any photon with a tangent motion would be trapped in a circular orbit). It can be argued that an astronomical black hole can be described by the Kerr metric since black holes are believed to be the final state of the evolution of massive stars and during their formation any other signature other than the mass and spin of the original star is radiated away. Moreover, astrophysical black holes are thought to be basically electrically neutral as a result of neutralization of any residual electric charge.

1.3.1 Post-Newtonian Approximation

The post-Newtonian (PN) approximations are used to find an approximate solution of the Einstein field equation for the metric tensor. These approximations are expanded in small parameters, for example, the ratio of the velocity of matter to the speed of light (v/c), which express the orders of deviations from the Newtonian gravitation in the weak-field region. Higher order terms are added for more accuracy. If the small parameter used for the expansion is zero, the PN approximations reduce to the Newtonian law of gravity.

The simplest black hole that has a mass but neither a charge nor spin is called a Schwarzschild black hole. There is no observational difference between the gravitational field of this type of black hole and any other spherical object with the same mass. The event horizon of the Schwarzschild black hole is called the Schwarzschild radius (r_s). A mass that is neither charged nor rotating and is smaller than its Schwarzschild radius, forms a black hole. Since the precession of the orbit of a test particle due the frame-dragging near a rotating black hole is very small, to find the orbit, an astrometric black hole can be considered to be a Schwarzschild black hole for simplification. A Schwarzschild black hole is described by the Schwarzschild metric. The line element of the Schwarzschild metric has a form of

$$c^2 ds^2 = \left(1 - \frac{r_s}{r}\right) c^2 dt^2 - \left(1 - \frac{r_s}{r}\right)^{-1} dr^2 - r^2 \left(d\theta^2 + sin^2\theta d\phi^2\right). \tag{1.4}$$

Here r_s is the Schwarzschild radius defined as $2GM/c^2$ (Schwarzschild 1916). A particle orbiting in this metric can have a stable circular orbit with $r > 3r_s$. A circular orbit of minimum radius $1.5r_s$, corresponds to an orbital velocity approaching the speed of light (c). A star that is sufficiently close to a Schwarzschild black hole experiences an acceleration given by equation

$$a_\star = -\frac{M_{BH}\vec{x}}{r^3} + \frac{M_{BH}\vec{x}}{r^3}\left(4\frac{M_{BH}}{r} - v^2\right) + 4\frac{M_{BH}\dot{r}}{r^2}\vec{v}, \tag{1.5}$$

in the first PN order, where $\vec{x}$ and $\vec{v}$ are the position and velocity vector of the star and $G = c = 1$ (Will 1993). The numerical integration of this equation will

result in the elliptical orbit of the revolving star showing precession in the orbital plane. Using a Kerr-Newman black hole instead of a Schwarzschild one, will add a few more terms due to the angular momentum vector (the frame-dragging effect) and quadruple moment of the black hole (see for examples, Zhang et al. 2015; Johannsen 2016; Will & Maitra 2017; Zhang & Iorio 2017; Iorio & Zhang 2017; Hees et al. 2017; Iorio 2017).

The relativistic parameter at periapse is defined as $\Upsilon \equiv r_s/r_p$ with r_s being the Schwarzschild radius and r_p the periapse distance. The relativistic parameter changes along the orbit. A mildly relativistic orbit follows an almost Keplerian energy equation and Υ can be expressed as

$$\Upsilon = \beta^2 + \frac{GM_{BH}}{c^2 a} \equiv \beta^2 + \Upsilon_0. \tag{1.6}$$

Here a is the semimajor axis and $\beta \equiv v/c$ (Alexander 2005). If $e \gg 0$ and the star is close to its periapse, then $\beta^2 \gg \Upsilon_0$ and consequently $\Upsilon \sim \beta^2$. The deviations from the Newtonian mechanics become greater as Υ increases. For $\Upsilon \ll 1$, which is the case for the stars near the SMBH at the GC, it is advantageous to expand the PN deviations in β and attribute each effect by the order of its β-dependence or equivalently, by the orders of r_s/r_p or r_s/a (Alexander 2005).

1.3.2 Relativistic Interactions with a Supermassive Black Hole

When a star approaches a SMBH on an orbit with a periapse distance smaller than the tidal disruption radius of the black hole, the work done by the tidal field transfers the energy and angular momentum from the orbit of the star to the star itself and unbinds it (Alexander 2017). Therefore, the observable relativistic interaction near a SMBH depends on the tidal radius to event horizon ratio. A $\sim$1 $M_\odot$ main sequence star will be disrupted outside the event horizon of a SMBH and the tidal interactions perturb its motion outside the tidal disruption radius. However, stellar black holes and to some extent the NSs and WDs can reach the event horizon without perturbations. Consequently, the main sequence stars can merely be the probes for the weak PN effects, while stellar remnants can be probes for the strong gravity.

The observed redshift curve z(t) can be expanded in terms of β in three-dimensions (Alexander 2005; Zucker et al. 2006),

$$z = \frac{\Delta\lambda}{\lambda} = B_0 + B_1\beta + B_2\beta^2 + O(\beta^3). \tag{1.7}$$

Two effects contribute to the second term, the special relativistic transverse Doppler effect and the GR gravitational redshift. The GR gravitational redshift, which also contributes to the zeroth-order z expansion, is

$$z_G = (1 - r_s/r)^{-1/2} - 1 \simeq r_s/2r = r_s/4a + \beta^2/2, \tag{1.8}$$

and the relativistic Doppler shift of a moving source seen by an observer at rest is

$$z_D = \frac{1 + \beta cos(v)}{\sqrt{1-\beta^2}} - 1 \simeq \beta cos(v) + \beta^2/2, \tag{1.9}$$

where v is the angle between the velocity vector and the line of sight (Alexander 2005; Zucker et al. 2006). The first order term is the Newtonian Doppler shift and the second order term is the special relativistic transverse Doppler effect. The lowest order β^2 effects, which are already above the detection limits of the current instruments through spectroscopy (Zucker et al. 2006) are expected to be observed in the near future.

Another effect that needs to be considered here is the Roemer delay. It is a Newtonian effect and caused by the fact that the travel time for the light coming from a star to the observer changes with the orbital phase, when the orbit has an inclination with respect to the plane of the sky. This difference between the emission and arrival times of the signal causes a deviation from a Newtonian orbit, which is dependent on the orbital parameters. The Roemer effect is also a β^2 correction, which is larger than both the GR gravitational redshift and the Special relativistic transverse Doppler effect. Multiple stars and their proper motions are needed to break this degeneracy.

The third-order (β^3) GR effects, such as the frame dragging[1], gravitational lensing[2] of the background stars by a SMBH and stellar black holes (Alexander & Sternberg 1999a,b; Alexander 2001), and Shapiro delay[3] (Shapiro 1964; Kopeikin & Ozernoy 1999), or GR periapse shift (although it is a β^2 effect in the proper motions) will not be detectable with the available radial velocity data.

There are some debates over whether the relativistic precession in the proper motion of the known short period stars is observable with the current instruments. There is a high expectation for the detection of these effects and the no-hair theorem (Will 2008; Merritt et al. 2010; Iorio 2011; Zhang et al. 2015) on the very short period stars by the IR interferometer GRAVITY (Eisenhauer et al. 2011). However, the Newtonian precession and resonant relaxation perturbations by the background stars can partially or completely affect the detection of the relativistic precessions (Merritt et al. 2010; Sabha et al. 2012). Nevertheless, it is unclear how many of these relativistic stars are in short orbits around the SMBH. High precision measurements of the radio pulsars could give us a better understanding of the properties of the SMBH (Eatough et al. 2015), but so far there is only one pulsar detected near Sgr A*. The observation in the GC increased after the discovery of the DSO/G2. This led to the discovery of a pulsar 0.12 pc away from the black hole after the very bright flare recorded by Swift in April 2013 (Kennea et al. 2013). The NuSTAR X-ray telescope reported that the flaring object is a magnetar with a spin rate of 3.76 seconds (Mori et al. 2013). Observing the gravitational lensing of the background stars by the SMBH and stellar black holes is also anticipated (Alexander & Sternberg 1999a,b; Alexander 2001). Gravitational lensing of the stars by the SMBH is slightly different from the other effects discussed here, since it is an effect on the light emitted by a star, rather than an effect on the star itself, and since the affected stars are usually far away from the dynamical radius of influence of the

[1]The changes in the trajectory of a star orbiting a spinning black hole by changes in the longitude of the ascending node corresponding to the precession of the orbital angular momentum vector around the black hole's spin vector, also known as the Lense-Thirring precession.

[2]The bending of the light from the source by a distribution of matter (called the gravitational lens) such as a cluster of galaxies or a black hole, as it travels towards the observer.

[3]Radar signals passing near a massive object take slightly longer to travel to a target and longer to return. The time delay is caused by the spacetime dilation, which increases the path length. The Shapiro time delay is one of the four classic solar system tests of GR.

SMBH. Another class of the GR effects that may also be detectable in the GC is the emission of the gravitational wave (GW) from the very low-mass stars that spiral into the SMBH.

The strong interactions of stars with a SMBH, defined as interactions, indescribable by the Newtonian gravity, such as the annihilation or absorption of the whole star by the SMBH or the tidal disruption are beyond the scope of this thesis.

1.4 Observation and Data Reduction

1.4.1 Observations

***Figure 1.7**: VLT in the Paranal observatory, Chile. Image credit: John Colosimo/ESO.*

In astronomy, the infrared range is divided into three subcategories of near-infrared (NIR): ~0.7–5 μm, mid-infrared (MIR): ~5–30 μm, and far-infrared (FIR): ~30–1000 μm. For observations in the mid to far-infrared regimes using rockets, balloons, aircrafts, and space telescopes are necessary, since some bands get absorbed fully by the atmosphere. In order to be able to observe in the NIR, ground-based telescopes have to be in dry locations in high altitudes, since there will be less water vapor absorption in the atmosphere. The very large telescope (VLT) is located in such a condition in Cerro Paranal, 2635 metres above the sea level in the driest desert on Earth, Atacama in Chile. The VLT consists of four unit telescopes (UT) with 8.2 m primary mirrors, which can work together as an interferometer called the VLTI. For the purpose of this work, one unit telescope has been used. There are also four movable auxiliary 1.8 m telescopes as can be seen in Fig. 1.7. The location of the VLT is ideal to study the GC since it is mostly visible from the southern hemisphere. Since the GC is a very crowded region and Sgr A* is a very faint source in the NIR, a high angular resolution is needed in order to distinguish the sources and locate the black hole.

In this work, K_s-band (central wavelength 2.18 μm with width of 0.35 μm) images of the central cluster are acquired with the NACO instrument, which is reinstalled from 2014 in the UT1 of the VLT. It was installed before in the UT4 from 2001 to 2013. The NACO instrument is a combination of the Nasmyth adaptive optic (AO) system (NAOS) and the Coude near-infrared camera (CONICA). NAOS is designed to work with natural guide sources. CONICA is a NIR imager and

spectrograph capable of AO assisted imaging, no AO imaging, imaging polarimetry, and cornography. The characteristics of the cameras of CONICA are described in Table 1.1 in terms of the plate scale and field-of-view (FoV).

***Table 1.1**: CONICA list of cameras. Credit: ESO NACO user manual.*

Camera	Scale (mas/pix)	FoV (arcsec)	Spectral Range (μm)
S13	13.221 ± 0.017	14 × 14	1.0 – 2.5
S27	27.053 ± 0.019	28 × 28	1.0 – 2.5
S54	54.50 ± 0.10	56 × 56	1.0 – 2.5
L27	27.19	28 × 28	2.5 – 5.0
L54	54.9	56 × 56	2.5 – 5.0

1.4.2 Adaptive Optics

Reaching the diffraction-limited resolution in a telescope is not possible due to the atmospheric turbulence and instrumental effects of the telescope itself. Ideally, the angular resolution of the telescope is given by $\theta = 1.22\lambda/D$. The parameter D is the diameter of the primary mirror of the telescope and λ is the observing wavelength. For the VLT, the diffraction-limited resolution at $\lambda = 2.2$ μm is $0''.057$. The atmospheric turbulences limit this resolution to $\lambda/r_0 \sim 0''.7$. The effecting parameter here (r_0) is the Fried parameter, which is related to the strength of the turbulence and is dependent on the wavelength by $\lambda^{6/5}$. The correlation time of the turbulence t_0 is another effecting parameter, which is related to r_0 and the speed of the turbulent air, and corresponds to the time-scale over which the changes in the turbulence become significant. In order to have stable atmospheric conditions and a better performance of the AO system, these two parameters, i.e. r_0 and t_0, have to be sufficiently large. The "seeing" can be described by these two parameters as $\epsilon = 0.98\lambda/r_0$ (Fried 1966). Moreover, heat, wind force, and gravity cause deviation in the telescope structure, which leads to image degradation.

Adaptive optics system can correct for all these small changing errors and compensate in the real-time for the deformation of the wavefront (WF) caused by the atmospheric turbulence on a bright guide star. The incoming light is split by a dichroic mirror and travels to a wavefront sensor (WFS). The WFS and a Real-Time Computer (RTC) that processes these measurements and controls a deformable mirror (DM) to correct for them and restore the WF flatness then measure the distortions in the WF. The DM is a thin plate mirror placed on a set of piezoelectric actuators that can push and pull it from the back. The DM of NAOS contains 185 actuators. The quality of the image is determined directly by the WF error. The seeing parameter r_0 determines the spacing of the actuators needed in an AO system and t_0 determines the correction speed required to compensate for the effects of the atmosphere. An AO system works in a closed loop. The DM flattens the WF and the WFS measures the residual WF error. A schematic view of the AO system is shown in Fig. 1.8.

An important parameter that defines the image quality is the Strehl ratio (SR). It corresponds to the ratio between the intensity peaks of the corrected image and the

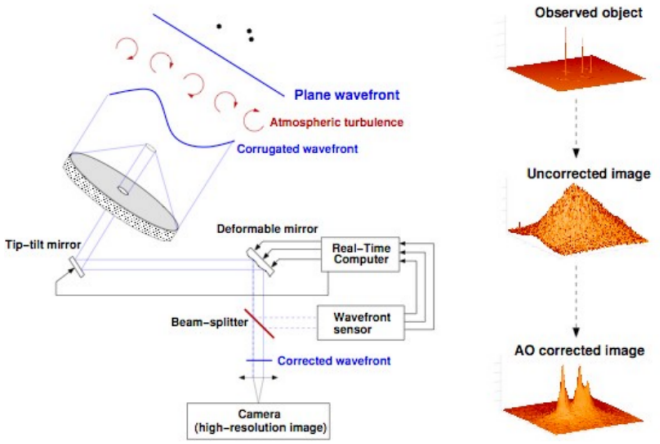

***Figure 1.8**: Principle of the Adaptive Optics. Credit: ESO NACO user manual.*

theoretical point spread functions (PSFs); i.e. a higher ratio corresponds to a better image quality. For the GC observations, the bright supergiant IRS 7 (with a K_s-band magnitude of ~7), which is located ~5″.6 north of Sgr A* is a good candidate for guiding star. Since finding the proper guiding source is not always trivial, there is an alternative method called the laser guide star (LGS) technique. In this technique, an artificial guiding point source is created by a Sodium-laser that excites the Sodium atoms in the mesosphere at 90 km altitude. If the observing conditions are suitable and the guide star is a close and bright source, the resulted PSF will be very close to the diffraction limit. In this situation, the Strehl ratio in the K_s-band will be more than 30%. In the case of not suitable observing conditions or at shorter wavelengths, the Strehl ratio is only a few percent. The current AO systems correct images at $\lambda > 1$ μm since for shorter wavelengths higher computational power is needed.

1.4.3 Data Reduction

Several adverse effects caused by the detector itself or by the thermal emission of the telescope or the sky emission at that special wavelength can influence the image. Therefore, it has to be corrected. The detector has inhomogeneity from its production procedure or from ageing. As a result, a given flux of the photons can be recorded by different counts at a different region of the detector. In order to correct for this issue, it is necessary to get the detector's response function on the night of the observation. To do so, a map of the pixel response is produced by the images of the twilight sky (the sky flat-field) or a lamp (the lamp flat-field), when the lamp is switched on and off. The on/off images of the lamp are then subtracted and averaged. The object frame is then divided by the flat-fields, which is called flat-fielding. Another method that also can minimize the detector's cosmetics is

jittering. The idea is to not let the sources lie on the same position of the detector. Taking several images of the field with offsets of small values does this.

The sky frame has to be subtracted from the object frames in order to remove the OH emission of the atmosphere for $\lambda \leq 2.2\ \mu$m. This is called the sky-subtraction. The sky frame has to be taken in a nearby field to the source, where there are not any apparent sources. For the GC, the closest location is 713″ west and 400″ north of IRS 7. The sky frames have to be taken several times since the thermal emission changes. For $\lambda \leq 2.2\ \mu$m the sky observations are done every ~2 hours while for the longer wavelengths where the atmospheric and telescope emissions are stronger, the smapling has to be done more frequently.

Replacing the dead/bad pixels with interpolations, i.e., average values, of the neighbouring pixels, does the dead/bad pixel correction. These pixels have either a zero or a high response value compared to the neighbouring pixels. Finally, the reduced images are shifted and stacked in a cube to get a mosaic image of the object or the field, in order to have higher signal to noise ratio.

1.4.4 Deconvolution

In an ideal case, the PSF, which is the image of a point source, would be an Airy pattern as a result of the diffraction of the light on the telescope aperture. In a real case the PSF varies with time due to the atmospheric turbulence and some effects of the telescope. Moreover, the PSF varies over the FoV. A deconvolution is a process used to reverse the effects of the convolution on the observed image. The observed image $I(x, y)$ is the convolution of the real object $O(x, y)$ with a $PSF(x, y)$. In reality there is also an additional noise $c(x, y)$,

$$I(x, y) = PSF(x, y) \odot O(x, y) + c(x, y). \tag{1.10}$$

Here we wish to recover $O(x, y)$, the real object. The symbol $\odot$ is the convolution operator. If we neglect the noise term, the Fourier transformation of the real object can be derived by a division in Fourier space like

$$\hat{O}(u, v) = \frac{\hat{I}(u, v)}{\hat{PSF}(u, v)}, \tag{1.11}$$

where $\hat{O}(u, v)$, $\hat{I}(u, v)$, and $\hat{PSF}(u, v)$ are the Fourier transformation of the original functions with u and v being the spatial frequencies corresponding to the x and y coordinates.

Due to the limitations like neglecting the noise and inaccurate determination of the PSF, different methods have been developed to recover the object distribution. Eckart et al. (2005) studies and compares different deconvolution methods. In this work, Lucy-Richardson deconvoluted images of the GC using the S13 camera of the NACO instrument has been used. Therefore I describe it bellow shortly. Before using a deconvolution method, it is vital to estimate the PSF. The PSF in the GC can be extracted individually for each source in the image using the software package StarFinder (Diolaiti et al. 2000). The StarFinder is an algorithm for a crowded stellar field for a semi-automatic PSF extraction and does high precision astrometry and photometry. It estimates the initial PSF by finding the median of several isolated

and bright sources selected by the user and then continues by finding sources and repeating the PSF extraction.

1.4.4.1 Lucy-Richardson Deconvolution

The Lucy-Richardson deconvolution (Lucy 1974; Richardson 1972) is an iterative algorithm for recovering an image that has been blurred by a known PSF and allows for the separation of flux density contributions of very close sources. First, the current estimate of the object distribution $O_n(x, y)$ is convolved with the $PSF(x, y)$ as

$$I_n(x, y) = O_n(x, y) \odot PSF(x, y). \tag{1.12}$$

Then the resulting image $I_n(x, y)$ is compared with the observed image $I(x, y)$,

$$Q(x, y) = \frac{I(x, y)}{I_n(x, y)} \odot PSF(x, y). \tag{1.13}$$

The PSF behaves as a low-pass filter that decreases the contribution of high spatial frequencies on the result as these frequencies are strongly under the influence of the noise. Finally, a new estimation of the object distribution $O_{n+1}(x, y)$ is found by the multiplication of the old object distribution $O_n(x, y)$ by $Q(x, y)$ as

$$O_{n+1}(x, y) = O_n(x, y) \odot Q(x, y). \tag{1.14}$$

The high spatial frequencies are subdued due to the convolution with the PSF and consequently the noise amplification is prevented. A sufficient number of iterations are needed to resolve the details of the image related to the high spatial frequencies. This results in a large computation time and therefore is a drawback of this algorithm. However, the image will not always benefit from a large number of iterations, since there is a chance that the diffuse background resolves into the point sources. The addition of the diffuse background and the flux densities of very faint sources into the flux density of a bright source is also another difficulty. Figure 1.9 shows the effect of the Lucy-Richardson deconvolution on an image of the central region of the GC.

1.5 Dissertation Outline

In this thesis, I study the physics in the vicinity of a SMBH through the observations of the S-cluster. I use the NIR imaging and spectroscopy data of the three S-stars closest to Sgr A* to determine the following:

- The mass of and the distance to Sgr A*. I start with the details of the observations in the NIR, the data reduction, and the Newtonian and relativistic PN models in Chapter 2. I discuss the astrometric accuracy that I can achieve with the data and find the astrometric positions of the three candidate stars, i.e., S2, S38, and S0-102/S55. I find the best orbital fits and consequently, I obtain the gravitational potential parameters.

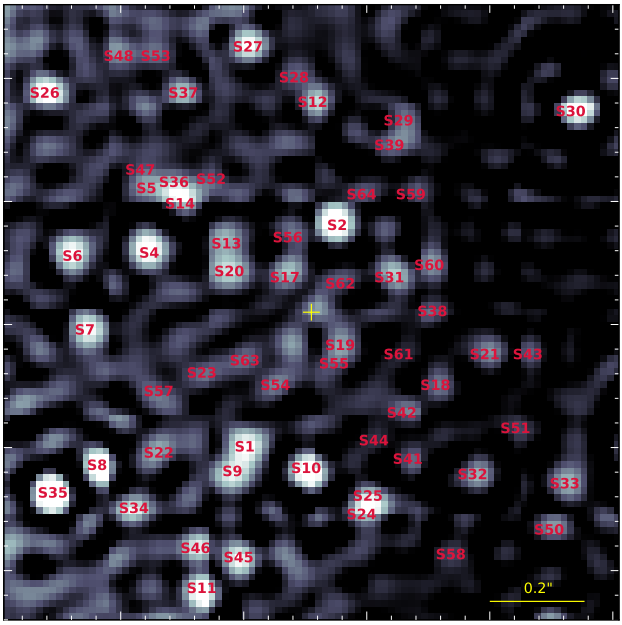

***Figure 1.9**: K_s-band image of the central arcsec of the GC taken in May 2011 with the S13 camera of the NACO instrument at the VLT after the Lucy-Richardson deconvolution. The S-stars are marked by their names. The position of Sgr A* is marked by a yellow plus.*

- The PN effects observable in the proper motion of S2. I develop methods that use the deviations from a Newtonian symmetric orbit to measure the PN effects within the weak-field limit in Chapter 3. S2 is the only S-star with a small enough periapse distance that makes the observation of these effects promising. It is also the only star with enough available astrometric and radial velocity data. I start with simulating the orbits of stars that are located within the orbit of S2 as case studies. The results from these simulations are analyzed by connecting them to the relativistic parameter at the periapse. This is beneficial in assessing the magnitude of the PN effects. Finally, I apply the results on S2 in order to confirm the PN characteristics of the orbit.

I give a summary of the results in Chapter 4. Finally, I provide supplementary information in the Appendix.

2 Stellar Positions and Orbits in the Galactic Center

2.1 Introduction

The existence of a $\sim 4 \times 10^6 M_\odot$ supermassive black hole (SMBH), Sagittarius A* (Sgr A*) has been proved by observing the S-stars. The S-stars (also referred to as the S-cluster) are the Galactic center (GC) small group of fast moving stars located in the very center of our galaxy, the Milky Way. The high velocities of some of the S-stars and their small periapse distances triggered the tests of general relativity (GR) and its predictions. But the tests of GR rely on accurate measurements of the gravitational potential of the SMBH, more precisely the mass of the SMBH (M_{BH}) and the distance to the GC (R_0). Moreover, the exact determination of the stellar orbits is as vital, since we expect to detect small deviations in the orbital trajectories.

The exact estimation of the mass of Sgr A* is essential since this quantity enables us to position our galaxy in the observed correlation between the black hole mass, the velocity dispersion and the stellar luminosity of the bulge (Ferrarese 2002; Tremaine et al. 2002; Kormendy & Ho 2013). The accurate determination of the distance to the GC enables us to calculate the apparent size of the Schwarzschild radius of the black hole in the sky. The size of the shadow of the black hole depends on M_{BH} and R_0 (e.g. Falcke et al. 2000; Fraga-Encinas et al. 2016) and it can be observed if the black hole has a spin, a suitable orientation, and in case the accretion zone is not disturbed to a great extend.

Among the members of the S-cluster, three of the detected stars are most suitable for both the gravitational potential measurements and the detection of the GR effects; due to their close proximity to the center, i.e. their small orbital periods. A smaller orbital period is favourable since the star can be observed for a full orbit in a shorter time. A small periapse passage and consequently a higher velocity at the periapse make the GR effects more noticeable. Gillessen et al. (2017) has recently raised the number of the stars with determined orbits to forty. In total 84 stars are associated with the S-cluster, but many fainter stars are assumed to exist in the innermost region of the GC (Sabha et al. 2012).

S2 with K_s-band magnitude of 14.2, also referred to as S0-2, is one of the brightest stars in the cluster. The Keplerian orbital elements of this star improved noticeably after its periapse in 2002, although they could be determined very well even before that. The near-infrared (NIR) adaptive optics (AO) imaging after 2002 allowed the derivation of even more detailed orbital elements (Schödel et al. 2002; Ghez et al. 2003). The measurements of the radial velocities from the NIR spectroscopy resulted in the determination of M_{BH} and R_0 in addition to the Keplerian orbital elements (Ghez et al. 2003, 2005; Eisenhauer et al. 2003). The

results of these calculations were improved even more using multiple S-stars (e.g. Ghez et al. 2008; Gillessen et al. 2009b; Boehle et al. 2016; Gillessen et al. 2017). The orbital period of S2 is ~16.2 yr. It has the second shortest orbital period in the S-cluster, which has allowed us to observe it long enough to determine the orbit with a very high precision (Ghez et al. 2003; Gillessen et al. 2009b, 2017). The velocity of S2 at the periapse is ~0.2 in unit of the speed of light. This indicates a large enough periapse shift (10′.8 assuming a semimajor axis size of 0′′.124, an eccentricity of 0.88, and a M_{BH} of 4×10^6 $M_\odot$) that can be observed with today's instruments (Jaroszynski 1998; Fragile & Mathews 1999; Rubilar & Eckart 2001; Weinberg et al. 2005).

The next suitable star in the cluster is **S38**, also known as S0-38, with K_s-band magnitude of 17. Since a large portion of the orbit of S38 has been covered by observations, it is a favorable star for determining the gravitational potential of Sgr A* along with S2. The rest of the orbit of S38 will be observed in the very near future. In general, the center of the Galaxy is a very crowded region. However, it seems like that the region in the east of Sgr A* is even more crowded by the stars than the region in the west. Luckily, S38 spends most of its orbital period in the less crowded region in the west of Sgr A*, which makes it more immune to source confusion. Another benefit of using the orbit of S38 along the orbit of S2 is that the orbit of S38 is perpendicular to the orbit of S2. This is especially beneficial since we are limited in determining the north-south motion of Sgr A* as a result of large uncertainties in positioning S2 during, and shortly before and after its periapse. Boehle et al. (2016) use the orbit of S2 and S38 simultaneously to determine M_{BH} and R_0.

Another significant star is **S0-102** (Meyer et al. 2012), which is possibly identical to an earlier reported source, S55. It has a K_s-band magnitude of 17.1 with the shortest observed period of ~ 12 yr among the S-stars. Unfortunately the radial velocity of this star is not determined so far due to its faintness.

2.2 Observations

The first step towards the goals in this thesis is the observation. The observations were done with the NACO (NAOS-CONICA) instrument installed initially at the fourth (from 2001 to 2013) and afterwards the first (from 2014 on) unit telescope (UT) at the Very Large Telescope (VLT) of the European Southern Observatory (ESO). More details about the telescope and the instrument are given in Sect. 1.4.1. For astrometry of the stars in the GC, I used the K_s-band (2.18 μm) images acquired by the S13 (with 13 mas pix^{-1} scale) and S27 (with 27 mas pix^{-1} scale) cameras with specifications given in Table 1.1. The list of the observations from 2002 to 2015 is given in Table 2.1.

2.3 Near-Infrared Data

After the standard data reduction steps explained in Sect. 1.4.3 (flat-fielding, sky subtraction, and bad-pixel correction), I use a cross-correlation algorithm in order to align the dithered exposures. Then, I select the K_s-band images with good quality manually. I use the reduced images by Witzel et al. (2012, Table 2) from 2003 to

***Table 2.1**: List of observations by the NACO instrument at the Very Large Telescope.*

Date (UT)	Camera	Project ID
31.07.2002	S13	60.A-9026(A)
13.06.2003	S13	713-0078(A)
16.06.2003	S13	713-0078(A)
06.07.2004	S13/S27	073.B-0775(A)
08.07.2004	S13	073.B-0775(A)
29.07.2004	S13	273.B-5023(C)
09.04.2005	S13	073.B-0085(I)
13.05.2005	S27	073.B-0085(E)
20.06.2005	S27	073.B-0085(F)
01.06.2006	S27	077.B-0552(A)
29.06.2006	S13	077.B-0014(C)
02.08.2006	S13	077.B-0014(D)
23.09.2006	S13	077.B-0014(F)
20.10.2006	S13	078.B-0136(A)
17.03.2007	S13	078.B-0136(B)
20.03.2007	S13	078.B-0136(B)
01.04.2007	S27	179.B-0261(A)
04.04.2007	S13	179.B-0261(A)
06.04.2007	S27	179.B-0261(A)
16.06.2007	S13	179.B-0261(H)
23.02.2008	S13	179.B-0261(L)
13.03.2008	S13	179.B-0261(L)
08.04.2008	S13	179.B-0261(M)
28.05.2008	S27	081.B-0648(A)
16.06.2008	S13	179.B-0261(T)
07.08.2008	S13	179.B-0261(N)
16.09.2008	S13	179.B-0261(U)
20.04.2009	S13	178.B-0261(W)
03.05.2009	S13	183.B-0100(G)
03.07.2009	S13	183.B-0100(D)
10.08.2009	S13	183.B-0100(I)
12.08.2009	S13	183.B-0100(I)
19.09.2009	S13	183.B-0100(J)
12.06.2010	S13	183.B-0100(T)
16.06.2010	S13	183.B-0100(U)
17.05.2011	S27	183.B-0100(V)
27.05.2011	S13	087.B-0017(A)
17.05.2012	S13	089.B-0145(A)
05.06.2013	S27	091.B-0172(A)
28.06.2013	S13	091.B-0183(A)
01.08.2015	S13	095.B-0003(A)

mid-2010, and Eckart et al. (2013, Table 1) and Shahzamanian et al. (2015, Table 1) from 2002 to 2012. To connect the NIR data to the radio reference frame, the pixel positions of the SiO maser stars IRS9, IRS10EE, IRS12N, IRS15NE, IRS17, IRS19NW, IRS28, and SiO-15 in seven 27 mas pix^{-1} scale images from 2004 to 2013 are measured. The location of these sources in an infrared (IR) K-band image is shown in Fig. 2.1. Additionally, the pixel positions of IRS16SW (S95), IRS16C (S97), S65, S96, S67, and S2 are measured in both the 27 mas pix^{-1} and 13 mas pix^{-1} scale images with the similar epochs. The 13 mas pix^{-1} scale images are diconvoluted with the Lucy-Richardson deconvolution algorithm (see Sect. 1.4.4.1) prior to the measurements of the positions of the stars. These sources are needed for the connection between the S27 and S13 images, since SiO masers are not covered in the field of view of S13 images.

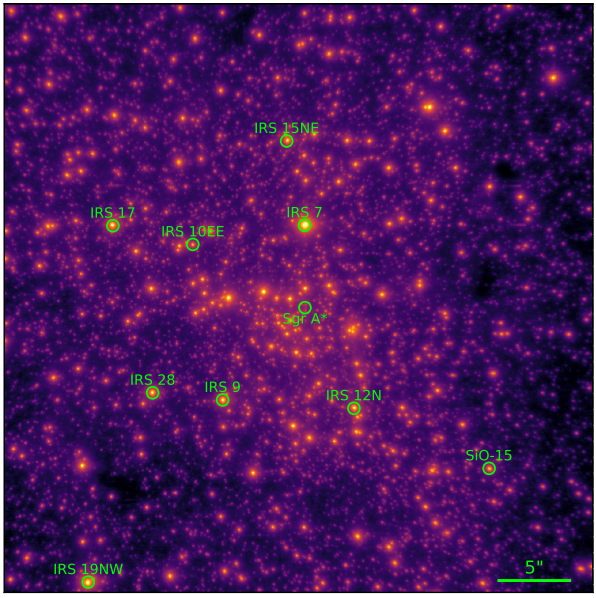

***Figure 2.1**: K_s-band image of the inner 20″ of the GC in 2005. The SiO maser stars in this region and Sgr A* are marked with circles. The linear scale is at the bottom right of the image.*

Since the pixel positions in the 13 mas pix^{-1} images are then transformed to a reference frame with Sgr A* at the center, only the images taken with Sgr A* flaring, are used. In addition to the sources mentioned above, in all the selected 13 mas pix^{-1} scale images, the offsets of five reference stars, S7, S10, S26, S30, and S65 with respect to Sgr A* are measured. These stars are then used for the image distortion calculations. The offsets of the three candidate stars, S2, S38, and S0-102/S55 are also measured in all these images for the final gravitational potential and orbital analysis.

The radial velocity data of S2 are provided by Gillessen et al. (2009b), who have used the AO assisted field spectrometer SINFONI. This instrument is installed on the fourth unit telescope of the VLT. Gillessen et al. (2009b) and Boehle et al. (2016) provide the radial velocity data for S38. As mentioned before, there is no radial velocity data for S0-102/S55.

2.3.1 Astrometric Accuracy

As shown by Gillessen et al. (2009b), the error of the resulting mean one-dimensional position in the S13 NACO data is as large as 1 mas. Plewa et al. (2015) conclude that the infrared reference frame does not show pumping (v_r/r), neither does it show rotation (v_ϕ/r) relative to the radio reference system to within $\sim$7.0 μas yr^{-1} arcsec^{-1}. In order to show this, they use the average velocity differences in the radial and tangential direction. This will amount to an upper limit of $\sim$0.14 mas arcsec^{-1} in a period of 20 yr, which is 0.1–0.2 mas across the 1 arcsec diameter of the central S-cluster. Therefore, the combined error, i.e. the residual distortions, the rotation, and the transformation in the S-cluster diameter is less than $\sim$1.2 mas.

A star's individual position has an accuracy of less than a tenth of a pixel using a Gaussian fit to its position. This is much better for a bright S-star, i.e. 1–2 mas per single epoch. For Sgr A* due to the crowding in the center and the presence of S17 close to its position in a few years of the data, estimating the accuracy is more complicated. For a bright flaring event, the accuracy of the position of Sgr A* is 1–2 mas. But this goes up to about a half of a pixel (6 mas) for a fainter flare emission, especially with S17 nearby. An accuracy of only a fraction of a mas is possible for sufficiently bright members of the cluster (Plewa et al. 2015).

2.3.2 Connection between the NIR and Radio Reference Frames

To connect the NIR and radio data, from each individual data set, the instrumental imaging parameters up to the second order are extracted. The pixel position of the i^{th} star given by (x_i, y_i) is obtained using the corrected offset coordinates from the base position (a_0, b_0) given by $(\Delta x_i, \Delta y_i)$ as:

$$x_i = a_0 + a_1\Delta x_i + a_2\Delta y_i + a_3\Delta x_i^2 + a_4\Delta x_i\Delta y_i + a_5\Delta y_i^2 \tag{2.1}$$

and

$$y_i = b_0 + b_1\Delta x_i + b_2\Delta y_i + b_3\Delta x_i^2 + b_4\Delta x_i\Delta y_i + b_5\Delta y_i^2 \ . \tag{2.2}$$

The first-order parameters in the equations 2.1 and 2.2 relate the camera rotation angle α_r and the pixel scales ρ_x and ρ_y in arcsec pix^{-1}. The second-order parameters give the image distortions. Using the positions and proper motions of eight maser stars in the radio wavelength from Plewa et al. (2015), for each data set, the 12 instrumental parameters are calculated by comparison. In order to calculate these parameters, an over-determined non-linear equation has to be solved for all eight maser sources, by means of orthonormalization of a 12×8 matrix. After solving the equation, it is determined that the first-order scaling parameters are typically greater than 10^3 of the second-order distortion parameters and pixel scale parameters. Then the instrumental parameters are corrected and the final position errors are found to be 1–10 mas for the bright maser sources for each data set.

The 27 mas pix^{-1} scale images have larger field and therefore contain the infrared counterparts of the maser stars. These images should be connected to the higher resolution 13 mas pix^{-1} scale images containing the S-stars and Sgr A* flaring in the similar epochs. Therefore, the procedure above is applied on the selected images. The connection is done using the offsets of the six overlap sources: IRS16SW (S95), IRS16C (S97), S65, S96, S67, and S2, to Sgr A*. These sources can be easily located in both the 27 mas pix^{-1} scale and 13 mas pix^{-1} scale images. The location of these sources in a 13 mas pix^{-1} scale image and a 27 mas pix^{-1} scale image are shown in Figs. 2.2 and 2.3, respectively.

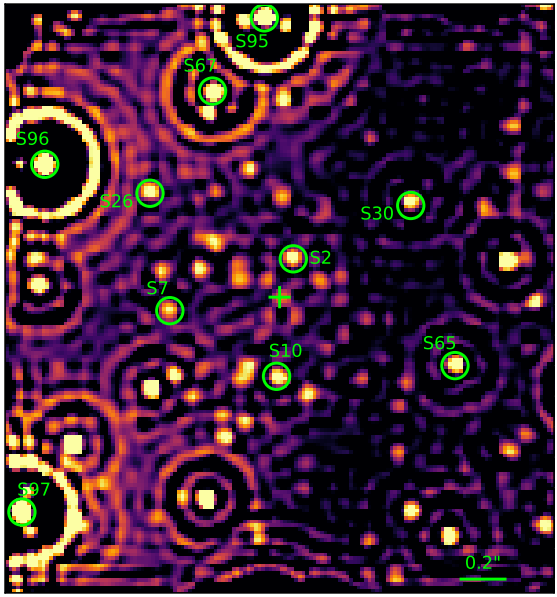

***Figure 2.2**: 13 mas pix^{-1} scale NIR K_s-band image taken with the NACO instrument of the VLT in 2011. The location of the overlapping stars between the 27 mas pix^{-1} scale and 13 mas pix^{-1} scale images and the reference stars are marked with circles. Sgr A* is shown with a plus in the center of the image. The image is deconvoluted using the LR deconvolution algorithm.*

Next, the NIR reference frame is connected to the radio frame using the distortion-corrected positions of the radio counterparts of the maser sources, from the projected trajectories given by Plewa et al. (2015). Here I assumed that the maser stars are almost co-spatial with their infrared counterparts. It is shown by Oyama et al. (2008) and Sjouwerman et al. (2004) that the maser spot shells are within 1 mas radius around the central stars. Therefore, my assumption is justified.

Finally, the motion of the infrared counter part of Sgr A* with respect to the radio frame is calculated. The infrared and radio positions of Sgr A* agree to within

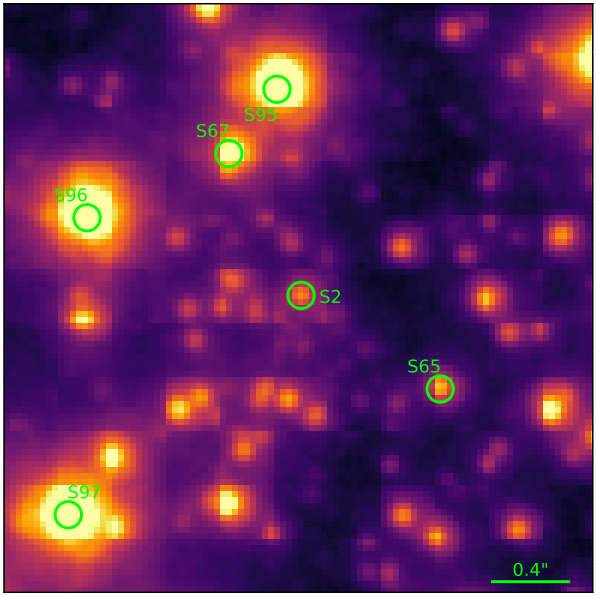

***Figure 2.3**: 27 mas pix^{-1} scale NIR K_s-band image taken with the NACO instrument of the VLT in 2011. The location of the overlapping stars between the 27 mas pix^{-1} scale and 13 mas pix^{-1} scale images are marked with circles.*

less than 1.4 mas and the proper motion is less than 0.3 mas yr^{-1} over the base line in time. This accuracy for the connection of the infrared and radio reference frame in the central cluster is approximately one order of magnitude bellow what is presented in Plewa et al. (2015). They find an accuracy of ~0.17 mas for the position and ~0.07 mas yr^{-1} for the velocity, in the epoch of 2009. Therefore, I conclude that in the two reference farmes, the positions of Sgr A* are in agreement and the S-stars are, to the first order, orbiting the infrared counterpart of Sgr A*.

These results can be compared to the expectations from the data. The positions of the stars are measured with an accuracy of 0.037–0.3 pix, which is approximately 1–10 mas, depending on the strength of the source. Therefore, the uncertainty of the connection of the NIR to the radio frame is dominated by the distortion of ~1 mas, similar to Plewa et al. (2015). Conservatively, I choose an accuracy of 10 mas for the determination of the positions. The rest of the uncertainties in the connection procedure are originated by:

1. The accuracy in the mosaicking of the 27 mas pix^{-1} fields to include the maser stars.

2. The measurements of the positions.

3. The connection procedure of the 27 mas pix^{-1} scale and the 13 mas pix^{-1} scale images using the six overlapping sources.

The mosaicking is influenced by 9 sources along the regions that overlap between the frames. One can presume that in the 13 mas pix^{-1} scale images, the accuracy of the determination of the positions is twice as large as the accuracy in the 27 mas pix^{-1} scale images. Therefore, the accuracy in determining the position of a single star is 0.5–5 mas in the 13 mas pix^{-1} scale frames. If all eight maser stars are used to find the single epoch positions, the accuracy of the measurements of the proper motions are at least 1.7 mas.

Figure 2.4 shows that the statistics of Sgr A* and the eight maser sources for a single epoch are in good agreement with this estimation. The analysis on the orbits of the S-stars in the next sections shows that for the faint members of the cluster, the accuracy in the determination of the positions is ~3 mas.

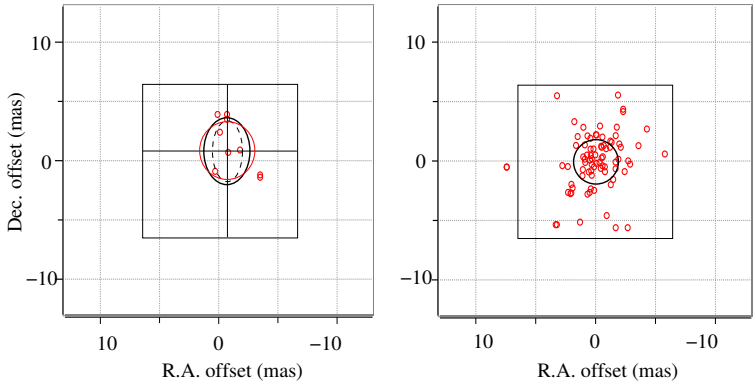

***Figure 2.4**: **Left panel:** Statistics for the offset between the infrared and radio positions of Sgr A* in a single epoch. The thin red ellipse is the median and the median deviation of the offsets for the right ascension and the declination of 1.8 mas × 0.9 mas. The zero offset point is located inside the median deviation. The black thick ellipse shows the standard deviations of 2.0 mas × 1.4 mas. A black dashed ellipse shows the equivalent geometrical mean of 1.7 mas. **Right panel:** Statistics for all the maser sources in a single epoch is depicted, which is almost centered on the zero offset point. The black circle shows the standard deviation of 1.8 mas. Credit: Parsa et al. (2017).*

2.3.3 Derivation of the Positions

While the procedure described above allows me to directly use the offset positions from Sgr A* as an input for the orbit calculations, I verify the result with a bootstrapping procedure justified in the Appendix, Sect. 5.1. Through the calculations done in the previous section, the position of the stars and Sgr A* can be measured with respect to the radio reference frame. As described in Sect. 2.3, I choose 33 images with 13 mas pix^{-1} scale taken by the NACO S13 camera in which Sgr A*

is flaring in the infrared and therefore, can be directly located in the coordinate system. The location of the three candidate stars, S2, S38, and S0-102/S55 are inspected in all these images. The Lucy-Richardson deconvolution is necessary for locating S0-102/S55. The locations of the candidate stars are shown in Figs. 2.5 to 2.8 in each year.

In addition, five other stars: S7, S10, S26, S30, and S65 (see Fig. 2.2), which are in the vicinity of the candidate stars, are located in all these images. These stars are chosen from the bright sources with previously reported linear motions and relatively low velocities (Gillessen et al. 2009b; Plewa et al. 2015; Gillessen et al. 2017). Moreover, these five stars are isolated, which is why I could easily locate them in each image without any confusion or overlapping with other stars.

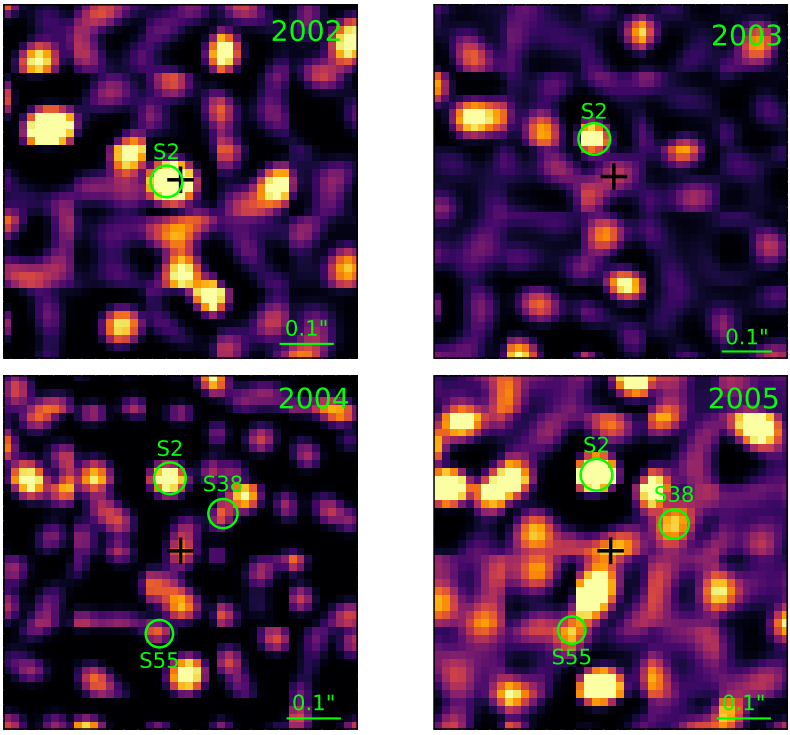

***Figure 2.5**: Location of S2, S38, and S0-102/S55 in the central ~0″.7 in years 2002 to 2005, in the NIR K_s-band images with 13 mas pix^{-1} scale. All images are deconvoluted, using the Lucy-Richardson deconvolution technique. Sgr A* is shown with a black plus in the center of the image.*

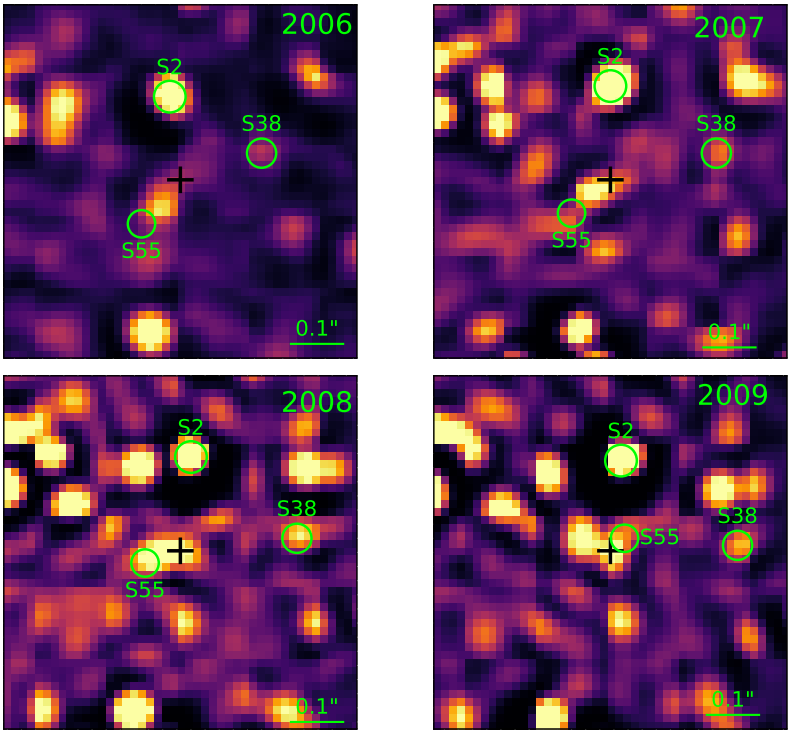

***Figure 2.6**: Location of S2, S38, and S0-102/S55 in the central ~0″.7 in years 2006 to 2009, in the NIR K_s-band images with 13 mas pix^{-1} scale. All images are deconvoluted, using the Lucy-Richardson deconvolution technique. Sgr A* is shown with a black plus in the center of the image.*

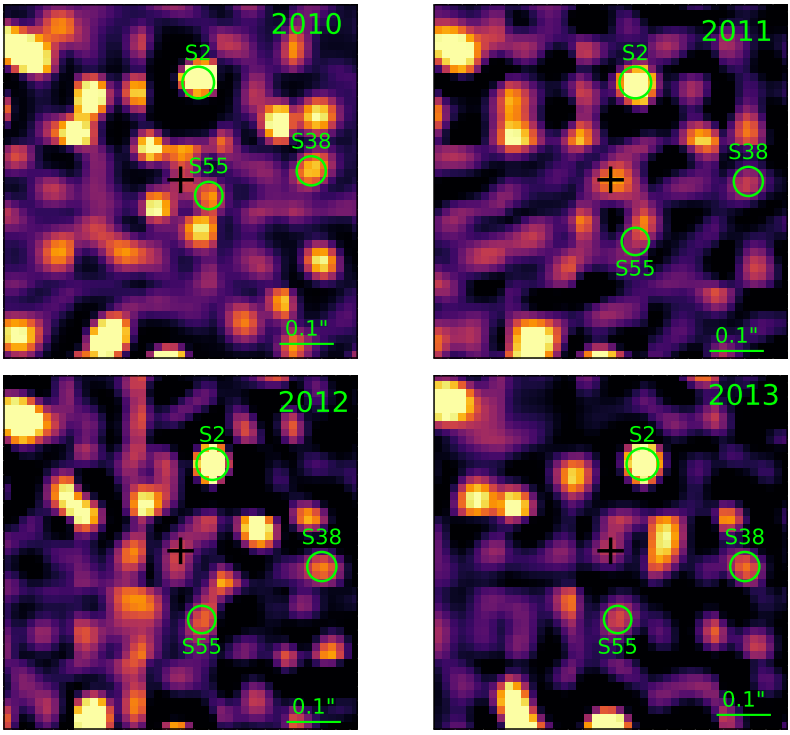

***Figure 2.7**: Location of S2, S38, and S0-102/S55 in the central ~0″.7 in years 2010 to 2013, in the NIR K_s-band images with 13 mas pix^{-1} scale. All images are deconvoluted, using the Lucy-Richardson deconvolution technique. Sgr A* is shown with a black plus in the center of the image.*

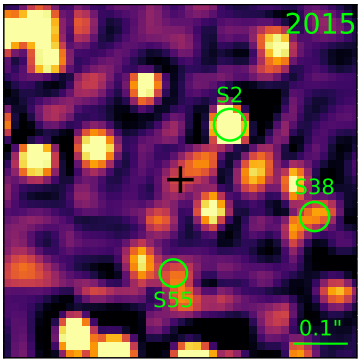

***Figure 2.8**: The location of S2, S38, and S0-102/S55 in the central ~0″.7 in year 2015, in the NIR K_s-band images with 13 mas pix^{-1} scale. All images are deconvoluted, using the Lucy-Richardson deconvolution technique. Sgr A* is shown with a black plus in the center of the image.*

The pixel positions are then extracted for all the sources. I use a two-dimensional Gaussian fit for isolated (not overlapping) stars. If two or more sources are overlapping partially in some epochs, pixel positioning cannot be done with a Gaussian fit easily. Therefore, I measure the positions manually, and thus associate them with larger measurement errors.

In all the 33 images, S2 can be easily detected from 2002 to 2015. However, S38 is confused with other sources in the very crowded region around Sgr A* before the year 2004. Therefore, I remove all the measurements of this star before this epoch from my data set and keep only the measurements from 2004 to 2015. S0-102/S55 is very faint, 16 times fainter than S2 according to Meyer et al. (2012). Its is also located in a very crowded region close to Sgr A*, in all epochs. There are epochs that the location of the star is not very clear and this leaves me with 25 measurements from the total of 33 images from 2004 to 2015.

Next, the positions in pixels are transformed into a reference frame by finding the linear equations of motion of the five reference stars through the minimum χ^2 method. The χ^2 method is explained in the Appendix, Sect. 5.2. The uncertainties of the fits are found using the bootstrapping technique explained in the Appendix, Sect. 5.3. The results are reported in Table 2.2.

For each of the reference stars in each of the images, the residuals between the measured positions and the equivalent positions in the linear fit are calculated. These residuals are then averaged in each image. The resulting mean residual in each image is then used to correct the distortion in the image for the positions of all the sources, treating Sgr A* as one of the sources. For the mean of the residuals in each image, the standard deviation of the mean is calculated. The standard deviation is then added through the error propagation to the uncertainty of the measurement of each source in that specific image as the uncertainty of the reference frame. This is a systematic error in my data. Next, the offset to the position of Sgr A* for each source is calculated and then transformed to an

***Table 2.2**: Equations of motion of the five reference stars. Credit: Parsa et al. (2017).*

Star	t_0 (yr)	ΔR.A. (arcsec)	ΔDec. (arcsec)
S7	2002.578	(0.5146 ± 0.0026) + (-0.0040 ± 0.0001)Δt	(-0.0421 ± 0.0020) + (-0.0016 ± 0.0002)Δt
S10	2002.578	(0.0552 ± 0.0023) + (-0.0045 ± 0.0001)Δt	(-0.3736 ± 0.0020) + (0.0037 ± 0.0002)Δt
S26	2002.578	(0.5105 ± 0.0027) + (0.0060 ± 0.0001)Δt	(0.4296 ± 0.0020) + (0.0016 ± 0.0004)Δt
S30	2002.578	(-0.5434 ± 0.0024) + (-0.0001 ± 0.0003)Δt	(0.3806 ± 0.0021) + (0.0036 ± 0.0002)Δt
S65	2002.578	(-0.7575 ± 0.0034) + (0.0023 ± 0.0006)Δt	(-0.2684 ± 0.0033) + (-0.0015 ± 0.0006)Δt

astrometric position. The result of this procedure is reported for S2, S38, and S0-102/S55 in Table 2.3, Table 2.4, and Table 2.5, respectively.

A linear equation of motion is fitted to the positions of the infrared counterpart of Sgr A* in the NIR reference frame, after the transformation explained above is applied. I use the minimum χ^2 method for calculating the fitting parameters and the bootstrapping method for the uncertainties. The reference epoch is 2002.66.

$$\alpha(\text{mas}) = (1.9 \pm 2.5) - (0.21 \pm 0.37) \times (t(\text{yr}) - 2002.66) \tag{2.3}$$

$$\delta(\text{mas}) = (-0.4 \pm 2.4) + (0.06 \pm 0.41) \times (t(\text{yr}) - 2002.66). \tag{2.4}$$

This linear fit (Equation 2.3) can be compared to a similar fit done by Gillessen et al. (2009b). The comparison is visualized in Fig. 2.9. The solid blue line shows the results of this study and the dashed red line shows the reported linear fit in Gillessen et al. (2009b).

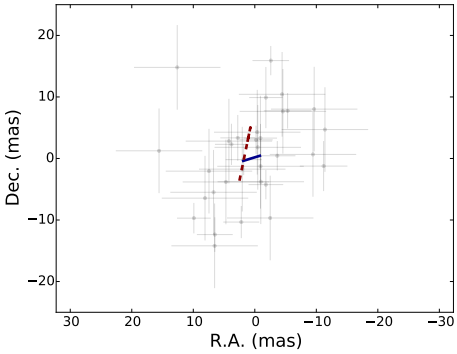

***Figure 2.9**: Linear motion fit to the NIR distortion-corrected counterpart data of Sgr A* shown with grey pluses indicating the uncertainty of each point. The solid blue line is the fit done in this study compared to the dashed red line from a study in Gillessen et al. (2009b). Credit: Parsa et al. (2017).*

2.4 Newtonian and Relativistic Models

A Keplerian orbit with six orbital elements can describe the Newtonian motion for a star around a SMBH. I choose the six orbital elements to be the semimajor axis, eccentricity, inclination, argument of periapse, longitude of the ascending node, and the periapse passage time. By defining these six elements, a unique orbit in three dimensions can be described and all other orbital elements can be calculated from them. This can be useful in finding the state vectors at each epoch. More details about a Keplerian orbit and its orbital elements are in Sect. 1.2. A Keplerian model is sufficient for almost all the S-stars. However, in addition to this model, a relativistic model is needed for the stars which are orbiting close enough to Sgr A*

***Table 2.3**: Astrometric measurements of S2. Credit: Parsa et al. (2017).*

Date (Decimal)	ΔR.A. (arcsec)	ΔDec. (arcsec)	ΔR.A. Error (arcsec)	ΔDec. Error (arcsec)
2002.578	0.0386	0.0213	0.0066	0.0065
2003.447	0.0385	0.0701	0.0009	0.0010
2003.455	0.0393	0.0733	0.0012	0.0012
2004.511	0.0330	0.1191	0.0010	0.0008
2004.516	0.0333	0.1206	0.0009	0.0006
2004.574	0.0315	0.1206	0.0009	0.0009
2005.268	0.0265	0.1389	0.0007	0.0011
2006.490	0.0141	0.1596	0.0065	0.0065
2006.584	0.0137	0.1609	0.0033	0.0007
2006.726	0.0129	0.1627	0.0033	0.0007
2006.800	0.0107	0.1633	0.0033	0.0007
2007.205	0.0064	0.1681	0.0004	0.0007
2007.214	0.0058	0.1682	0.0004	0.0008
2007.255	0.0069	0.1691	0.0010	0.0007
2007.455	0.0047	0.1709	0.0004	0.0006
2008.145	-0.0076	0.1775	0.0007	0.0012
2008.197	-0.0082	0.1780	0.0007	0.0011
2008.268	-0.0084	0.1777	0.0006	0.0008
2008.456	-0.0118	0.1798	0.0006	0.0009
2008.598	-0.0126	0.1802	0.0009	0.0010
2008.708	-0.0127	0.1806	0.0008	0.0013
2009.299	-0.0216	0.1805	0.0006	0.0009
2009.334	-0.0218	0.1813	0.0006	0.0009
2009.501	-0.0233	0.1803	0.0005	0.0008
2009.605	-0.0266	0.1800	0.0012	0.0015
2009.611	-0.0249	0.1806	0.0006	0.0008
2009.715	-0.0260	0.1804	0.0006	0.0008
2010.444	-0.0347	0.1780	0.0013	0.0021
2010.455	-0.0340	0.1774	0.0008	0.0013
2011.400	-0.0430	0.1703	0.0009	0.0017
2012.374	-0.0518	0.1617	0.0012	0.0016
2013.488	-0.0603	0.1442	0.0006	0.0019
2015.581	-0.0690	0.1010	0.0014	0.0010

***Table 2.4**: Astrometric measurements of S38. Credit: Parsa et al. (2017).*

Date (Decimal)	ΔR.A. (arcsec)	ΔDec. (arcsec)	ΔR.A. Error (arcsec)	ΔDec. Error (arcsec)
2004.511	-0.0667	0.0576	0.0017	0.0016
2004.516	-0.0673	0.0690	0.0066	0.0065
2005.268	-0.1178	0.0583	0.0065	0.0066
2006.490	-0.1544	0.0558	0.0065	0.0065
2006.584	-0.1600	0.0613	0.0073	0.0078
2006.726	-0.1684	0.0550	0.0009	0.0008
2006.800	-0.1690	0.0549	0.0011	0.0009
2007.205	-0.1851	0.0513	0.0005	0.0008
2007.214	-0.1853	0.0506	0.0005	0.0008
2007.255	-0.1807	0.0524	0.0010	0.0007
2007.455	-0.1898	0.0474	0.0005	0.0065
2008.145	-0.2058	0.0363	0.0009	0.0013
2008.197	-0.2065	0.0359	0.0008	0.0011
2008.268	-0.2049	0.0338	0.0007	0.0009
2008.456	-0.2111	0.0325	0.0008	0.0010
2008.598	-0.2141	0.0346	0.0010	0.0010
2008.708	-0.2175	0.0338	0.0010	0.0013
2009.299	-0.2315	0.0244	0.0007	0.0009
2009.334	-0.2310	0.0241	0.0007	0.0009
2009.501	-0.2344	0.0216	0.0006	0.0008
2009.605	-0.2360	0.0156	0.0012	0.0015
2009.611	-0.2350	0.0202	0.0007	0.0008
2009.715	-0.2363	0.0178	0.0006	0.0009
2010.444	-0.2415	0.0053	0.0013	0.0021
2010.455	-0.2437	0.0009	0.0009	0.0014
2011.400	-0.2425	-0.0113	0.0010	0.0017
2012.374	-0.2519	-0.0251	0.0013	0.0017
2013.488	-0.2450	-0.0409	0.0007	0.0019
2015.581	-0.2320	-0.0617	0.0016	0.0013

to show relativistic effects. The orbit of these stars deviate from a purely Keplerian orbit. Also, the relativistic model is needed for the tests of GR.

The post-Newtonian (PN) approximation is implemented for approximate solution to the equation of motion of a particle bound to a gravitational field with a small velocity relative to the speed of light (see Weinberg (1972); Will (1993) and Schneider (1996)). More details about PN approximation can be found in Sect. 1.3.1. Therefore, for the relativistic model of the motion of a star in the gravitational field of the SMBH, I use a first-order PN approximation called the "Einstein-Infeld-Hoffmann" equation (Einstein et al. 1938). Next, I rewrite the equation for the gravitational potential $\phi = -GM_{BH}/r$ of a compact mass distribution M_{BH} and with a constant velocity $\vec{v_{bh}}$:

***Table 2.5**: Astrometric measurements of S0-102/S55. Credit: Parsa et al. (2017).*

Date (Decimal)	ΔR.A. (arcsec)	ΔDec. (arcsec)	ΔR.A. Error (arcsec)	ΔDec. Error (arcsec)
2004.511	0.0549	-0.1552	0.0066	0.0065
2004.516	0.0711	-0.1536	0.0066	0.0065
2005.268	0.0707	-0.1437	0.0065	0.0066
2006.490	0.0731	-0.1199	0.0065	0.0065
2006.584	0.0749	-0.1220	0.0065	0.0065
2006.726	0.0790	-0.1180	0.0066	0.0065
2006.800	0.0731	-0.1169	0.0066	0.0065
2007.205	0.0835	-0.0883	0.0065	0.0065
2007.255	0.0797	-0.0763	0.0066	0.0065
2007.455	0.0784	-0.0635	0.0065	0.0065
2008.145	0.0659	-0.0346	0.0065	0.0066
2008.197	0.0641	-0.0338	0.0065	0.0066
2008.268	0.0711	-0.0309	0.0065	0.0066
2008.456	0.0692	-0.0167	0.0065	0.0066
2008.598	0.0678	-0.0144	0.0066	0.0066
2008.708	0.0620	-0.0058	0.0066	0.0066
2009.334	-0.0017	0.0358	0.0065	0.0066
2009.501	-0.0257	0.0291	0.0065	0.0066
2009.605	-0.0305	0.0243	0.0066	0.0067
2009.715	-0.0390	0.0378	0.0065	0.0066
2010.444	-0.0620	-0.0453	0.0066	0.0068
2010.455	-0.0523	-0.0404	0.0018	0.0020
2011.400	-0.0492	-0.1080	0.0066	0.0067
2012.374	-0.0345	-0.1180	0.0013	0.0029
2013.488	-0.0134	-0.1380	0.0007	0.0019
2015.581	0.0239	-0.1678	0.0016	0.0066

$$\frac{d\vec{v}_\star}{dt} = -\frac{GM_{BH}}{c^2 r_\star^3}\left\{\vec{r}_\star\left[c^2 + v_\star^2 + 2v_{BH}^2 - 4\left(\vec{v}_\star.\vec{v}_{BH}\right) - \frac{3}{2r_\star^2}\left(\vec{r}_\star.\vec{v}_{BH}\right)^2 - 4\frac{GM_{BH}}{r_\star}\right] - \left[\vec{r}_\star.\left(4\vec{v}_\star - 3\vec{v}_{BH}\right)\right]\left(\vec{v}_\star - \vec{v}_{BH}\right)\right\}. \tag{2.5}$$

Where M_{BH} and $\vec{v}_\bullet$ are the mass and the velocity vector of the black hole, and $\vec{r}_\star$ and $\vec{v}_\star$ are the position and velocity vector of the star. I assume that the extended mass inside the orbit of the star is negligible and the star is only under the influence of the mass of the black hole. If I consider only a small and negligible proper motion for the central black hole, I can reduce Equation 2.5 to the equation given by Rubilar & Eckart (2001):

$$\frac{d\vec{v}_\star}{dt} = -\frac{GM_{BH}}{c^2 r_\star^3}\left[\vec{r}_\star\left(c^2 - 4\frac{GM_{BH}}{r_\star} + v_\star^2\right) - 4\vec{v}_\star\left(\vec{v}_\star.\vec{r}_\star\right)\right]. \tag{2.6}$$

This equation is useful when the orbital period is short enough that the small proper motion of the black hole is negligible. Integrating the equations of motion, Equation 2.5 and 2.6, using the fourth-order Runge-Kutta integration method, gives me the orbit of the star showing the first-order PN effects. The Runge-Kutta method is explained in the Appendix, Sect. 5.4. However, I need to define the starting position and velocity vector of the star in three dimensions in Equation 2.6 (six parameters). In Equation 2.5, I need to define the initial state vector of the star and the black hole as initial parameters (12 parameters), in addition to the mass of the black hole and the distance to it.

2.5 Stellar Orbits

In order to find the orbit of S2, S38, and S0-102/S55 and the drift motion of the black hole, first I write the equation of motion (Equation 2.5) for each of the stars. Then I fit the model to the astrometric data for all three stars and the radial velocity data for S2 and S38 using the minimum χ^2 method, simultaneously. I had to scale the measurements and reference frame errors such that the reduced $\chi^2 \geq 1$. Therefore, I had to find 26 parameters, simultaneously. The best fit is demonstrated in Fig. 2.10 for S2, S38, S0-102/S55, and the drift motion of Sgr A*.

Next, I apply the Markov-Chain Monte Carlo (MCMC) technique in order to find the parameters of the fits for both Newtonian and post-Newtonian models. The MCMC technique is explained in detail in the Appendix, Sect. 5.5. In case of the Keplerian models, six orbital parameters of the stars, and the six initial parameters of the state vectors of the black hole in addition to the mass of the black hole and the distance to the GC have to be determined. The MCMC technique determines the 1σ uncertainties of the fits as well.

First, I use a Keplerian model. The MCMC method is time consuming; therefore I use initial values for the desired parameters that are determined via a minimum χ^2 method. This way the chains are more efficient and converge faster. I apply the method for S2 as the best candidate star for determining the gravitational potential parameters of the black hole. Then I apply it to S2 and S38 simultaneously, and as I expected the results are improved. Then I add S0-102/S55 to the other two stars and apply the method again and consequently achieved the best estimates for all the desired parameters. Figure 2.11 is a cut of the 1- and 2-dimensional histograms of these best estimates. The rest of the parameters are not shown here, since the number of the parameters is large and it affects the readability. The one-dimensional histograms along the diagonal are the marginalized distributions for each of the desired gravitational potential parameters. The posterior probability distributions are compact, which means that the parameters are constrained well. The correlations between some of the parameters are expected, especially between M_{BH} and R_0.

Subsequently, I change the model from Newtonian to PN. I fit the data again for the parameters, i.e. the reference epoch position and the velocity, using a χ^2 method. The resulting values are the initial parameters in the MCMC technique. Similar to the Newtonian case, I apply the method on S2 alone, on S2 and S38 together, and finally on S2, S38, and S0-102/S55 simultaneously to improve the results. The estimates for all the orbital elements and gravitational potential parameters

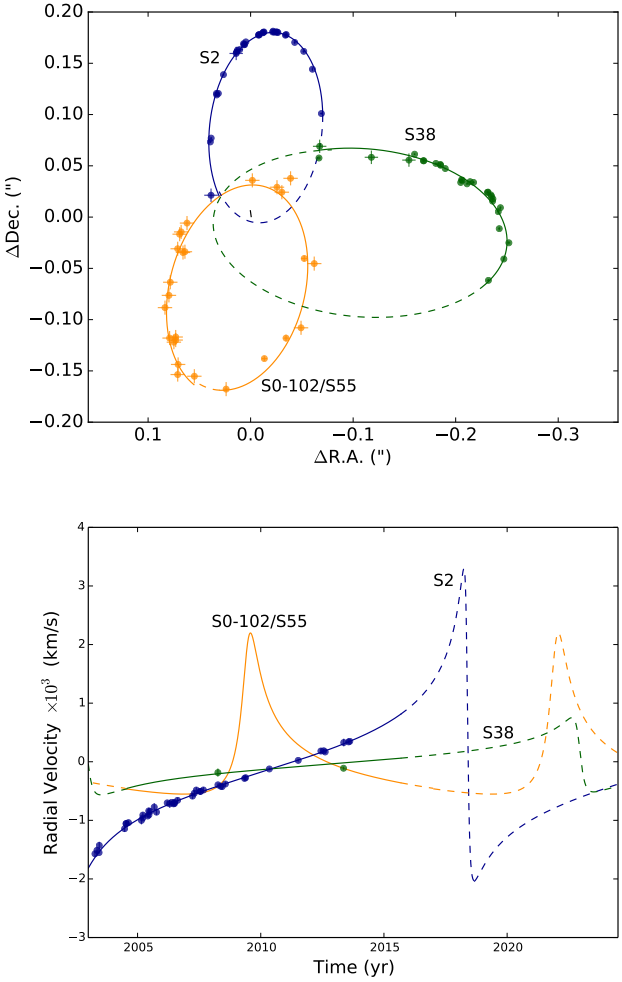

***Figure 2.10**: Best post-Newtonian orbital fit of S2, S38, S0-102/S55, and the drift motion of Sgr A* using Equation 2.5 and the minimum χ^2 method. The points with error bars are the data and the solid lines are the fits. The dashed sections are the extrapolation of the motions in order to present one full orbit. S2 data and its orbit are in blue, S38 data and its orbit are in green, and S0-102/S55 data and its orbit are in orange. The proper motion of the black hole is in black. Top panel credit: Parsa et al. (2017).*

including M_{BH} and R_0 and their 1σ uncertainties are reported in Table 2.6. The differences in the state vectors of the black hole are mainly due to the difference in the reference epochs of the models. For the Newtonian model, the reference epoch is July 2002 and for the PN model, it is April 2002.

2.6 Discussion

2.6.1 Comparison to the Litrature

The calculations from the results of the orbital fitting with Newtonian models and using three stars in Table 2.6, and the relation between the semimajor axis and the period

$$p = 2\pi \sqrt{\frac{a^3}{GM_{BH}}}\,, \tag{2.7}$$

indicate a periapse time of 2018.51 ± 0.22 for S2. Boehle et al. (2016) estimate an even earlier date, 2018.267 ± 0.04. However, for both predictions the observation conditions of the GC is optimal. The anticipation of detecting the gravitational redshift and periapse precession of S2, when it goes through its periapse, makes the event significant. Nevertheless, these GR effects are only observable if a detailed knowledge of the orbit of S2 and the gravitational potential parameters of Sgr A*, is at hand. Using the data from more than one star for the orbital fitting is one way of getting a better precision in finding these parameters. Using multiple stars for determining M_{BH} and R_0 has been reported by Gillessen et al. (2009b), Gillessen et al. (2017), and Boehle et al. (2016). For a combination of seventeen stars, Gillessen et al. (2017) find $M_{BH} = (4.28 \pm 0.10) \times 10^6\ M_\odot$ and $R_0 = 8.32 \pm 0.07$ kpc. These values are in agreement with the values from the multistar fit with a Newtonian model in this work (given in Table 2.6 in bold) within 2σ uncertainty. Boehle et al. (2016) find similar values of $M_{BH} = (4.02 \pm 0.16) \times 10^6\ M_\odot$ and $R_0 = 7.86 \pm 0.14$ kpc for the mass of the black hole and the distance to it using the Keck measurements for a simultaneous fit to the data of S2 and S38. These values are comparable with the values in this work, using the NACO data within 1σ and $\sim 2\sigma$ uncertainty, respectively.

As a result of the faintness of the source S55/S0-102, the radial velocity of this star cannot be determined. Hence, this star has not been used before for the determination of the mass of and the distance to the black hole. It is difficult to put constrain on the Newtonian shift of the periapse in the orbit of S2 since the mass within the orbit is not determined well. To overcome this obstacle, S55/S0-102 with its short orbital period and its large orbital coverage can be helpful to detect the bias in orbital fitting. However, including S55/S0-102 is not improving the derivation of the parameters for the Newtonian models.

Moreover, The estimates for M_{BH} and R_0 in the multistar fits are slightly larger in the value and uncertainty for the PN model than the Newtonian one. These values for the fits, based on only S2 data are in agreement with the multistar fit in this work and in the work by Ghez et al. (2008) and Gillessen et al. (2009b). The mass of and the distance to Sgr A* estimates from the combination of S2 and S38 with a PN model is in an acceptable agreement with the Newtonian ones. However, the

determined values of the parameters with the PN fit are again larger than with the Newtonian fit.

2.6.2 Overcoming the Bias in the Orbital Fitting

Although the results from the PN models are generally in agreement with the Newtonian ones, more constrains are needed on these models. In principal, a Newtonian model can predict the motion of the S-stars well. However, since it is expected to observe the relativistic effects in the orbit of S2, by using a Newtonian model, the possibility of determining them is disregarded. This can happen since the small precession of the orbit of S2 is compensated by the larger proper motion of Sgr A*, in one orbital period. In general, the drift motion of Sgr A* is a complication in finding the precession of S2, even if a PN model is used. In order to overcome the bias generated here, the orbit of at least two stars, such as S2 and S38 can be fitted simultaneously. However, at the present, the only complete orbit belongs to S2 and including other complete orbits can only happen in near future or if stars closer to Sgr A* are discovered. The discovery of these stars is achievable with higher angular resolution instruments, such as GRAVITY at the Very Large Telescope Interferometer (VLTI, Eisenhauer et al. 2011; Eckart et al. 2012; Grould et al. 2016) and telescopes such as the European Extremely Large Telescope (E-ELT, Brandl et al. 2016; Davies et al. 2016).

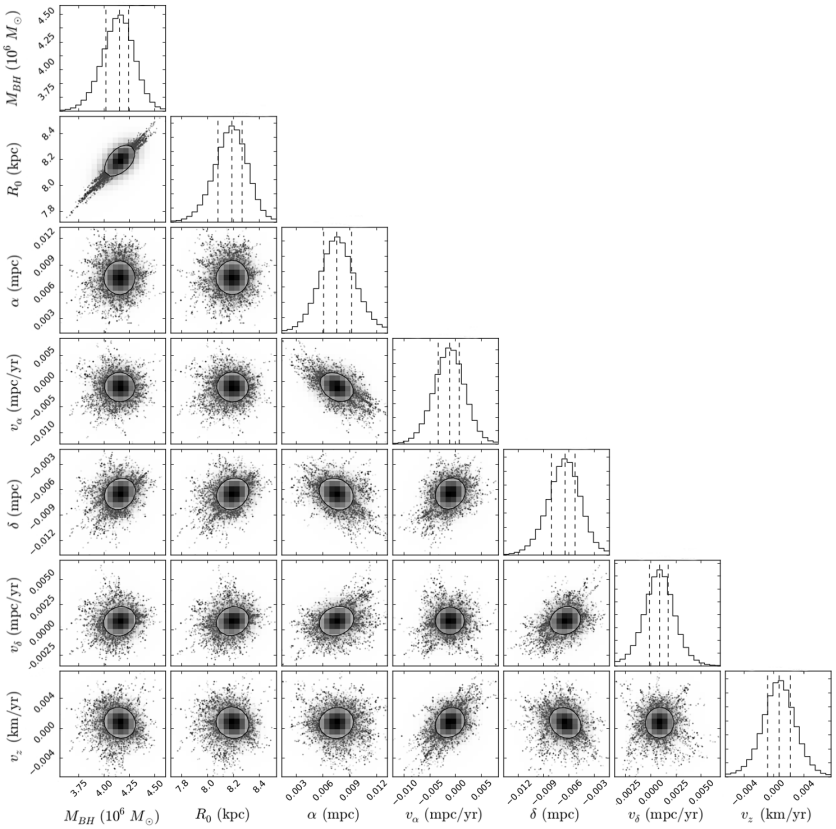

Figure 2.11*: Results of the MCMC method for the gravitational potential parameters of Sgr A*, using a Keplerian model for S2, S38, and S0-102/S55. In order to allow for the readability of the plots, I remove the rest of the histograms of the parameters. A two-dimensional cut of the parameter-space is shown in each panel. The one-dimensional histogram panels along the diagonal are the marginalized distributions. The 1σ uncertainties are shown by contours and the 0.16, 0.5, and 0.84 quantiles are shown with dashed lines. The complete plot can be found in the Appendix, Sect. 5.5 Credit: Parsa et al. (2017).*

***Table 2.6**: Results of the MCMC method for Newtonian and PN models.The explanation is given in the text. Credit: Parsa et al. (2017).*

		Keplerian			Relativistic	
Parameter (unit)	S2 Only	S2, S38	**S2, S38, S55/S0-102**	S2 Only	S2, S38	S2, S38, S55/S0-102
Black hole:						
M_{BH} (10^6 $M_\odot$)	$4.78^{+0.73}_{-0.47}$	$4.08^{+0.17}_{-0.17}$	$\mathbf{4.15^{+0.09}_{-0.13}}$	$4.37^{+0.20}_{-0.14}$	$4.16^{+0.02}_{-0.02}$	$4.72^{+0.08}_{-0.06}$
Distance (kpc)	$8.93^{+0.57}_{-0.44}$	$8.14^{+0.13}_{-0.12}$	$\mathbf{8.19^{+0.08}_{-0.11}}$	$8.50^{+0.16}_{-0.18}$	$8.29^{+0.01}_{-0.01}$	$8.53^{+0.07}_{-0.03}$
α (mas)	$0.31^{+0.95}_{-0.73}$	$0.21^{+0.04}_{-0.05}$	$\mathbf{0.19^{+0.04}_{-0.04}}$	$-0.03^{+0.17}_{-0.14}$	$0.03^{+0.07}_{-0.14}$	$0.07^{+0.08}_{-0.03}$
δ (mas)	$0.42^{+1.32}_{-0.82}$	$0.23^{+0.10}_{-0.10}$	$\mathbf{-0.16^{+0.03}_{-0.41}}$	$-0.01^{+0.06}_{-0.07}$	$-0.40^{+0.04}_{-0.05}$	$0.56^{+0.10}_{-0.08}$
v_α (mas yr^{-1})	$-0.21^{+0.36}_{-0.42}$	$-0.11^{+0.15}_{-0.18}$	$\mathbf{-0.03^{+0.05}_{-0.06}}$	$-0.07^{+0.11}_{-0.16}$	$0.56^{+0.05}_{-0.03}$	$0.19^{+0.12}_{-0.06}$
v_δ (mas yr^{-1})	$0.13^{+1.02}_{-0.66}$	$0.06^{+0.17}_{-0.13}$	$\mathbf{0.02^{+0.02}_{-0.03}}$	$0.12^{+0.23}_{-0.15}$	$-0.08^{+0.08}_{-0.14}$	$0.34^{+0.05}_{-0.04}$
v_z (km s^{-1})	$-10.3^{+50.7}_{-43.0}$	$-2.01^{+5.97}_{-7.84}$	$\mathbf{0.70^{+1.47}_{-1.52}}$	$-3.17^{+3.46}_{-2.05}$	$22.30^{+1.42}_{-2.08}$	$18.81^{+4.78}_{-9.00}$
S2:						
a ($''$)	$0.121^{+0.006}_{-0.004}$	$0.126^{+0.002}_{-0.002}$	$\mathbf{0.126^{+0.001}_{-0.001}}$			
e	$0.872^{+0.006}_{-0.007}$	$0.882^{+0.003}_{-0.004}$	$\mathbf{0.884^{+0.002}_{-0.002}}$			
i (°)	$138.1^{+2.0}_{-1.8}$	$136.38^{+0.77}_{-0.91}$	$\mathbf{136.78^{+0.36}_{-0.44}}$			
ω (°)	$68.9^{+1.9}_{-1.9}$	$71.1^{+1.3}_{-1.4}$	$\mathbf{71.36^{+0.65}_{-0.84}}$			
Ω (°)	$231.9^{+2.8}_{-2.6}$	$233.9^{+1.7}_{-1.9}$	$\mathbf{234.50^{+0.94}_{-1.09}}$			
T_p (yr)	$2002.27^{+0.04}_{-0.04}$	$2002.33^{+0.02}_{-0.02}$	$\mathbf{2002.32^{+0.02}_{-0.02}}$			
S38:						
a ($''$)		$0.139^{+0.002}_{-0.003}$	$\mathbf{0.140^{+0.001}_{-0.002}}$			
e		$0.819^{+0.005}_{-0.005}$	$\mathbf{0.818^{+0.005}_{-0.005}}$			
i (°)		$167.1^{+2.6}_{-2.8}$	$\mathbf{166.22^{+3.1}_{-2.4}}$			
ω (°)		$27.5^{+9.8}_{-7.4}$	$\mathbf{18.4^{+4.8}_{-5.8}}$			
Ω (°)		$106.8^{+9.5}_{-7.2}$	$\mathbf{101.8^{+4.6}_{-5.6}}$			
T_p (yr)		$2003.32^{+0.03}_{-0.04}$	$\mathbf{2003.30^{+0.03}_{-0.04}}$			
S55/S0-102:						
a ($''$)			$\mathbf{0.109^{+0.002}_{-0.002}}$			
e			$\mathbf{0.74^{+0.01}_{-0.01}}$			
i (°)			$\mathbf{141.7^{+1.6}_{-1.5}}$			
ω (°)			$\mathbf{133.5^{+3.9}_{-3.6}}$			
Ω (°)			$\mathbf{129.9^{+4.0}_{-4.2}}$			
T_p (yr)			$\mathbf{2009.31^{+0.03}_{-0.03}}$			

3 Relativistic Orbit of the Stars Near the Black Hole in the Galactic Center

3.1 Introduction

After the formulation of the theory of General Relativity (GR) by Einstein (1915), two points were recognized. First, a vacuum solution for a fully collapsed body is admitted by the theory and it can be derived in an analytical manner (Schwarzschild 1916). Second, three most promising observational tests can be done within the solar system and in the weak-field gravitational regime. The first test was the measurement of the bending of light passing nearby a massive body. The second proposed test was measuring the time delay of the light crossing through a strong gravitational field. The third test was measuring the anomalous perihelion shift of the orbit of Mercury.

A lasting debate followed regarding the interpretation of the experimental constraints on the perihelion shift of Mercury and whether the obtained results of the measurements supported or contradicted the prediction of GR. Confusion was sparked by the fact that the total value of the shift includes additional effects, such as the influence of quadrupole moment of the Sun. The latter was poorly constrained at that time but it was also realized that in principle these measurements could be refined if the other planets' perihelion shifts at different radii, are measured too.

In this thesis, I adopt the effect of the periapse shift as an acceptable and practical way to test the gravitational potential in the proximity of the supermassive black hole (SMBH) of the Galactic center (GC) using the stars in the S-cluster as test particles revolving around Sgr A*. I can approach this problem the same way as the case of the solar system planets in the framework of the weak-field post-Newtonian (PN) approximation, with the SMBH playing the role of the central body.

Similar to the historical case of Mercury, I have to deal with complications caused by the Nuclear Star Cluster (NSC) of the mass of up to $10^4\ M_\odot$ (e.g. the early result by Mouawad et al. 2005) that contributes to a Newtonian shift of the stellar orbits of the same order of magnitude in a direction opposite to the GR shift. This Newtonian precession can partially or fully neutralize the GR precession for a star with an orbit similar to the orbit of S2. The number of these perturbers (the granularity of the mass) can also cause a precession caused by a phenomena, called the "resonant relaxation" (RR) (Sabha et al. 2012). It affects primarily the orbital plane and eccentricity, but can have an effect on the other precessions, i.e. GR and Newtonian precession, from the additional mass. Merritt et al. (2010) has shown that for orbits larger than ~1 mpc, RR can cover the frame-dragging effect and for orbits larger than ~0.2 mpc it can cover the Lense-Thirring effect.

The PN effects can manifest themselves in the stellar redshift curves through the special relativistic transverse Doppler effect and gravitational redshift (Zucker et al.

2006; Angélil et al. 2010; Zhang et al. 2015). The deviation from the redshift curve is highly anticipated to be observable in 2018, when S2 is going through its next periapse passage. To be able to detect any PN effect, the accurate determination of the proper motion and the radial velocity of the star are essential.

The detection of the PN effects will be more optimistic if stars with smaller orbital scales, and consequently more relativistic, are detected within the orbit of S2. The Newtonian perturbations for such stars are also less dominating. Instruments like GRAVITY on the Very Large Telescope Interferometer (VLTI, e.g. Eisenhauer et al. 2011; Eckart et al. 2012; Grould et al. 2016) or future instruments like the European Extremely Large Telescope (E-ELT, e.g. Brandl et al. 2016; Davies et al. 2016) are aiming at observing these stars.

3.2 Near-Infrared Data

In this chapter, I use the results from the orbital analysis from the previous chapter. Moreover, I use the near-infrared (NIR) and spectroscopy data of S2 and S38 acquired with the NACO and SINFONI instruments on the European Southern Observatory (ESO) Very Large Telescope (VLT), respectively, which I analyze in Sect. 2.3.3. I aim to probe the observable relativistic effects in the orbit of S2 and several simulated stars within the orbit of S2 with different impact parameters. I also make use of these simulated stars to develop a practical method for estimating the strength of the weak-field PN effects, and then apply it to the NIR data of S2. In addition to the data acquired by the VLT, I used the positions and radial velocities published by Boehle et al. (2016) from 1995 to 2013, who use a different NIR data set acquired by the Keck observatory.

3.3 The Case of Simulated Stars

I use Equation 2.6 and different initial state vectors at the apoapse positions to get orbits with a wide range of periapse distances inside the orbit of S2. I integrate the equation of motion iteratively for one full orbit using the fourth-order Runge-Kutta method (see the Appendix, Sect. 5.4 for more details on the method). I generate 14 mildly to highly relativistic stellar orbits with their initial state vectors reported in Table 3.1. Since the eccentricity of the orbit is one of the two parameters that define the periapse distance and I intend to produce few orbits with similar eccentricities, I need to introduce a new parameter. This new parameter should enable me to have a control over the eccentricity of the orbits via the initial parameters. Therefore, I introduce the new parameter $\alpha \equiv r \times v^2$, which has a linear correlation with the eccentricity.

Accuracy in generating the orbits is vital. If the system loses energy over the time, it will result in stretching and the next apoapse will not result in the same value for the semimajor axis. Therefore, I have to make the time steps relatively small in spite of the larger computational time for generating a full orbit in order to keep the energy of the system conserved. Another advantage of a small orbital scale and therefore a small orbital period, is that the perturbation due to the proper motion of the central black hole in the NIR reference frame will be small and consequently can be neglected.

***Table 3.1**: Generated simulated stars using Equation 2.6. The initial state vectors are recorded in the second and third columns. The fit to the upper and lower part of the orbit are labeled by subscripts u and l, respectively. The calculated periapse precessions are recorded in the last column. The last line is designated to the results of my analysis for S2 using the data in this work and the published data by Boehle et al. (2016). The uncertainties are estimated by the Markov Chain Monte Carlo method explained in the appendix. Credit: Parsa et al. (2017).*

Star	ΔR.A. (mpc)	$(v_{Dec.}, v_z)$ (10^3km/s)	ϒ	a_u (mpc)	a_l (mpc)	e_u	e_l	$\Delta\omega$ (rad)
1	0.07	(5.34 , 0.00)	0.120	0.0252 ± 0.0004	0.0173 ± 0.0017	0.947 ± 0.005	0.823 ± 0.024	0.586 ± 0.029
2	0.5	(2.00 , 0.00)	0.015	0.2573 ± 0.0002	0.2386 ± 0.0039	0.909 ± 0.001	0.885 ± 0.003	0.070 ± 0.001
3	0.05	(7.75 , 0.00)	0.106	0.0210 ± 0.0003	0.0166 ± 0.0012	0.915 ± 0.007	0.789 ± 0.014	0.530 ± 0.014
4	0.06	(7.07 , 0.00)	0.087	0.0269 ± 0.0002	0.0209 ± 0.0013	0.907 ± 0.004	0.788 ± 0.012	0.434 ± 0.016
5	0.04	(10.00 , 0.00)	0.095	0.0185 ± 0.0002	0.0154 ± 0.0005	0.871 ± 0.004	0.735 ± 0.008	0.480 ± 0.012
6a	0.06	(6.45 , 5.00)	0.061	0.0300 ± 0.0006	0.0260 ± 0.0021	0.840 ± 0.005	0.741 ± 0.019	0.301 ± 0.023
6b	0.06	(8.16 , 0.00)	0.061	0.0300 ± 0.0002	0.0259 ± 0.0007	0.850 ± 0.002	0.748 ± 0.001	0.312 ± 0.008
7a	0.05	(8.00 , 6.00)	0.056	0.0262 ± 0.0003	0.0232 ± 0.0013	0.814 ± 0.008	0.705 ± 0.011	0.279 ± 0.020
7b	0.05	(10.00 , 0.00)	0.056	0.0262 ± 0.0001	0.0238 ± 0.0005	0.803 ± 0.003	0.702 ± 0.005	0.294 ± 0.006
8	0.07	(8.45 , 0.00)	0.039	0.0379 ± 0.0001	0.0355 ± 0.0008	0.786 ± 0.003	0.712 ± 0.008	0.200 ± 0.008
9	0.10	(7.07 , 0.00)	0.027	0.0554 ± 0.0002	0.0624 ± 0.0011	0.766 ± 0.002	0.716 ± 0.007	0.138 ± 0.006
10	0.05	(10.95 , 0.00)	0.044	0.0278 ± 0.0001	0.0258 ± 0.0004	0.731 ± 0.003	0.644 ± 0.005	0.232 ± 0.006
11a	0.06	(8.00 , 6.00)	0.037	0.0332 ± 0.0002	0.0299 ± 0.0021	0.755 ± 0.005	0.654 ± 0.003	0.163 ± 0.005
11b	0.06	(10.00 , 0.00)	0.037	0.0337 ± 0.0002	0.0317 ± 0.0006	0.724 ± 0.005	0.650 ± 0.007	0.194 ± 0.005
12	0.08	(9.35 , 0.00)	0.022	0.0479 ± 0.0004	0.0479 ± 0.0014	0.653 ± 0.004	0.630 ± 0.004	0.112 ± 0.012
13	0.09	(9.43 , 0.00)	0.017	0.0561 ± 0.0001	0.0553 ± 0.0003	0.589 ± 0.002	0.558 ± 0.003	0.086 ± 0.005
14	1.00	(3.00 , 0.00)	0.001	0.6597 ± 0.0001	0.6494 ± 0.0007	0.514 ± 0.001	0.501 ± 0.001	0.020 ± 0.006
S2	-	-	0.0007	4.6256 ± 0.0053	4.6140 ± 0.0317	0.892 ± 0.002	0.888 ± 0.003	0.002 ± 0.005

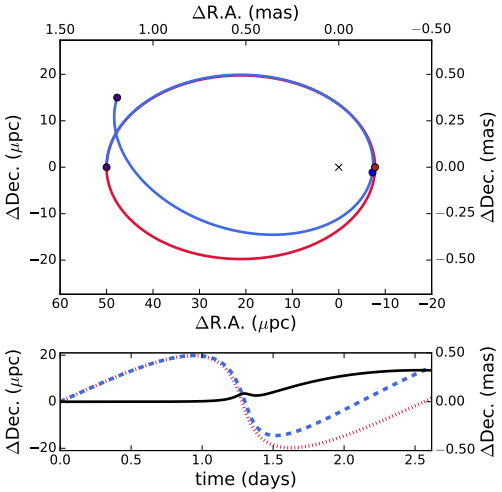

Figure 3.1: Post-Newtonian orbit alongside its Newtonian equivalent (case 7a of Table 3.1). ***Top panel:*** *post- / Newtonian orbit in blue/red and apoapses in purple and the periapse in blue/red.* ***Bottom panel:*** *ΔDec. of the post- /Newtonian orbit in blue/red against the time. The difference between the ΔDec. of the two orbits is shown with a black curve. The peak in this curve indicates the periapse. Credit: Parsa et al. (2017).*

In case of a binary system, the astrometric and radial velocity measurements can be perturbed. Additionally, the orbit of the primary can be severely changed, as a result of the binary disruption at the periapse. Hence, I have to mention here that I assume that all the S-stars are single stars and not part of a binary system. To support my assumption, at least for S2, there has not been any evidence that a secondary component exists in the spectra (Eisenhauer et al. 2005b; Martins et al. 2007, 2008).

In order to be able to compare orbits that are generated using the first-order PN approximation and the purely Newtonian ones, I demonstrate case 7a of Table 3.1 in Fig. 3.1. In this figure, the blue PN orbit is shown alongside its Newtonian counterpart; i.e. the red ellipse. I start both orbits from the apoapse until I reach the next apoapse (the purple points). Due to the periapse precession, the second apoapse of the PN orbit shifts. As can be seen the figure, most of the deviation occurs after the periapse. The periapses are marked with similar colors to the orbits. In this case, due to the orientation of the orbit, the difference between the two orbits is more noticeable in the declination direction, shown in the bottom panel against the time. The peak of the black line in this plot marks the periapse.

Nevertheless, plotting the right ascension or declination against the time does not allow the comparison of the positions with the same orbital phase. Plotting the positions against the mean anomaly facilitates a better comparison. The mean anomaly varies between $-\pi < M < \pi$ in one orbit with the periapse happening at the zero mean anomaly. Moreover, the periapses of the PN orbit and its Newtonian counterpart do not occur at the same time but at the same mean anomaly. This is demonstrated in Fig. 3.2. The post-/ Newtonian orbit is again shown with blue/red. The ΔR.A. and ΔDec. against the mean anomaly are plotted in the middle and bottom panels, respectively. The difference between the two orbits

$\delta = \sqrt{(\delta R.A.)^2 + (\delta Dec.)^2}$ is shown in a separate (top) panel.

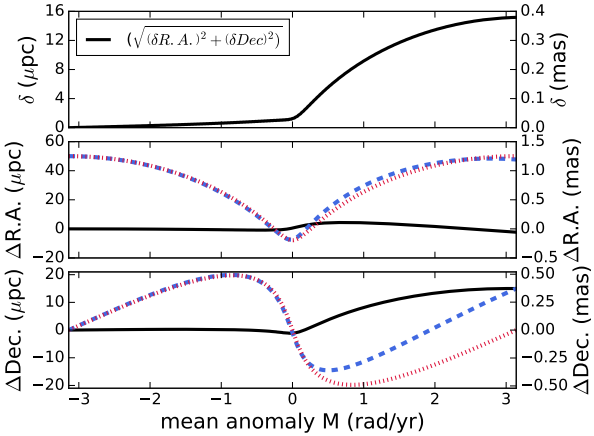

***Figure 3.2**: Comparison between the Newtonian and relativistic orbits (case 7a of Table 3.1) as a function of the orbital phase. The middle and bottom panels show the ΔR.A. and ΔDec. of the orbits demonstrated in Fig. 3.1 with respect to their mean anomaly in units of rad yr^{-1}. The zero mean anomaly (M) is the periapse and $-\pi$ and π are the first and second apoapses. The relativistic orbit is dashed blue and the Newtonian one is dotted red and the difference between the two in each panel is shown with a solid black line. The black solid line in the first panel shows $\delta = \sqrt{(\delta R.A.)^2 + (\delta Dec)^2}$, which is the distance between the positions of the two cases. Credit: Parsa et al. (2017).*

I choose the $r \simeq 0''.234$ as the upper limit of the generated stars, which is the apoapse of S2. Therefore, all the simulated orbits exist inside the orbit of S2 and thus they are more relativistic. It is useful to also compare the distribution of these stars to the distribution of the S-stars with determined orbits. The distributions are shown in Fig. 3.3 in the parameter-space, i.e., the semimajor axis against the eccentricity in the top panel and the semimajor axis against the periapse distance in the bottom panel. S2, S38, and S0-102/S55 are highlighted in the figure. As can be seen, the eccentricities of the simulated stars (blue circles) cover a similar range as the S-stars (red circles). However, the orbital scales are smaller than the known S-stars observed with today's instrumental power.

There is also a lower limit, since main-sequence stars cannot exist inside the tidal disruption radius near the black hole. As a result, the closest approach of the simulated stars cannot be smaller than the tidal disruption radius defined as

$$r_t \sim R_\star \, (M_{BH}/M_\star)^{(1/3)} \, . \tag{3.1}$$

This amounts to 85 μas for $M_\star = 1\ M_\odot$, $R_\star = 1\ R_\odot$, and $M_{BH} = 3.5 \times 10^6\ M_\odot$ (Alexander 2005). However, I find in the previous chapter $M_{BH} = 4.3 \times 10^6\ M_\odot$. This will result in $r_t \sim 90$ μas.

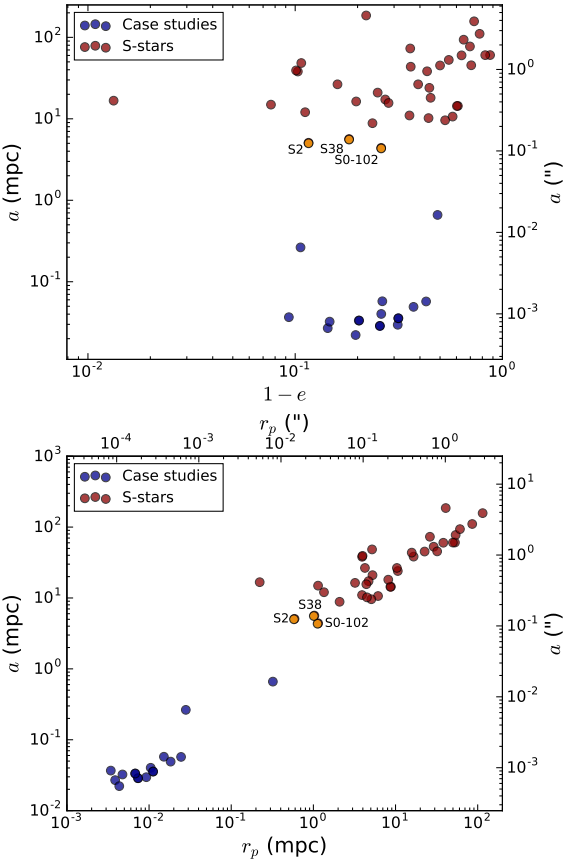

***Figure 3.3**: Distribution of the S-stars with determined orbits shown in red circles compared to the simulated stars listed in Table 3.1 and shown in blue circles. The semimajor axis against the eccentricity and the semimajor axis against the periapse distance are plotted in the top and bottom panels, respectively as parts of the parameter-space. Although the orbit of S111 is well determined, I did not include it in the S-stars since the orbit is hyperbolic and its eccentricity is greater than 1. S2, S38, and S55/S0-102 are highlighted with orange circles. Gillessen et al. (2017, Table 3) is the source of the orbital parameters of all S-stars with the exception of S2, S38, and S55/S0-102. The orbital parameters of these three stars are determined in the previous chapter of this thesis. Credit: Parsa et al. (2017).*

All the simulated orbits are generated on the sky plane, i.e., the velocity in the direction normal to the plane of the sky is zero. This could be done without loss of generality. However, for the sake of completeness, for three stars (6a, 7a, and 11a in Table 3.1) I also generated a counterpart star with $v_z \neq 0$. These three stars are 6b, 7b, and 11b and as a result of $v_z \neq 0$ the orbits have inclinations with respect to the plane of the sky. The information about the inclinations of these orbits comes from their radial velocities.

3.4 Method for Measurements of the Post-Newtonian Effects

After sampling the parameter-space with the simulated stars, I start with developing a method for the measurement of the PN effects. I develop the method in a way that the observation of only one orbital period is enough for each star. My main goal is to find a correlation between changes in some observable parameters and a theoretical PN parameter.

3.4.1 Squeezed States

First, I look for relatively uncomplicated measurable observables, which vary noticeably due to the PN effects after one orbital period. These observable parameters are more efficient if I can also exploit the uncertainties of the measurements in the orbital fitting simultaneously. This is why I use a concept similar to the squeezed states in quantum mechanics in the framework of orbital fitting.

A squeezed state can be defined as any state that satisfies the uncertainty principle given by

$$\alpha \times \beta \geq \epsilon \ . \tag{3.2}$$

In this framework we can replace α and β with $e^{-\chi_l^2}$ and $e^{-\chi_u^2}$, respectively. Where χ^2 is the statistical function describing the goodness of the fit to the orbit as the sum of the squared residuals between the model and the observational data. Therefore, $e^{-\chi^2}$ represents the likelihood that the model describes the orbit satisfactorily. Since the PN orbit is not symmetric, the asymmetry can be expressed by the difference in the orbital fitting to the different sections of the orbit. I use the upper (denoted by subscript u) and lower (denoted by subscript l) sections of the orbit. Therefore the inequality 3.2 can be written as

$$e^{-\chi_l^2} \times e^{-\chi_u^2} \geq e^{-\chi^2} \tag{3.3}$$

or equivalently

$$\chi_l^2 + \chi_u^2 \geq \chi^2. \tag{3.4}$$

The uncertainty in the orbital fitting originates from different sources. It is either from the uncertainty of the measurements (subscript r) or from the fact that the orbital shape is not purely elliptical (subscript s). The inequality 3.4 can be rewritten as

$$\chi_{l,s}^2 + \chi_{u,s}^2 + \chi_{l,r}^2 + \chi_{u,r}^2 \geq \chi_{ul,r}^2, \tag{3.5}$$

if the goodness of the whole orbit (all sections) considering only the random uncertainty of the measurements is $\chi_{ul,r}$. The inequality can become an equality if it includes the goodness of the fit to the whole orbit considering only the uncertainty due to the misfit of the elliptical shape $\chi^2_{ul,s}$ to the right side

$$\chi^2_{l,s} + \chi^2_{u,s} + \chi^2_{l,r} + \chi^2_{u,r} \sim \chi^2_{ul,s} + \chi^2_{ul,r}. \tag{3.6}$$

If I assume that the uncertainties of the measurements for the different sections of the orbit are similar $\chi^2_{u,r} \sim \chi^2_{l,r}$, then I can write

$$\chi^2_{ul,r} = \chi^2_{l,r} + \chi^2_{u,r} \sim 2 \times \chi^2_{l,r}. \tag{3.7}$$

I presume that in the fit to all orbital sections, the uncertainty due to the misfit to the shape of the orbit is distributed evenly throughout the orbit, which results in $\chi^2_{u,s} \sim \chi^2_{l,s}$. Thus, I can write

$$\chi^2_{ul,s} = \chi^2_{l,s} + \chi^2_{u,s} \sim 2 \times \chi^2_{l,s} \sim 2 \times \chi^2_{u,s}. \tag{3.8}$$

If the measurements are very accurate, the uncertainties due to the misfit are dominant. For example, the lower section of the orbit has a lower eccentricity and smaller semimajor axis compared to the upper half. As a result, fitting to one of these sections will "squeeze" the fitting uncertainty due to the misfit of the ellipse to the other half. Therefore, if I only fit the lower part of the orbit well, I find for the upper part of the orbit

$$if \quad \chi^2_{l,s} \longrightarrow 1 \quad then \quad \chi^2_{u,s} \longrightarrow \sim 2 \times \chi^2_{u,s} > 1, \tag{3.9}$$

and similarly, if I only fit the upper part of the orbit well, for the lower part of the orbit I get

$$if \quad \chi^2_{u,s} \longrightarrow 1 \quad then \quad \chi^2_{l,s} \longrightarrow \sim 2 \times \chi^2_{l,s} > 1. \tag{3.10}$$

Therefore, $\chi^2_{u,s}$ or $\chi^2_{l,s}$ or the ratios between these parameters can be the observable I was looking for. In Fig. 3.4, I choose the ratio $\chi^2_u/\chi^2_{u,\chi^2_l \to 1}$ as the observable parameter for the simulated stars in Table 3.1. As for the theoretical parameter to evaluate the strength of the PN effect, I choose the "relativistic parameter Υ" introduced in Sect. 1.3.1.

The relativistic parameter at periapse defined as $\Upsilon \equiv r_s/r_p$ with r_s being the Schwarzschild radius and r_p the periapse distance, is a valid parameter for assessing the approximate magnitude of the components of the Schwarzschild metric outside a single object in vacuum (Baker et al. 2015). This parameter is also useful for comparison of constraints on GR in different regimes of gravity (Alexander 2005; Zucker et al. 2006; Ghez et al. 2008). It is 2 times the Newtonian gravitational potential and has a reversed correlation with the periapse distance and a correlation with the periapse shift, which are all parameters with which the strength of the PN effects can be evaluated. In this work, since the r_s is the same for all stars orbiting the black hole, the inverse of periapse distance $1/r_p$ is basically being measured since I expect larger/smaller PN effects for smaller/larger r_p.

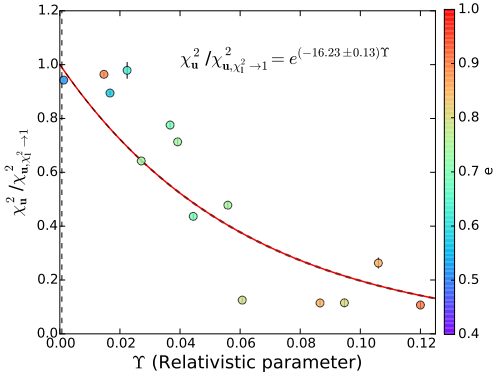

Figure 3.4: Correlation between the relativistic parameter ϒ and the ratio of the upper section's goodness of the fit to upper section's goodness of the fit after fitting to only the lower section $\chi^2_u/\chi^2_{u,\chi^2_l\to1}$ for the case studies in Table 3.1. Credit: Parsa et al. (2017).

If I assume $\chi^2_{u,s} \sim \chi^2_{l,s}$, then I expect to get $\chi^2_u/\chi^2_{u,\chi^2_l\to1} = 1/2$ from equation 3.9. For stronger PN effects, $\chi^2_{u,\chi^2_l} > 2\times\chi^2_{u,s}$ holds. The more the orbit approaches to a Newtonian one, the more the ratio approaches a unity, and the mismatch of the orbital fits to the two sections vanishes. The correlation in Fig. 3.4 can best be described as

$$\chi^2_u/\chi^2_{u,\chi^2_l\to1} = e^{(-16.23\pm0.13)\Upsilon}. \tag{3.11}$$

A simpler way to describe the differences in the orbital fits is using the changes in the orbital parameters, since fitting to different sections will result in different orbital elements. For an ellipse the eccentricity is defined as

$$e = \sqrt{1-\left(\frac{b}{a}\right)^2}. \tag{3.12}$$

Here e is the eccentricity and a is the semimajor and b is the semiminor axis. With a and e a unique ellipse can be defined in two dimensions. Therefore, the changes in the shape of a PN orbit in the two sections should result in changes in a and e. The different orbital parameters for the upper and lower section can be expressed in terms of these two ratios: a_l/a_u and e_l/e_u, which is much simpler and easier to understand compared to $\chi^2_u/\chi^2_{u,\chi^2_l\to1}$.

This method is illustrated in Fig. 3.5 for the case 7b from Table 3.1. Here two full orbits are plotted starting from an apoapse point. The blue circles are apoapse points and the purple points are periapse points in the upper left panel. In the upper right and bottom panel, the yellow circles are the observed data points. These points make a full orbit on the sky and are selected with equal time intervals between them in accordance to the orbital period. The orbital periods of the simulated stars range between an hour to a month. The elliptical fit to the upper section is solid red and the fit to the lower section is solid cyan in the bottom panel.

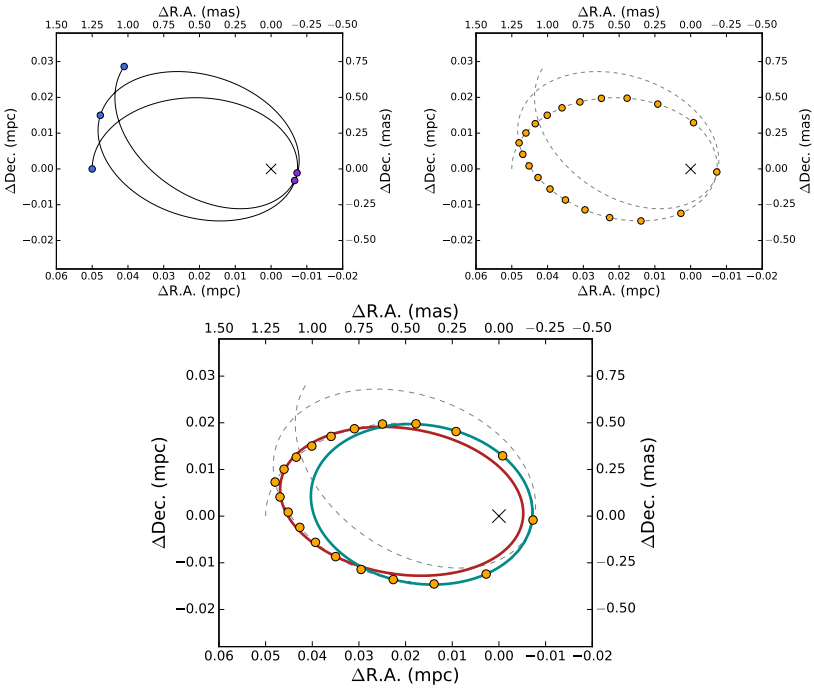

Figure 3.5*: Illustration of the method for measuring the PN effects using the changes in the semimajor axis and eccentricity. Two orbits and the location of the black hole (black cross) are shown on the sky plane in each panel. The blue circles are the apoapses and the purple circles are the periapses in the upper left panel. The yellow circles are the observations done in equal time intervals in the upper right and bottom panels. The higher velocity around the periapse passage results in the larger separations in the data points in the lower section of the orbit. In the bottom panel, the two elliptical fits of the upper and lower section are demonstrated with red and cyan ellipses, respectively. Credit: Parsa et al. (2017).*

The upper and lower fits are done for all stars in Table 3.1 and the semimajor axis and eccentricity are reported in columns five to eight. This is done via the minimum χ^2 method explained in the Appendix. For this method, an approximation for the uncertainty of the measurement for each of the assumed observational data points was needed. I assumed that the maximum amount of these uncertainties is allowed to be equal to the displacement of the positions due to the periapse shift, since for larger uncertainty in the measurement, the detection of the PN effects is impossible. Therefore, the value of the standard deviation of an approximate mean displacement of $a\Delta\omega/4$ for half of the data points on an orbit was attributed to all points as the uncertainty of the measurement. $\Delta\omega$ is the periapse precession.

For stars 6b, 7b, and 11b from Table 3.1, since the orbit is not located on the plane of the sky, few more steps have to be taken before the elliptical fits are done. A Keplerian orbit should be fitted to the assumed data points and their radial velocities to determine the inclination and the line of nodes. Then the inclination can be applied to each data point using the argument of periapse. Now all the assumed observed points have a z coordinate and I can move to the plane of the orbit for the elliptical fits. Nevertheless, these additional steps introduce more uncertainty to the final results and, consequently, I decided not to use these stars for the final analysis.

3.4.2 Periapse Shift

Another method to investigate the PN effects is a measurement of the changes in the argument of periapse $\Delta\omega$ presented by Angélil & Saha (2014). For the semimajor axis of $0''.126$, the eccentricity of 0.88, and the mass of the black hole of $4.15 \times 10^6\ M_\odot$ (estimated in the previous chapter of this thesis) for S2, the GR shift of the periapse in 2018 is $\sim 11'$. However, as Angélil & Saha (2014) mention, this shift does not happen gradually. The shift in the argument of periapse of the pre- and post-periapse sections of the orbit happens as a step at the periapse flyby. This method can equivalently be done by measuring the argument of periapse before and after the periapse and calculate the change.

Therefore, in order to measure the rapid change in the argument of periapse, only considering small sections before and after the periapse passage should be sufficient. Nevertheless, the orbital elements cannot be determined with the required precision in such small sections. The information about at least half of the orbit is essential for accurate estimations of the orbital elements to find the changes in them, when comparing the upper and lower or the pre- and post-periapse sections.

I apply this method on the simulated stars in Table 3.1. This is done by fitting ellipses to the pre- and post-periapse sections of each orbit using a minimum χ^2 method with the same measurement uncertainties as the previous method for each assumed data point. Like the previous method, I illustrate this on the star 7b in the upper panel of Fig. 3.6. In the lower panel, the instantaneous argument of periapse is plotted against the time for one orbital period. The instantaneous argument of periapse at each point on a PN orbit is the argument of periapse of the Newtonian equivalent of that orbit at that point. This parameter is not directly observable. The change in the argument of periapse of each star is reported in last column of Table 3.1.

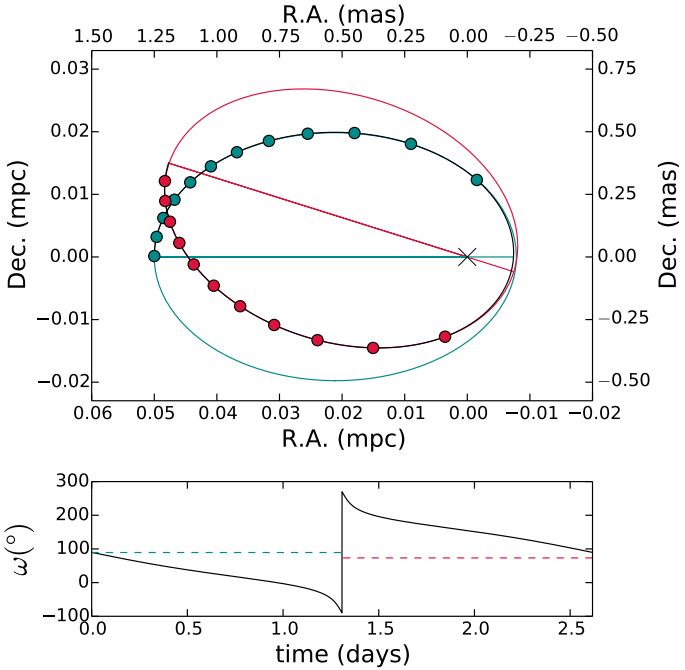

***Figure 3.6**: Method for the observation of the PN effects by means of measuring the changes in the argument of periapse for the star 7b from Table 3.1. **Top panel:** One full orbit in black with the pre-periapse data points in cyan and the post-periapse data points in red. The elliptical fit to each set of these data points is shown with the similar color. The angle between the major axes is the periapse shift. **Bottom panel:** Instantaneous argument of periapse against time in black. The argument of periapse determined from the pre-/ post-periapse section is shown with the cyan/red dashed line. Credit: Parsa et al. (2017).*

3.4.3 Comparison of Methods

On the one hand, when measuring the changes in the orbital elements, i.e. the semimajor axis and eccentricity, by evaluating the ratios a_l/a_u and e_l/e_u, the orbital changes in the radial direction are being measured, and the violated folding symmetry along the semiminor axis is being used. On the other hand, the change in the argument of periapse is violating the folding symmetry along the semimajor axis. One can consider this as squeezing the goodness of the fit to the sections of the orbit, before and after the periapse, following the formalism in the pervious section. This is visualized in Fig. 3.7.

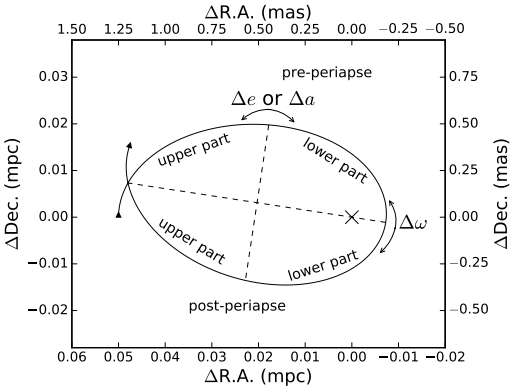

Figure 3.7: Comparison between the two methods discussed for the determination of the PN effects, using the changes in the orbital elements in different sections of the orbit, as described in Sect. 3.4.1. Credit: Parsa et al. (2017).

3.5 The case of S2

In this section, I implement the methods to the data of S2 to determine their outcome. I use the data set from 2002 to 2010 analyzed in the previous chapter. Additionally, since this data set does not cover a full orbit I use the data published by Boehle et al. (2016) from 1995 to 2010. However, since the two data sets are from two different telescopes with possibly different data analyzation methods, they do not share the same reference coordinate system. Gillessen et al. (2009a) assume that the only differences between the two data sets are the location of the origin and the zero velocity. I implement this approach for bringing the two data sets to the same reference coordinate system by adding four parameters to my fits: Δx, Δy, Δv_x, and Δv_y. Next I fit the new parameters, the gravitational potential parameters of the black hole, and the orbital parameter of S2 using the astrometric and radial velocity of S2, in order to bring the coordinate systems together, using the Markov Chain Monte Carlo (MCMC) method. The new parameters are

$$\Delta x = +2.95 \pm 0.25 \text{ (mas)} \tag{3.13}$$

$$\Delta y = -1.08 \pm 0.48 \text{ (mas)} \tag{3.14}$$

$$\Delta v_x = -0.21 \pm 0.04 \text{ (mas/yr)} \tag{3.15}$$

$$\Delta v_y = -0.44 \pm 0.09 \text{ (mas/yr)}. \tag{3.16}$$

The reference epoch is May 1995. The uncertainties are the result of the MCMC chains. I implement these parameters on the data from Boehle et al. (2016). Now the combined data set is covering all four sections of the orbit sufficiently for the implementation of the methods in Sects. 3.4.1 and 3.4.2 on S2. Since the orbit of S2 is not located on the plane of the sky, I have to include the additional steps explained earlier to add the third coordinate to the astrometric data and move to the orbital plane. The results of the fits to all the four sections are in the last row of Table 3.1.

Additionally, I compare the PN and the Newtonian fits to the two data sets from 1995 to 2015 in Fig. 3.8 with the dashed blue and dotted red curves. The black solid

line shows the difference between the two models and indicates that the difference is observable during and after the periapse passage in 2018.

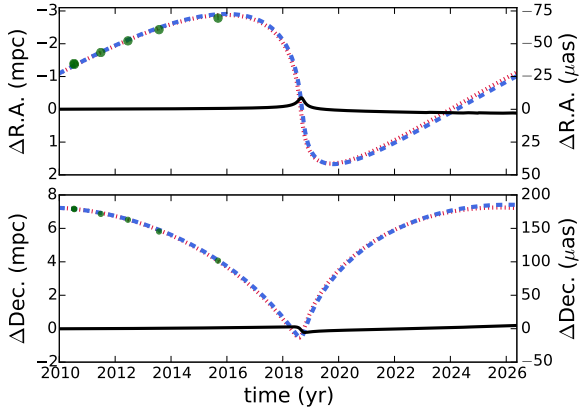

***Figure 3.8**: Comparison between the post-Newtonian (blue dashed curve) and Newtonian (red dotted curve) fits to the combined astrometric and the radial velocity data of S2 covering the years 1995 to 2015 in right ascension (ΔR.A., top panel) and declination (ΔDec., bottom panel). The horizontal axes in both panels are the orbital period. The data points are shown by green circles. The fits are extrapolated to cover the future periapse and apoapse. The peak and the step in the solid black line showing the difference between the two models in the top and bottom panels indicate the sudden shift of the argument of periapse during the Sgr A* flyby. Credit: Parsa et al. (2017).*

Gillessen et al. (2009a) presume that since the North direction in the GC is easy to determine, a rotation between the data sets is improbable. I follow their assumption in finding the new parameters to translate the data sets from different coordinate systems. However, here I add a fifth parameter for the possible rotation to determine a limit for it. The existence of such a rotation will have an unacceptable effect, when determining the argument of periapse of the peri- and post-periapse sections. Consequently, the determined periapse shift will be contaminated. Especially since the pre-periapse section is covered only by the Keck data set.

I perform the MCMC method again with the additional parameter for the rotation centered on the location of Sgr A*. I use a Newtonian model and include the S38 combined data set of the VLT and Keck (Boehle et al. 2016) from 2004 to 2013. The reason for including S38 in this fit is its especial orientation with respect to S2 on the plane of the sky, which helps in confining the possible rotation. Additionally, the expected periapse shift of S38 is small, ~6′ using the orbital elements determined in the previous chapter. The resulting upper limit for the rotation between the two data sets is 0′.002 for the S38 combined data (in the intersection of the two data sets) and 0′.1 for the S2 and S38 fit. As a result, I conclude that the upper limit for the possible rotation between the two data sets is very small compared to

the expected GR periapse shift of S2 (~11′) and can be neglected. Therefore, the combined data set is suitable for investigating the PN effects in the orbit of S2.

3.6 Results

3.6.1 The Simulated Stars

Other than the relativistic parameter at the periapse Υ, parameters that can act as measures of the strength of the PN effects are the periapse distance and the speed at the periapse in units of the speed of light $\beta = v_p/c$, where v_p is the velocity during the periapse passage. The relativistic parameter at the periapse is a function of the parameters of the orbital shape, i.e., the semimajor axis and eccentricity. Figure 3.9 shows the correlations $\Upsilon \propto a$ and $\Upsilon \propto (1-e)$. The correlation between Υ and the orbital period is similar to the correlation between Υ and the semimajor axis. The black lines in the top panel are from top to bottom e = 0.9, 0.8, 0.7, 0.6, and 0.5. While in the bottom panel, the black lines are a = 0.02, 0.03, 0.04, 0.05, 0.06, 0.27, 1, and 5 mpc or equivalently a = ~0.50, 0.75, 1.00, 1.25, 1.5, 6.7, 25, and 125 mas from top to bottom. The circles/diamonds show the simulated stars listed in Table 3.1 located on/inclined to the plane of the sky. The dashed lines in both panels indicate the Υ of S2 at its periapse, which is the minimum amount among the stars in Table 3.1.

In this chapter, my prime parameter to demonstrate the strength of the PN effects is the relativistic parameter at periapse. In Figs. 3.11, 3.12, and 3.13, I demonstrate $\Upsilon \propto a_l/a_u$, $\Upsilon \propto e_l/e_u$, and $\Upsilon \propto \Delta\omega$ obtained from the simulated stars in Table 3.1. The relativistic parameter at the periapse can alternatively be expressed as $\Upsilon = r_s/(a(1-e))$, which might result in complications in the correlations $\Upsilon \propto a_l/a_u$ and $\Upsilon \propto e_l/e_u$, i.e., parameterization of a and e might be required. However, the effect of the eccentricity is dominant only on small orbital scales. For larger orbital scales, the effect of the eccentricity is negligible. For a typical eccentricity range of between 0.4 – 0.9, Υ varies by a factor of 6. For the possible semimajor axis range, if the periapse distance ranges between the tidal disruption radius and the S2 periapse distance (~ 0.01 – 5 mpc), Υ changes by a factor of 500. But for the ratios a_l/a_u and e_l/e_u, the dependencies on the semimajor axis and eccentricity are compensated almost entirely and in Figs. 3.11 and 3.12 the scattering around the correlation is small.

The a_l/a_u and e_l/e_u ratios are smaller for stronger PN effects, i.e., larger Υ. This is a result of a larger semimajor axis and eccentricity for the upper section compared to the lower section. The ratios are expected to approach the unity with less and less PN effects, since the orbit is approaching to its Newtonian equivalent. The correlations between the ratios a_l/a_u and e_l/e_u and Υ can be best described as

$$a_l/a_u = (-3.14 \pm 0.18)\,\Upsilon^{(1.15\pm0.02)} + 1\,, \tag{3.17}$$

and

$$e_l/e_u = (-0.41 \pm 0.01)\,\Upsilon^{(0.44\pm0.01)} + 1\,. \tag{3.18}$$

Replacing the relativistic parameter with the periapse distance is not useful, since $r_p = r_s/\Upsilon$. Stronger PN effects result in smaller periapse passages and hence,

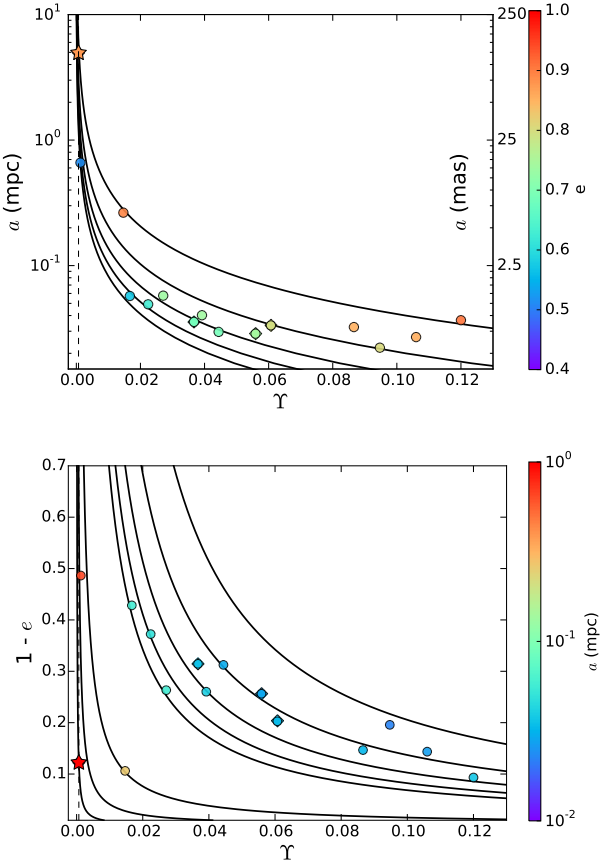

***Figure 3.9**: Correlations $\Upsilon \propto a$ and $\Upsilon \propto (1-e)$ in the top and bottom panels, respectively. Υ is the relativistic parameter at the periapse and a is the semimajor axis and e is the eccentricity. The solid lines in the top panel are $e = 0.9 - 0.5$ in steps of 0.1 (top to bottom). The solid lines in the bottom panel are $a = 0.02 - 0.06$, 0.27, 1, 5 mpc (~0.5 – 1.5, 6.7, 25, 125 mas, top to bottom). The circles/diamonds are the simulated stars from Table 3.1 without/with an inclination. S2 is represented with a star symbol. The dashed lines are $\Upsilon_{S2} = 0.00065$. The colorbars represent the eccentricity/semimajor axis in the top/bottom panel. Credit: Parsa et al. (2017).*

larger velocities at the periapse. Moreover, if the eccentricity is sufficiently large, therefore $r_p \ll a$ and $\Upsilon \ll 1$ as the orbit approaches to a Newtonian one. For this condition, the equation $\beta \sim \sqrt{\Upsilon}$ holds (Zucker et al. 2006). In this study and using the simulated stars, I find $\beta = (0.713 \pm 0.003)\sqrt{\Upsilon}$ (Fig. 3.10), which agrees with the result by Zucker et al. (2006). In Fig. 3.10, S2 is shown via a star symbol and the dashed vertical lines are the limits for the selection of the simulated stars, i.e., β_{S2} at the periapse, expected $\Upsilon_{S2} = 0.00065$, and Υ of a star with a periapse distance as large as the tidal disruption radius. The simulated stars from Table 3.1 are shown with circles (without inclinations) and diamonds (with inclinations).

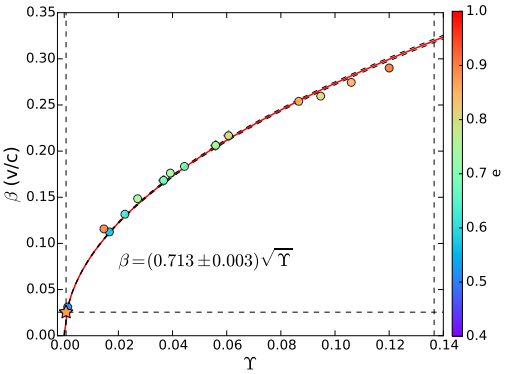

***Figure 3.10**: Correlation between Υ and the relativistic β at the periapse for the simulated stars in Table 3.1, where β is in units of the velocity of light. The circles/diamonds are the simulated stars from Table 3.1 without/with an inclination. The colorbars represent the eccentricity. S2 is shown via a star symbol and the dashed vertical lines are the limits for the selection of the simulated stars. The correlation is shown with the red line and its uncertainties are shown with gray dashed lines. Credit: Parsa et al. (2017).*

3.6.2 The S2 Star

The orbit of S2 gives us a unique chance to implement the result of this study due to its large eccentricity and high speed at the periapse passage. The last row of Table 3.1 contains the semimajor axis and eccentricity of the upper and lower sections of its pervious full orbit and the difference between the argument of periapse of the pre- and post-periapse sections. These values and their uncertainties are found as the mean and the standard deviations of the distribution of the parameters, using the MCMC method. Here, I intend to use a_l/a_u, e_l/e_u, and $\Delta\omega$ and their normal distributions to find Υ_{S2}. The derived distribution for a_l/a_u and e_l/e_u have an upper limit of 1. Therefore, I calculate their truncated normal distributions as the probability density functions (PDFs), using the following equation

$$f(x;\mu,\sigma,a,b) = \frac{(1/\sigma)\,\phi\left((x-\mu)/\sigma\right)}{\Phi\left((b-\mu)/\sigma\right) - \Phi\left((a-\mu)/\sigma\right)}. \tag{3.19}$$

Here $a \leq x \leq b$ and ϕ is the PDF of a standard normal distribution and Φ is the cumulative distribution function (CDF). In order to find the PDF of Υ from the PDF of a_l/a_u, e_l/e_u, or $\Delta\omega$, I use the correlations and a change of variables. For the correlation between the Υ and $\Delta\omega$ I use

$$\Delta\omega = \frac{6\pi G M_{BH}}{c^2 a\,(1-e^2)}\,, \tag{3.20}$$

which is the periapse shift due to a Schwarzschild black hole up to the first order. The PDFs are shown next to their axis in the bottoms panels of Figs. 3.11, 3.12, and 3.13. The means and the standard deviations are in solid and dashed black, respectively. The orange stars are the corresponding means of the distributions with the error bars showing the standard deviations in both axes. Since the distributions are truncated, I also calculate the medians and medians absolute deviations and show them with blue solid and dashed lines and the corresponding blue star with the median absolute deviations ("mads") as errorbars in both axis.

All calculated values are reported in the first and second rows of Table 3.2. Here, I assumed that the individual values obtained from each of the correlations respond in non-identical ways to the statistical and systematical uncertainties of the data. This means that any changes in parts of the data set will result in different variations for the semimajor axis, eccentricity, and periapse shift. Therefore, the uncertainties of a_l/a_u, e_l/e_u, and $\Delta\omega$ do not follow a Gaussian distribution, and as a result, the combination of the three values by means of median and "mad" is preferable. The values resulted from the correlations $\Upsilon_{S2} \propto a_l/a_u$ and $\Upsilon_{S2} \propto e_l/e_u$ are taken into account as one, using their mean value, since they both describe the folding symmetry along the semiminor axis.

The drift motion of Sgr A* can affect the result of this analysis adversely. Therefore, I removed the estimated proper motion of the black hole given in the fifth column of Table 2.6 from the combined data set of S2. The resulting Υ after removing the drift motion of the black hole is given in the third and fourth rows of Table 3.2. However, the effect of this drift motion on the found Υ_{S2} proved to be small.

3.7 Discussion

3.7.1 Comparison with the Literature

The methodology in this work is inductive: starting from the astrometric and radial velocity data of stars orbiting the black hole to show that the PN effects affect the orbit of S2. I used indirect parameters to compare the PN orbits with the Newtonian ones based on the data. A deductive methodology is adopted by Iorio (2017): a GR theory is used to deduce the orbital parameters of S2 as a function of time under the influence of the mass of Sgr A*. However, it can be shown that the methodologies are comparable and confirm the same predictions.

Iorio (2017) finds the time-series of the first-order PN precessions of the orbital parameters analytically and numerically. The author finds maximum shifts of $\Delta a = 30$ au, $\Delta e = 0.003$, and $\Delta\omega = 0.2^\circ$ for S2. If the orbital parameters found

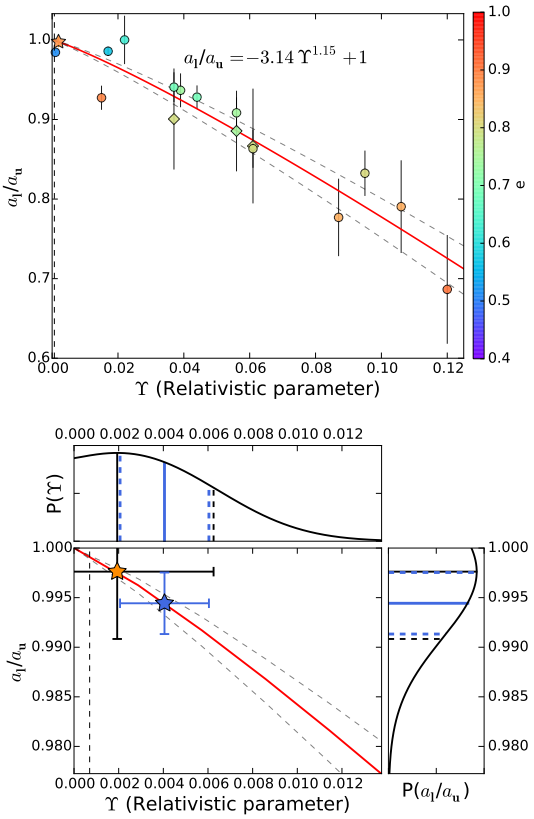

***Figure 3.11**: **Top panel:** Correlation between the relativistic parameter at periapse Υ and the ratio of the semimajor axis of the lower to upper sections of the orbit (a_l/a_u). S2 is shown via a star symbol and the dashed vertical line is the expected $\Upsilon_{S2} = 0.00065$. The circles/diamonds are the simulated stars from Table 3.1 without/with an inclination. The colorbars represent the eccentricity. The correlation is shown with the red line and its uncertainties are shown with gray dashed lines. **Bottom panel:** Zoomed-in top panel for better readability for S2. The truncated/calculated PDF of a_l/a_u/Υ is in the panel next to the y-axis/x-axis. The solid black/blue lines and the dashed black/blue lines are the mean/median and std/"mad", respectively, shown with the orange/blue stars with errorbars. Credit: Parsa et al. (2017).*

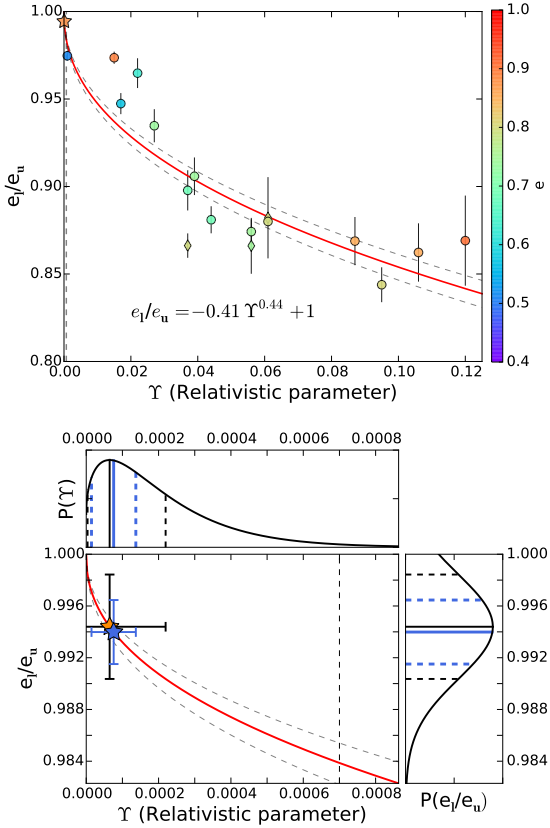

***Figure 3.12**: **Top panel:** Correlation between the relativistic parameter at the periapse Υ and the ratio of the eccentricity of the lower to upper sections of the orbit (e_l/e_u). S2 is shown via a star symbol and the dashed vertical line is the expected $\Upsilon_{S2} = 0.00065$. The circles/diamonds are the simulated stars from Table 3.1 without/with an inclination. The colorbars represent the eccentricity. The correlation is shown with the red line and its uncertainties are shown with gray dashed lines. **Bottom panel:** Zoomed-in top panel for better readability for S2. The truncated/calculated PDF of $e_l/e_u/\Upsilon$ is in the panel next to the y-axis/x-axis. The solid black/blue lines and the dashed black/blue lines are the mean/median and std/"mad", respectively, shown with the orange/blue stars with errorbars. Credit: Parsa et al. (2017).*

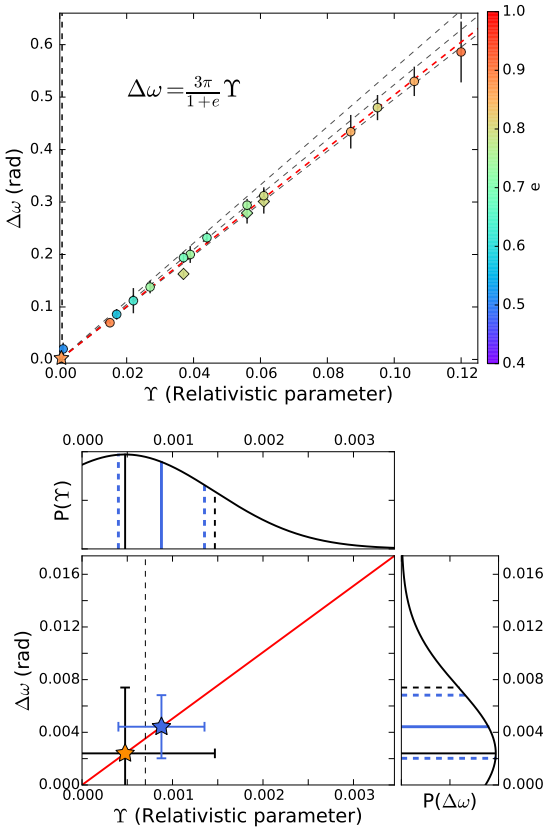

***Figure 3.13**: **Top panel:** Correlation between the relativistic parameter at periapse Υ and the periapse shift ($\Delta\omega$). S2 is shown via a star symbol and the dashed vertical line is the expected $\Upsilon_{S2} = 0.00065$. The circles/diamonds are the simulated stars from Table 3.1 without/with an inclination. The colorbars represent the eccentricity. The correlation for S2 ($e_{S2} \approx 0.87$) is the red dashed line and e = 0.7, 0.8, and 0.9 from top to bottom are the grey dashed lines. **Bottom panel:** Zoomed-in top panel for better readability for S2. The truncated/calculated PDF of $\Delta\omega/\Upsilon$ is in the panel next to the y-axis/x-axis. The solid black/blue lines and the dashed black/blue lines are the mean/median and std/"mad", respectively, shown with the orange/blue stars with errorbars. Credit: Parsa et al. (2017).*

***Table 3.2**: Relativistic parameter at the periapse (ϒ) of S2, calculated from the a_l/a_u, e_l/e_u and $\Delta\omega$ correlations. The first and second rows are calculated before removing the drift motion of Sgr A* from the data, and the third and fourth rows after. Each individual ϒ from each correlation is given as both mean (with std) and median (with "mad"). The final results in the last two columns are the combination of the individual values from a_l/a_u, e_l/e_u, and $\Delta\omega$ correlations in two different ways, i.e. the mean and the std of the three means or medians values and the median of the medians. Credit: Parsa et al. (2017).*

Method	a_l/a_u	e_l/e_u	$\Delta\omega$	Mean	Median
with the drift motion of BH:					
ϒ (Mean)	0.00193 ± 0.00432	0.00006 ± 0.00015	0.00048 ± 0.00099	0.00074 ± 0.00227	–
ϒ (Median)	0.00405 ± 0.00199	0.00008 ± 0.00006	0.00088 ± 0.00048	**0.00147 ± 0.00105**	**0.00088 ± 0.00080**
without the drift motion of BH:					
ϒ (Mean)	0.00179 ± 0.00424	0.00001 ± 0.00005	0.00048 ± 0.00099	0.00069 ± 0.00223	–
ϒ (Median)	0.00392 ± 0.00194	0.00002 ± 0.00002	0.00088 ± 0.00048	0.00142 ± 0.00102	0.00088 ± 0.00086

in this work are taken, i.e., a semimajor axis of $a = 0''.126$ and an eccentricity of $e = 0.884$, and these maximum shifts for them are applied, one can find

$$\frac{a_l}{a_u} = \frac{a - \Delta a}{a} = 0.971, \tag{3.21}$$

and

$$\frac{e_l}{e_u} = \frac{e - \Delta e}{e} = 0.997. \tag{3.22}$$

which are in agreement with the values that can be derived from Table 3.1.

3.7.2 Justifying the Result

Here, I exclude the possibility of the domination of noise, the proper motion of the black hole, and the rotation between the VLT and Keck data sets in the results.

In order to exclude the domination of noise, I assume that the orbital determination is entirely dominated by noise and therefore, the changes in the orbital parameters are influenced by noise as well. I consider for simplicity that the displacement of each section of the orbit due to noise is a single degree of freedom. If the orbital sections are considered similar to the methods above, i.e. upper and lower, and pre- and post-periapse, there are four sections that can be displaced along the semimajor or semiminor axes. However, only a fraction of the noise realizations is significant enough to result in a displacement of an orbital section. Now, I try to estimate a basic lower limit for the probability of getting a consistent result, assuming independent contributions of noise for each section.

There is a total of $4^4 = 256$ possibilities to combine the displacements of the four sections of the orbit and only one of them results in a unique arrangement with the measured a_l/a_u, e_l/e_u and $\Delta\omega$. Which means that the probability of reproducing the measurements is $1/256 \simeq 0.004$ or 0.4%. There are five possible combinations that gives a consistent result with the measurements if at least one of the quadrants is displaced. If more that one quadrant is displaced, it results in an inconsistent value for at least one of the measured orbital changes. Therefore, the total probability is $5/256 \simeq 0.019$ or ~2%. It can be concluded from these calculations, that it is very unlikely that the results from the measurements of orbital changes are dominated completely by noise.

The proper motion of Sgr A* in the NIR reference frame could dominate the variations of the orbital elements, especially the argument of periapse due to the east-west drift. A proper motion of the order of 30 μas yr^{-1} could result in the observed $\Delta\omega$. However, I attempted to remove this possibility by correcting the astrometric positions for the residual drift motion of Sgr A* before deriving the orbital parameters and their changes (see Table 3.2). Therefore, I conclude that there is only a very small probability that the measured $\Delta\omega$ is dominated by the proper motion of the black hole.

I also exclude the possibility that the measured quantities are dominated by the rotation between the different data sets that I used. First of all, the two data sets are compared to the radio reference frame. The temporal rotation of the IR reference frame relative to the radio frame is ~7.0 μas yr^{-1} arcsec^{-1} (Plewa et al. 2015), which

is less than 0′.5 in 20 yrs. This is 24 times smaller than the expected periapse shift of S2. Moreover, the uncertainty of the camera calibration for the rotation is less than ∼0°.1 which is less that ∼6′. This is almost a factor of two smaller than the expected first-order periapse precession of 11" for S2 for a semimajor axis of 0″.126, an eccentricity of 0.88, and a black hole mass of $4.15 \times 10^6\ M_\odot$. Furthermore, an upper limit of 0′.1 for the possible rotation of the two data sets is found in Sect.3.5, which is 110 times smaller that the expected periapse shift of S2. As a result, I conclude, that it is very unlikely that the measured $\Delta\omega$ in this work is a result of the rotation in the data sets.

3.7.3 Detectability of the PN effects

The direct measurement of the deviation of the orbit of S2 from a Newtonian one is not trivial, since the velocity at the periapse is high and distinguishing the IR counterpart of Sgr A* from the source is not easy. The correlations between the relativistic parameter and the observables ($\Upsilon \propto a_l/a_u$ and $\Upsilon \propto e_l/e_u$) are indirect methods, which are using the information from the whole orbital period to estimate the PN effects and consequently, predict parameters such as r_p, β_p, and $\Delta\omega$. These parameters are not directly measurable and a full knowledge of the orbit is essential in estimating them. For the case of S2, these correlations result in two distributions for Υ of S2.

The instantaneous argument of the periapse is not an observable parameter. Therefore, in order to measure the shift of the periapse, one cannot simply measure ω before and after the periapse passage. Therefore, $\Delta\omega$ should be measured over a complete orbital period (Angélil & Saha 2014). In this study, I measured the change in ω of S2 by using the orbital data from the two halves of the orbit before and after the periapse. The correlation between Υ and $\Delta\omega$ results in yet another distribution for Υ.

The median and "mad" of all three distributions of Υ for S2 is 0.00088 ± 0.00080. Another option in combining the three distributions is taking the average of the medians of the Υ distributions of the methods, using the same symmetry in the orbit, i.e., a_l/a_u and e_l/e_u methods, and considering them as one method. Next, the mean of this new distribution and the one from $\Delta\omega$ method should be calculated, which results in $\Upsilon = 0.00147 \pm 0.00105$. For both approaches in combining the distributions, the resulting value is consistent with the expected $\Upsilon_S 2 = 0.00065$ (for a semimajor axis of 0″.126, an eccentricity of 0.88, and a black hole mass of $4.15 \times 10^6\ M_\odot$) within the uncertainties. From the values in Table 3.2, it can be concluded that the proper motion of Sgr A* does not affect the result of these methods significantly. However, a significant limitation is originated from the data sets. The data from the pre-periapse and the lower sections of the orbit of S2 are sparser and less certain compared to the rest of the data. This limitation can be resolved after the next apoapse of S2 in 2026.

Additionally, if the expected Υ of S2 is considered, using the correlation between Υ and the relativistic β found in Sect. 3.6.1, the relativistic $\beta_{S2} = 0.00182 \pm 0.00008$ is found. If the Υ found in this work for S2 is used, I find $\beta_{S2} = 0.00187 \pm 0.0303$. Both values agree with ∼0.02, calculated from the simulations of the orbit of S2.

4 Summary and Conclusion

The achieved results of this thesis on the course of studying the effects of general relativity on the motion of the stars orbiting Sgr A*, the supermassive black hole in the Galactic center, can be divided into two main parts.

In the first part, the gravitational potential parameters of Sgr A* are estimated precisely. I find the mass of the black hole and our distance to it to be $M_{BH} = (4.15 \pm 0.13) \times 10^6 M_\odot$ and $R_0 = 8.19 \pm 0.11$ kpc based on Newtonian models for the orbits of stars that are in agreement with the recently published values.

Furthermore, I attempt to reduce the uncertainties in the calculation of the gravitational potential parameters of the black hole and the orbital parameters of the stars, especially the velocity of Sgr A*, by means of including multiple stars in the orbital fitting. Additionally, I apply a post-Newtonian model for stars, since using a Newtonian model instead of a relativistic one might result in the underestimation of R_0 (Zucker et al. 2006).

However, systematic errors of M_{BH} and R_0 arise as a result of the chosen model over a relativistic one (Gillessen et al. 2017). The differences in these parameters between the values derived from the Newtonian and post-Newtonian models are 0.57×10^6 $M_\odot$ and 0.34 kpc, respectively. Although some of the errors in the construction of the reference frame are taken into the account, I expect the unaccounted errors to be small in comparison to the values above. However, Boehle et al. (2016) have estimated 0.04×10^6 $M_\odot$ and 0.04 kpc for the uncertainties of the reference frame. I considered some of the errors by including the standard deviation of the mean of the residuals of the five reference stars in the astrometric errors of S2, S38, and S0-102/S55.

- Hence, I conclude as the first result of my analysis, that the systematic errors are dominated by the model variations and my final best estimates of the mass of the black hole and the distance to the Galactic center are $M_{BH} = (4.15 \pm 0.13 \pm 0.57) \times 10^6$ $M_\odot$ and $R_0 = 8.19 \pm 0.11 \pm 0.34$ kpc, respectively.

In the second part, I use the first-order post-Newtonian approximation to generate several orbits with a broad range of impact parameters. Next, I present two methods that utilize the changes in the orbital parameters for measuring the relativistic parameter at the closest approach to Sgr A*. The results from applying these methods, determined for the simulated orbits, are then carried out on the orbital analysis of S2. Consequently, I was able to determine a consistent change in the orbital parameters of S2 from the variations between the orbital fits to the upper/lower and the pre-/post-periapse sections of the orbit.

- For the changes in the argument of periapse, I find $\Delta\omega = 14' \pm 7'$. The obtained periapse shift is consistent with $\sim 11'$, calculated from the results of the orbital analysis of S2, where I found a semimajor axis of $0''.126$, an eccentricity of 0.88, and a black hole mass of $4.15 \times 10^6\ M_\odot$.
- These analyses imply a relativistic parameter of $\Upsilon = 0.00088 \pm 0.00080$ for S2, which is consistent with the expected theoretical value of $\Upsilon = 0.00065$ within the uncertainties.
- Since the eccentricity of S2 is the largest among the three stars with the shortest orbital period, it is currently the first and only star for which a relativistic parameter is determined.
- This is a new way to prove and determine the post-Newtonian characteristics of the orbit of S2.
- This is the first time that a measurement of the strength of the general relativistic effects has been achieved for stars orbiting a SMBH.

However, I have to discuss the effect of the resonant relaxation in the S-cluster near Sgr A* (Rauch & Tremaine 1996; Alexander 2005; Hopman & Alexander 2006; Merritt et al. 2010; Kocsis & Tremaine 2011; Sabha et al. 2012) on my result. The effect of the orbital torques on the orbit of S2 through the resonant relaxation is investigated in Sabha et al. (2012). The authors find that in the presence of a significant population of ten-solar-mass black holes, i.e., an enclosed mass of $10^3\ M_\odot$ to $10^5\ M_\odot$ (Mouawad et al. 2005; Freitag et al. 2006), the effect for each single orbit can be of the same order of magnitude as the relativistic (or Newtonian) periapse shifts. More on this discussion can be found in Parsa et al. (2017).

- Considering the obtained relativistic parameter of Υ implies that, at least over the orbital time scale of the resonant relaxation of S2, the proper motion of Sgr A* inside the stellar cluster and the effect of an extended mass inside the orbit of S2 are irrelevant within the current measurement uncertainties.

It is arguable that the calculated variations in the orbital parameters of S2 are random results or dominated by the disturbing effects discussed by Sabha et al. (2012). However, all these effects have compensated each other such that the direction and magnitude of the relativistic parameter is obtained within the 1σ uncertainties of the theoretically predicted value.

In future, continued single dish or interferometry studies of the stellar orbits close to Sgr A* must be performed in order to determine the relativistic motion of other stars.

5 Appendix

5.1 Justification of Control Method

In the following we justify and outline the procedure in one-dimensional coordinates. We call $\sigma_\star$ the statistical uncertainties with which the positions of the stars are extracted from the infrared images over all stars and epochs and σ_{SgrA*} the statistical uncertainties with which the position of Sgr A* can be extracted from the infrared images over all epochs.

In the infrared we relate all positions with respect to an average position of all 5 reference stars and Sgr A* that we consider in this formalism. It is required that the initial centering with respect to a position p_{IR} of all IR images is sufficiently accurate to derive the proper motions of the stars. For a single epoch the image centering offset δ_{center} goes into all positions relative to p_{IR} in this particular epoch. Any motion of stars and Sgr A* can then be expressed via an offset $off_\star$ from the reference position p_{IR} as

$$p_\star = p_{IR} + off_\star. \tag{5.1}$$

Deriving the proper motion position of Sgr A* and each individual star for each epoch, we can write:

$$p_{SgrA*} = p_{IR} + off_{SgrA*} + \sigma_{SgrA*} + \delta_{center} + A \tag{5.2}$$

and

$$p_\star = p_{IR} + off_\star + \sigma_\star + \delta_{center} + A \tag{5.3}$$

Here A includes other statistical or systematic contributions. For our method this would be possibly distortions that are locally so small that they can be neglected.

For the average position of all 5 reference stars we then find per epoch:

$$p_{\star,ave} = p_{IR} + average(off_\star) + \frac{1}{\sqrt{5}}(\sigma_\star) + \delta_{center} \tag{5.4}$$

By fitting an average motion to the average position of all stars over all epochs we effectively remove all constants and offsets but we have to consider σ_{SgrA*} and δ_{center} remains for each individual epoch. We can then write down the following correction term for single stars including Sgr A* for individual epochs:

$$p_{correction} = \frac{1}{\sqrt{5}}(\sigma_\star + \sigma_{SgrA*}) + \delta_{center} \tag{5.5}$$

Now we correct the motion of an individual star by subtraction the correction:

$$\begin{aligned} p_{\star corrected} &= p_{starIR} - p_{correction} \\ &= p_{IR} + off_{\star} + \sigma_{\star} - off_{SgrA*} + \delta_{center} \\ &\quad + \frac{1}{\sqrt{5}}(\sigma_{\star} + \sigma_{SgrA*}) - \delta_{center} \\ &= p_{IR} + off_{\star} + \sigma_{\star} - off_{SgrA*} \\ &\quad + \frac{1}{\sqrt{5}}(\sigma_{\star} + \sigma_{SgrA*}) \end{aligned} \tag{5.6}$$

Here, we find of course that for the stars off_{SgrA*} and $\frac{1}{\sqrt{5}}(\sigma_{\star} + \sigma_{SgrA*})$ are very small with respect to $off_{\star}$ and $\sigma_{\star}$ and therefore can be neglected. Hence we find

$$p_{\star corrected} = p_{IR} + off_{\star} + \sigma_{\star}. \tag{5.7}$$

However, we can now correct the motion for Sgr A* by subtraction of the correction:

$$\begin{aligned} p_{SgrA*corrected} &= p_{SgrA*} + p_{correction} \\ &= p_{IR} + off_{SgrA*} + \sigma_{SgrA*} + \delta_{center} \\ &\quad + \frac{1}{\sqrt{5}}(\sigma_{\star} + \sigma_{SgrA*}) - \delta_{center} \\ &= p_{IR} + off_{SgrA*} + \sigma_{SgrA*} + \frac{1}{\sqrt{5}}(\sigma_{\star} + \sigma_{SgrA*}) \end{aligned} \tag{5.8}$$

Again $\frac{1}{\sqrt{5}}(\sigma_{\star} + \sigma_{SgrA*})$ is small with respect to off_{SgrA*} and σ_{SgrA*} and we find

$$p_{SgrA*corrected}s = p_{SgrA*} + p_{correction} = p_{IR} + off_{SgrA*} + \sigma_{SgrA*}. \tag{5.9}$$

Hence, what we get as a result from the corrected positions $p_{SgrA*corrected}$ and $p_{\star,corrected}$ as a function of time is a combinations of the proper motions of Sgr A* and the stars and a possible drift velocity of the p_{IR} centering position. Connecting the NIR and radio reference frame as described in section 2.3.2, we could put a limit of 0.1 mas yr^{-1} to this drift.

5.2 Minimun χ^2 Estimation

In statistics, minimum χ^2 (chi-square) is a method of estimating the unobserved quantities based on the observed data. The χ^2 describes the goodness-of-fit of the data to the model. If the observed data point is shown with O_i and its measurement error is shown by σ_i, and the expected value from the model is E_i, then χ^2 for n observations is given by

$$\chi^2 = \sum_{i=1}^{n} \left(\frac{O_i - E_i}{\sigma_i} \right)^2. \tag{5.10}$$

The χ^2 has to be minimized. The best estimation of the model is the minimum $\chi^2 = 1$. The χ^2 should be equal or larger than 1. If it is smaller than 1, then the measurement errors are underestimated and they should be scaled such that the minimum $\chi^2 = 1$.

5.3 Bootstrap

The bootstap method was first introduced by Efron (1982). In general bootstrapping in statistics is any test performing with random resampling with replacement. The goal is to obtain a measure of accuracy like variance, confidence intervals, or other similar measurements for sample estimates. The resampling can be simply done with a Monte Carlo technique. It is performed by constructing a number of resamples with replacements of the original dataset with the size of the original dataset. It should be considered that the number of the repetitions is sufficiently large and for each resample (bootstrap sample) the mean (or any other statistic) is computed, which provides an estimate of the distribution of the mean. Bootstrap is simple and convenient when there is not any analytical form to estimate the distribution of the statistics.

5.4 Runge-Kutta Method

The Runge–Kutta methods are a family of iterative methods in numerical analysis, including the famous Euler Method, used for finding the approximate solutions of the ordinary differential equations. German mathematicians C. Runge and M. W. Kutta developed these methods in 1900. The most widely used Runge-Kutta method is "RK4", i.e, the fourth-order Runge-Kutta method.

If the initial value problem is defined as

$$\dot{y} = f(t,\ y)\ , \qquad y(t_0) = y_0\ . \tag{5.11}$$

Then, with the chosen step size h, one can write

$$y_{n+1} = y_n + \frac{h}{2}(k_1 + 2k_2 + 2k_3 + k_4)\ , \qquad t_{n+1} = t_n + h\ . \tag{5.12}$$

For each iteration these values have to be calculated:

$$k_1 = f(t_n,\ y_n)\ , \tag{5.13}$$

$$k_2 = f\left(t_n + \frac{h}{2},\ y_n + \frac{h}{2}k_1\right)\ , \tag{5.14}$$

$$k_3 = f\left(t_n + \frac{h}{2},\ y_n + \frac{h}{2}k_2\right)\ , \tag{5.15}$$

$$k_4 = f(t_n + h,\ y_n + k_3)\ . \tag{5.16}$$

The total accumulated error is of the order of 10^4. It is possible to solve a second-order differential equation using the Runge-Kutta method by treating it as two first-order differential equations.

$$\frac{d\dot{y}}{dt} = \dot{z} = g(t,\ y,\ z)\ , \qquad \dot{y} = z = f(t,\ y,\ z) \tag{5.17}$$

These two first order equations have to be solve together like the following.

$$y_{n+1} = y_n + \frac{h}{2}(k_1 + 2k_2 + 2k_3 + k_4)\ , \tag{5.18}$$

$$z_{n+1} = z_n + \frac{h}{2}(l_1 + 2l_2 + 2l_3 + l_4)\ , \tag{5.19}$$

with k_1, k_2, k_3, and k_4 defined as

$$k_1 = f(t_n,\ y_n,\ z_n)\ , \tag{5.20}$$

$$k_2 = f(t_n + \frac{h}{2},\ y_n + \frac{1}{2}k_1,\ z_n + \frac{1}{2}l_1)\ , \tag{5.21}$$

$$k_3 = f(t_n + \frac{h}{2},\ y_n + \frac{1}{2}k_2,\ z_n + \frac{1}{2}l_2)\ , \tag{5.22}$$

$$k_4 = f(t_n + h,\ y_n + k_3,\ z_n + l_3)\ , \tag{5.23}$$

and l_1, l_2, l_3, and l_4 defined as

$$l_1 = g(t_n,\ y_n,\ z_n)\ , \tag{5.24}$$

$$l_2 = g(t_n + \frac{h}{2},\ y_n + \frac{1}{2}k_1,\ z_n + \frac{1}{2}l_1)\ , \tag{5.25}$$

$$l_3 = g(t_n + \frac{h}{2},\ y_n + \frac{1}{2}k_2,\ z_n + \frac{1}{2}l_2)\ , \tag{5.26}$$

$$l_4 = g(t_n + h,\ y_n + k_3,\ z_n + l_3)\ . \tag{5.27}$$

5.5 Markov Chain Monte Carlo

The scientific research has been altered since the introduction of the probabilistic data analysis, and specially the Bayesian inference and the numerical methods for approximate inference, such as the Markov Chain Monte Carlo (MCMC) method. The MCMC was first introduced by Metropolis et al. (1953) in the context of solving problems in the statistical mechanics more than sixty years ago. However, its immense growth in popularity over the last decade is a result of the improvement in the computational power. The Markov Chain Monte Carlo techniques are a class of algorithms for sampling from a probability distribution based on constructing a

Markov chain that has the required distribution as its equilibrium distribution. The sample of the desired distribution is the state of the chain after a number of steps. The number of steps in the MCMC improves the quality of the sample; therefore, a larger number of steps is favourable. The name Monte Carlo was invented by Metropolis & Ulam (1949), who introduced a stochastic method using random numbers to derive the Markov process and to solve problems in the mathematical physics with large number of dimensions, in analogy to the Monte Carlo integration technique. However, the method did not fully develop until 1970, when it was used for sampling an arbitrary PDF by (Hastings 1970). He derived a condition for the acceptance ratio that a chain should satisfy in order to sample the target distribution. This simplest MCMC algorithm is known as the Metropolis-Hastings algorithm (Algorithm 1). Yet it was not until 2002 that the MCMC became known in astronomy. For the MCMC computations in this thesis, I used a python package called "emcee", which is widely being used in astronomy.

In order to understand how the MCMC works, a few concepts should be explained. The probability of the parameter θ given the evidence X is called the "posterior probability" $p(\theta|X)$. The Markov Chain Monte Carlo aims at an efficient sample from the posterior PDF. The "likelihood function" $p(X|\theta)$ is the probability of the evidence X given the parameter θ. The posterior probability and the likelihood function are related by the "priors". The priors show the current information about the desired parameters. When facing a large number of dimensions, it is expectable to have degeneracies among the parameters. The priors help to restrict the posterior to a smaller region of the parameter space. There are two types of priors: uninformative and informative. The uninformative priors have little restrictions on the parameters, while the informative ones are very restricting. The informative priors might come from previous analysis of some other data. When the data itself is not informative enough, the informative priors become very important, since they help in constraining the parameters. The posterior probability can be written as:

$$Posterior probability \propto Likelihood \times Prior probability, \tag{5.28}$$

or

$$p(\theta|X) = \frac{p(X|\theta)\ p(\theta)}{p(X)}\ . \tag{5.29}$$

The Gaussian likelihood function is given by

$$ln\ p(y|\mu, \sigma^2) = \sum_n \left[\left(\frac{y_n - \mu}{\sigma} \right)^2 + ln(2\pi\sigma^2) \right]. \tag{5.30}$$

Where μ is the model.

A "Markov chain" is a Markov process, i.e, a stochastic process that satisfies the Markov property, i.e., the process is memoryless. Therefore, a Markov chain is a sequence of random variables with the condition that the state X_{n+1} in future depends only on the state X_n in present and not on the state X_{n-1} in the past. In another words, given the present state, the future and past states are independent. The state space can be either continuous or discrete. If the probability of the

transition $K(x, y)$ from $X_n = x$ to $X_{n+1} = y$ is independent of n, then the chain is time-homogeneous. A time-homogeneous Markov chain has a stationary distribution π if

$$\pi(y) = \int dx\, \pi(x)\, K(x, y)\ . \tag{5.31}$$

An irreducible Markov chain is a chain that can go from any state to another in a finite number of steps. A chain is positive recurrent when it is an irreducible chain and has a stationary distribution, which means that the stationary distribution is unique. An aperiodic distribution is limiting (equilibrium distribution), when the chain is positive recurrent. In other words, starting from any initial distribution and applying the transition operator K many times, the stationary distribution π will be reached. The expectation value of a function $g(x)$ over π, approaches the average taken over the output of a Markov chain, if it is positive recurrent, i.e, it is irreducible with a unique stationary distribution π,

$$E_\pi[g(x)] = \int g(x)\, \pi(x)\, dx = \lim_{n\to\infty} \frac{1}{n} \sum_{i=1}^{n} g(x_i)\ . \tag{5.32}$$

This equation allows making estimates of a desired parameter from a Markov chain. The techniques to do so are called the MCMC. A chain with a stationary distribution is reversible, if it looks the same running forward and backward, starting from a stationary distribution. This is called the "condition of detailed balance". It is not a necessary condition for a Markov chain to have reversibility, but if it does, then there is definitely a stationary distribution. This is the reason why most MCMC algorithms satisfy the condition of detailed balance.

input : Starting point x_1, transition distribution $Q(y|x)$
output : An array of $x_1, x_2, ..., x_n$

for $t \leftarrow 1$ **to** n **do**
  $q \leftarrow \frac{p(y)Q(x_t|y)}{p(x_t)Q(y|x_t)}$ `// This line is generally expensive;`
  $r \leftarrow R \sim [0, 1]$ sample a uniform random variable r;
  if $r \leq q$ **then**
    $x_{t+1} \leftarrow y$;
    else $x_{t+1} \leftarrow x_t$;
  end
end

Algorithm 1: Metropolis-Hastings MCMC algorithm

When facing autocorrelation between the parameters, in some algorithms only the sequence from its k-th iteration is considered, so that the successive draws are approximately independent. This process is called "thinning". However, some believe that the thinning is unnecessary if you do not have any objection to keep the first to k-th iterations in your chain and an estimate from a thinned chain is never better than the original chain.

Traditional sampling methods do not converge quickly, especially if the dimension is large. However, an affine transformation can make the sampling from the proposal density easier. Moreover, using an ensemble sampler can solve the problem of tuning the proposal density. An ensemble sampler has multiple walkers (chains), which are running in parallel and are interacting so that they can adapt their proposal densities in a way that the Markov property is not violated. Emcee is a Python implementation of the affine-invariant ensemble sampler for the MCMC, originally suggested by Goodman & Weare (2010), informally called the "stretch move". A prime desirable feature of the algorithm is that, it needs hand tuning of only one or two parameters, compared to $\sim N^2$ parameters for a traditional algorithm, when one is dealing with a N-dimensional parameter space. The algorithm updates an ensemble of k walkers $S = x_k$ in a way that the proposal distribution for the walker k is based on the positions of the $k-1$ other walkers, which are in the complementary ensemble $S_{[k]} = x_j | \forall j \neq k$ (see Algorithm 2). In order to make the computation faster, one can split the ensemble into two subsets $S^{(0)} = x_k | \forall k = 1, 2, ..., K/2$ and $S^{(1)} = x_k | \forall k = K/2 + 1, ..., K$ and simultaneously evolve all the walkers in the first subset, using the Algorithm 2 based on the positions of the walkers in the other subset. Making use of the new positions of the walkers in the first subset, one can evolve the walkers in the second subset. This algorithm can be run in parallel and thus the inner loop of the Algorithm 2 is less computationally expensive.

for $k \leftarrow 1$ **to** K **do**
  Draw a random walker x_j from the complementary ensemble $S_{[k]}(t)$;
  $z \leftarrow Z$ a random variable drawn from distribution $g(Z = z)$;
  $y \leftarrow x_j + z[x_k(t) - x_j]$;
  $q \leftarrow z^{n-1} \frac{p(y)}{p(x_k(t)}$ `// This line is generally expensive`;
  $r \leftarrow R \sim [0, 1]$ sample a uniform random variable r;
  if $r \leq q$ **then**
    $x_{t+1} \leftarrow y$;
    else $x_{t+1} \leftarrow x_t$;
  end
end

Algorithm 2: Stretch Move MCMC Algorithm Used in Emcee

Where n is the dimension of the parameter space and $g(z)$ is suggested by Goodman & Weare (2010) as

$$g(z) = \begin{cases} \frac{1}{\sqrt{z}}, & \text{if } z \in \left[1\frac{1}{a}, a\right], \\ 0, & \text{otherwise.} \end{cases}$$

Here I show some of the histograms of MCMC simulations, which are reported in Table 2.6. Since the parameter space has a large dimension, I cut each of the 2D histograms into three parts: top-left, bottom-left, and right.

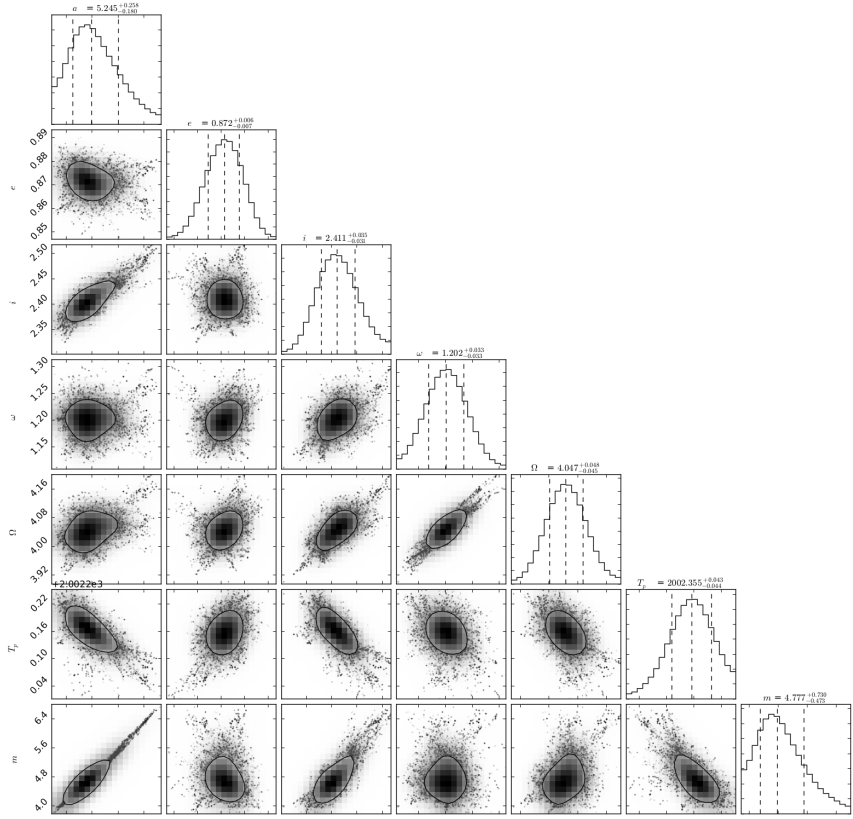

***Figure 5.1**: Top-left part of the probability density function for the fit to S2 using the MCMC method and a Newtonian model. Each panel shows a two-dimensional cut of the parameter space. The posterior probability distribution is compact. The marginalized distribution for each parameter is shown independently in the histograms along the diagonal. The contours show the 1σ uncertainties and the dashed lines show the 0.16, 0.5, and 0.84 quantiles. Here, a is the semimajor axis in mpc; i, Ω, and ω are inclination, longitude of ascending node, and argument of periapse in rad; T_p is the time of the periapse passage in yr; and m is the mass of the SMBH in $10^6 M_\odot$.*

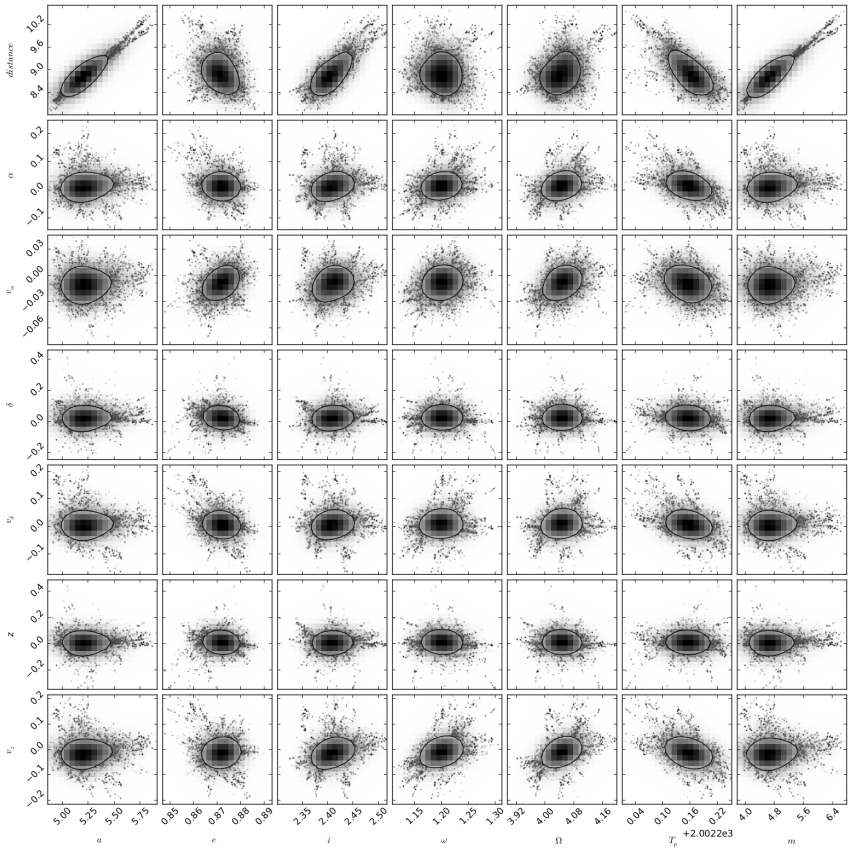

Figure 5.2*: Bottom-left part of the previous figure (Fig. 5.1). Here, a is the semimajor axis in mpc; i, Ω, and ω are inclination, longitude of ascending node, and argument of periapse in rad; T_p is the time of the periapse passage in yr; m is the mass of the SMBH in $10^6 M_\odot$; the distance to the GC is in kpc; α, δ, and z are the initial R.A., Dec. and z of the black hole in mpc; and v_α, v_δ, and v_z are the initial velocity of the blak hole in R.A., Dec., and z directions in mpc yr^{-1}.*

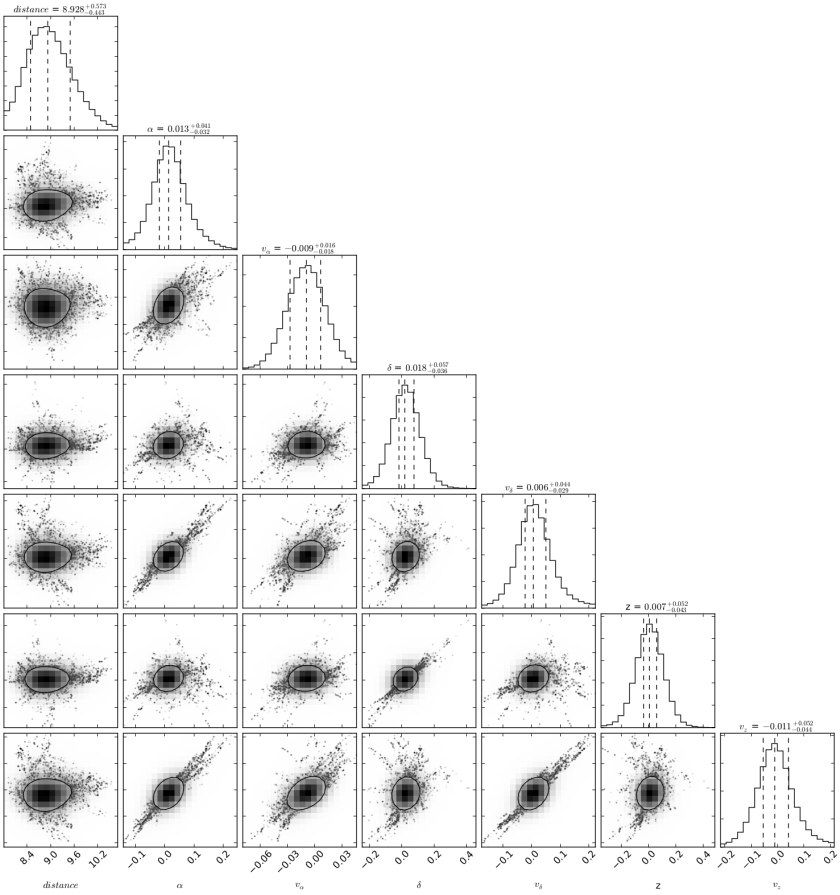

Figure 5.3*: Right part of the previous figures (Figs. 5.1 and 5.2). The distance to the GC is in kpc; α, δ, and z are the initial R.A., Dec. and z of the black hole in mpc; and v_α, v_δ, and v_z are the initial velocity of the black hole in R.A., Dec., and z directions in mpc yr^{-1}.*

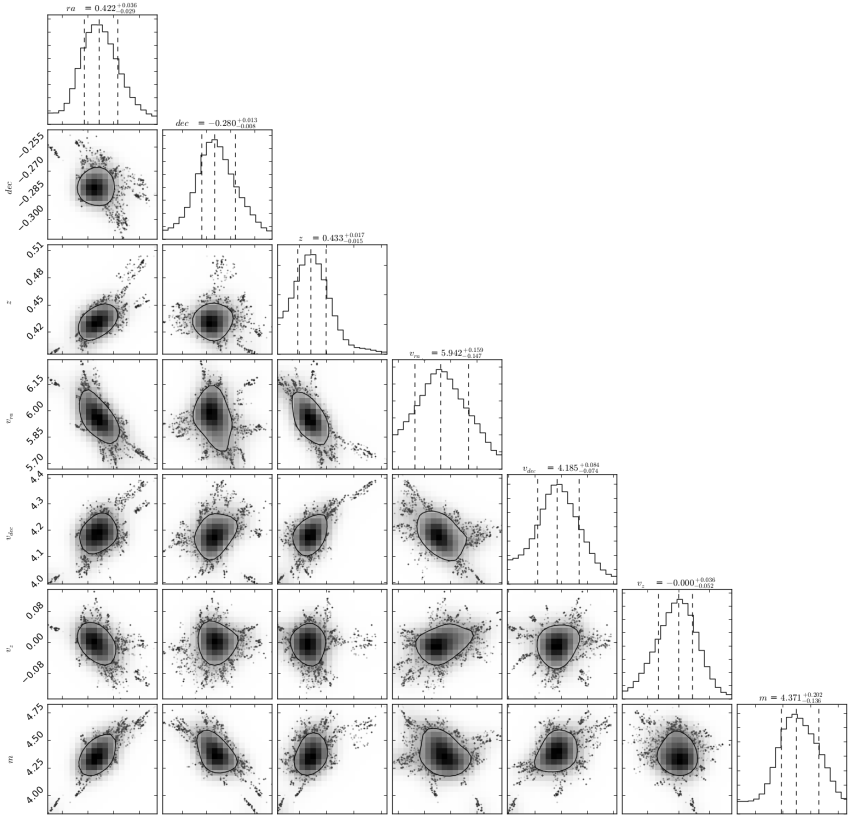

Figure 5.4*: Top-left part of the probability distribution function for the fit to S2 using MCMC simulations and a post-newtonian (relativistic) model. Each panel shows a two-dimensional cut of the parameter space. The posterior probability distribution is compact. The marginalized distribution for each parameter is shown independently in the histograms along the diagonal. The contours show the 1σ uncertainties and the dashed lines show the 0.16, 0.5, and 0.84 quantiles. Here, ra, dec, and z are the initial R.A., Dec., and z of S2 in mpc; v_{ra}, v_{dec}, and v_z are the initial velocity of S2 in R.A., Dec., and z directions in km s^{-1}; and m is the mass of the SMBH in $10^6 M_\odot$.*

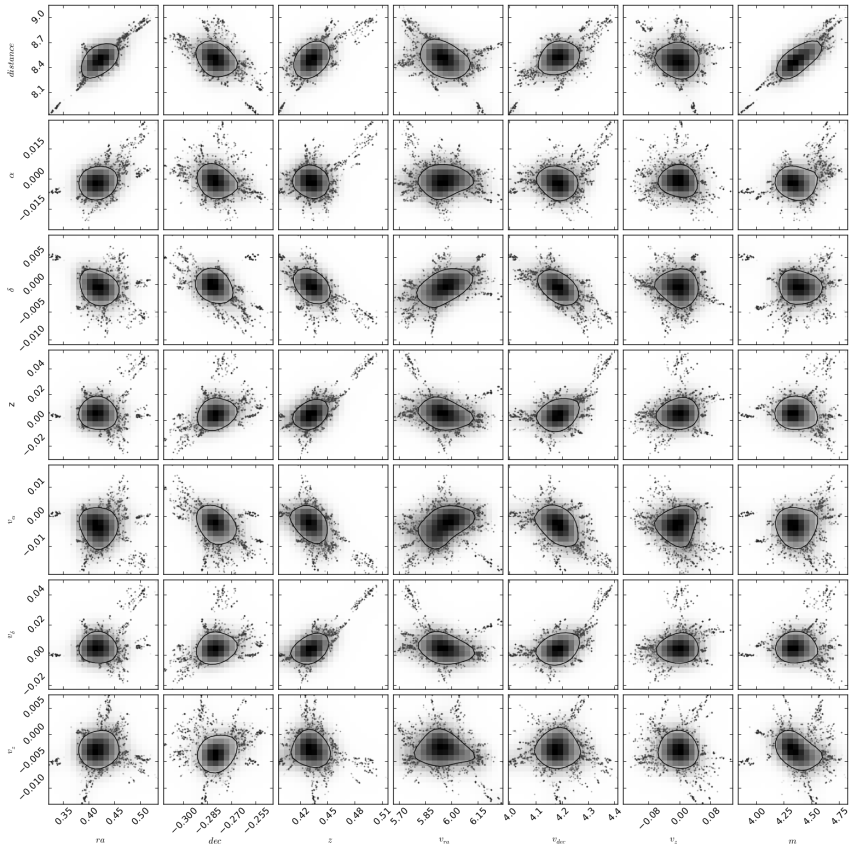

***Figure 5.5**: Bottom-left part of the previous figure (Fig, 5.4). Here, ra, dec, and z (in the x-axis) are the initial R.A., Dec., and z of S2 in mpc; v_{ra}, v_{dec}, and v_z (in the x-axis) are the initial velocity of S2 in R.A., Dec., and z directions in km s^{-1}; m is the mass of the SMBH in $10^6 M_\odot$; the distance to the GC is in kpc; α, δ, and z (in the y-axis) are the initial R.A., Dec. and z of the black hole in mpc; and v_α, v_δ, and v_z (in the y-axis) are the initial velocity of the black hole in R.A., Dec., and z directions in mpc yr^{-1}.*

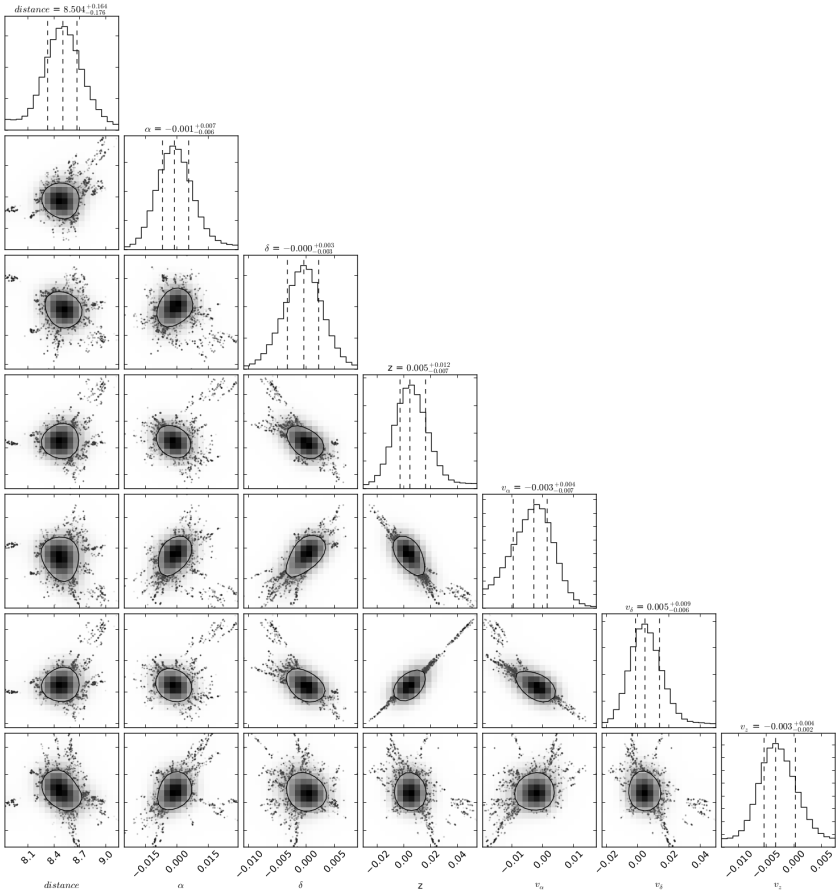

Figure 5.6*: Right part of the previous figures (Figs. 5.4 and 5.5). The distance to the GC is in kpc; α, δ, and z are the initial R.A., Dec. and z of the black hole in mpc; and v_α, v_δ, and v_z are the initial velocity of the black hole in R.A., Dec., and z directions in mpc yr^{-1}.*

Bibliography

Alexander, T. 2001, ApJ, 553, L149

Alexander, T. 2005, Phys. Rep., 419, 65

Alexander, T. 2011, in Astronomical Society of the Pacific Conference Series, Vol. 439, The Galactic Center: a Window to the Nuclear Environment of Disk Galaxies, ed. M. R. Morris, Q. D. Wang, & F. Yuan, 129

Alexander, T. 2017, ArXiv e-prints [arXiv:1701.04762]

Alexander, T. & Sternberg, A. 1999a, ApJ, 520, 137

Alexander, T. & Sternberg, A. 1999b, ApJ, 520, 137

Amaro-Seoane, P. & Chen, X. 2014, ApJ, 781, L18

Angélil, R. & Saha, P. 2014, MNRAS, 444, 3780

Angélil, R., Saha, P., & Merritt, D. 2010, ApJ, 720, 1303

Baker, T., Psaltis, D., & Skordis, C. 2015, ApJ, 802, 63

Balick, B. & Brown, R. L. 1974, ApJ, 194, 265

Bartko, H., Martins, F., Trippe, S., et al. 2010, ApJ, 708, 834

Becklin, E. E., Gatley, I., & Werner, M. W. 1982, ApJ, 258, 135

Boehle, A., Ghez, A. M., Schödel, R., et al. 2016, ApJ, 830, 17

Bower, G. C., Goss, W. M., Falcke, H., Backer, D. C., & Lithwick, Y. 2006, ApJ, 648, L127

Brandl, B. R., Agócs, T., Aitink-Kroes, G., et al. 2016, in Proc. SPIE, Vol. 9908, Ground-based and Airborne Instrumentation for Astronomy VI, 990820

Brown, W. R. 2015, ARA&A, 53, 15

Buchholz, R. M., Schödel, R., & Eckart, A. 2009, A&A, 499, 483

Davies, R., Schubert, J., Hartl, M., et al. 2016, in Proc. SPIE, Vol. 9908, Ground-based and Airborne Instrumentation for Astronomy VI, 99081Z

Diolaiti, E., Bendinelli, O., Bonaccini, D., et al. 2000, A&AS, 147, 335

Do, T., Ghez, A. M., Morris, M. R., et al. 2009, ApJ, 703, 1323

Eatough, R., Lazio, T. J. W., Casanellas, J., et al. 2015, Advancing Astrophysics with the Square Kilometre Array (AASKA14), 45

Eckart, A. & Genzel, R. 1996, Nature, 383, 415

Eckart, A. & Genzel, R. 1997, in Bulletin of the American Astronomical Society, Vol. 29, American Astronomical Society Meeting Abstracts, 1366

Eckart, A., Genzel, R., Ott, T., & Schödel, R. 2002, MNRAS, 331, 917

Eckart, A., Moultaka, J., Viehmann, T., Straubmeier, C., & Mouawad, N. 2004, ApJ, 602, 760

Eckart, A., Mužić, K., Yazici, S., et al. 2013, A&A, 551, A18

Eckart, A., Sabha, N., Witzel, G., et al. 2012, in Proc. SPIE, Vol. 8445, Optical and Infrared Interferometry III, 84451F

Eckart, A., Schödel, R., Moultaka, J., et al. 2005, in American Institute of Physics Conference Series, Vol. 783, The Evolution of Starbursts, ed. S. Hüttmeister, E. Manthey, D. Bomans, & K. Weis, 17–25

Efron, B. 1982, The Jackknife, the Bootstrap and other resampling plans

Einstein, A. 1915, Sitzungsberichte der Königlich Preußischen Akademie der Wissenschaften (Berlin), Seite 844-847.

Einstein, A., Infeld, L., & Hoffmann, B. 1938, Annals of Mathematics, 39, 65

Eisenhauer, F., Genzel, R., Alexander, T., et al. 2005a, ApJ, 628, 246

Eisenhauer, F., Genzel, R., Alexander, T., et al. 2005b, ApJ, 628, 246

Eisenhauer, F., Perrin, G., Brandner, W., et al. 2011, The Messenger, 143, 16

Eisenhauer, F., Schödel, R., Genzel, R., et al. 2003, ApJ, 597, L121

Falcke, H., Goss, W. M., Matsuo, H., et al. 1998, ApJ, 499, 731

Falcke, H., Melia, F., & Agol, E. 2000, ApJ, 528, L13

Ferrarese, L. 2002, ApJ, 578, 90

Ferrarese, L. & Merritt, D. 2000, ApJ, 539, L9

Figer, D. F. 2003, Astronomische Nachrichten Supplement, 324, 255

Figer, D. F., Rich, R. M., Kim, S. S., Morris, M., & Serabyn, E. 2004, ApJ, 601, 319

Fraga-Encinas, R., Mościbrodzka, M., Brinkerink, C., & Falcke, H. 2016, A&A, 588, A57

Fragile, P. C. & Mathews, G. J. 1999, in Bulletin of the American Astronomical Society, Vol. 31, American Astronomical Society Meeting Abstracts #194, 969

Freitag, M., Amaro-Seoane, P., & Kalogera, V. 2006, ApJ, 649, 91

Fried, D. L. 1966, Journal of the Optical Society of America (1917-1983), 56, 1380

Gebhardt, K., Bender, R., Bower, G., et al. 2000, ApJ, 539, L13

Genzel, R., Eisenhauer, F., & Gillessen, S. 2010, Reviews of Modern Physics, 82, 3121

Genzel, R., Schödel, R., Ott, T., et al. 2003, ApJ, 594, 812

Gerhard, O. 2001, ApJ, 546, L39

Ghez, A. M., Becklin, E., Duchjne, G., et al. 2003, Astronomische Nachrichten Supplement, 324, 527

Ghez, A. M., Klein, B. L., Morris, M., & Becklin, E. E. 1998, ApJ, 509, 678

Ghez, A. M., Morris, M., Becklin, E. E., Tanner, A., & Kremenek, T. 2000, Nature, 407, 349

Ghez, A. M., Salim, S., Hornstein, S. D., et al. 2005, ApJ, 620, 744

Ghez, A. M., Salim, S., Weinberg, N. N., et al. 2008, ApJ, 689, 1044

Gillessen, S., Eisenhauer, F., Fritz, T. K., et al. 2009a, ApJ, 707, L114

Gillessen, S., Eisenhauer, F., Trippe, S., et al. 2009b, ApJ, 692, 1075

Gillessen, S., Genzel, R., Fritz, T. K., et al. 2013a, ApJ, 763, 78

Gillessen, S., Genzel, R., Fritz, T. K., et al. 2013b, ApJ, 774, 44

Gillessen, S., Genzel, R., Fritz, T. K., et al. 2012, Nature, 481, 51

Gillessen, S., Plewa, P. M., Eisenhauer, F., et al. 2017, ApJ, 837, 30

Goddi, C., Falcke, H., Kramer, M., et al. 2017, International Journal of Modern Physics D, 26, 1730001

Goodman, J. & Weare, J. 2010, Communications in Applied Mathematics and Computational Science, Vol. 5, No. 1, p. 65-80, 2010, 5, 65

Graham, A. W. 2016, Galactic Bulges, 418, 263

Griv, E. 2010, in IAU Symposium, Vol. 267, Co-Evolution of Central Black Holes and Galaxies, ed. B. M. Peterson, R. S. Somerville, & T. Storchi-Bergmann, 330–330

Grould, M., Vincent, F. H., Paumard, T., & Perrin, G. 2016, Proceedings of the International Astronomical Union, 11, 25–30

Güsten, R. & Downes, D. 1980, A&A, 87, 6

Güsten, R., Genzel, R., Wright, M. C. H., et al. 1987, ApJ, 318, 124

Hansen, B. M. S. & Milosavljević, M. 2003, ApJ, 593, L77

Hastings, W. K. 1970, Biometrika, 57, 97

Hees, A., Do, T., Ghez, A. M., et al. 2017, Phys. Rev. Lett., 118, 211101

Herrnstein, R. M. & Ho, P. T. P. 2002, ApJ, 579, L83

Hills, J. G. 1988, Nature, 331, 687

Hopman, C. & Alexander, T. 2006, ApJ, 645, 1152

Iorio, L. 2011, Phys. Rev. D, 84, 124001

Iorio, L. 2017, ArXiv e-prints [arXiv:1705.05471]

Iorio, L. & Zhang, F. 2017, ApJ, 839, 3

Jalali, B., Pelupessy, F. I., Eckart, A., et al. 2014, MNRAS, 444, 1205

Jaroszynski, M. 1998, **??**jnlActa Astron., 48, 653

Johannsen, T. 2016, Classical and Quantum Gravity, 33, 113001

Kennea, J. A., Burrows, D. N., Kouveliotou, C., et al. 2013, ApJ, 770, L24

Kerr, R. P. 1963, Phys. Rev. Lett., 11, 237

Kocsis, B. & Tremaine, S. 2011, MNRAS, 412, 187

Kopeikin, S. M. & Ozernoy, L. M. 1999, ApJ, 523, 771

Kormendy, J. & Ho, L. C. 2013, ARA&A, 51, 511

Levin, Y. & Beloborodov, A. M. 2003, ApJ, 590, L33

Löckmann, U., Baumgardt, H., & Kroupa, P. 2009, MNRAS, 398, 429

Lucy, L. B. 1974, AJ, 79, 745

Madigan, A.-M., Levin, Y., & Hopman, C. 2009, ApJ, 697, L44

Martins, F., Genzel, R., Hillier, D. J., et al. 2007, A&A, 468, 233

Martins, F., Gillessen, S., Eisenhauer, F., et al. 2008, ApJ, 672, L119

Merritt, D., Alexander, T., Mikkola, S., & Will, C. M. 2010, Phys. Rev. D, 81, 062002

Metropolis, N., Rosenbluth, A. W., Rosenbluth, M. N., Teller, A. H., & Teller, E. 1953, J. Chem. Phys., 21, 1087

Metropolis, N. & Ulam, S. 1949, Journal of the American Statistical Association, 44, 335

Meyer, L., Ghez, A. M., Schödel, R., et al. 2012, Science, 338, 84

Mezger, P. G., Duschl, W. J., & Zylka, R. 1996, A&A Rev., 7, 289

Mezger, P. G., Zylka, R., Philipp, S., & Launhardt, R. 1999, A&A, 348, 457

Milosavljević, M. & Loeb, A. 2004, ApJ, 604, L45

Milosavljević, M., Merritt, D., Rest, A., & van den Bosch, F. C. 2002, MNRAS, 331, L51

Mori, K., Gotthelf, E. V., Zhang, S., et al. 2013, ApJ, 770, L23

Morris, M. 1993, ApJ, 408, 496

Morris, M., Ghez, A. M., & Becklin, E. E. 1999, Advances in Space Research, 23, 959

Mouawad, N., Eckart, A., Pfalzner, S., et al. 2005, Astronomische Nachrichten, 326, 83

Mužić, K., Schödel, R., Eckart, A., Meyer, L., & Zensus, A. 2008, in Journal of Physics Conference Series, Vol. 131, Journal of Physics Conference Series, 012016

Nayakshin, S. & Cuadra, J. 2005, A&A, 437, 437

Newman, E. T., Couch, E., Chinnapared, K., et al. 1965, Journal of Mathematical Physics, 6, 918

Nordström, G. 1918, Proc. Amsterdam Acad., 20, 1238

Oyama, T., Miyoshi, M., Deguchi, S., Imai, H., & Shen, Z.-Q. 2008, PASJ, 60, 11

Parsa, M., Eckart, A., Shahzamanian, B., et al. 2017, ApJ, 845, 22

Paumard, T., Genzel, R., Martins, F., et al. 2006, ApJ, 643, 1011

Perets, H. B. 2011, in Astronomical Society of the Pacific Conference Series, Vol. 439, The Galactic Center: a Window to the Nuclear Environment of Disk Galaxies, ed. M. R. Morris, Q. D. Wang, & F. Yuan, 172

Perets, H. B., Hopman, C., & Alexander, T. 2007, ApJ, 669, 661

Pfuhl, O., Gillessen, S., Eisenhauer, F., et al. 2015, ApJ, 798, 111

Philipp, S., Zylka, R., Mezger, P. G., et al. 1999, A&A, 348, 768

Plewa, P. M., Gillessen, S., Eisenhauer, F., et al. 2015, MNRAS, 453, 3234

Plewa, P. M., Gillessen, S., Pfuhl, O., et al. 2017, ApJ, 840, 50

Rauch, K. P. & Tremaine, S. 1996, New Ast., 1, 149

Reid, M. J., Menten, K. M., Trippe, S., Ott, T., & Genzel, R. 2007, ApJ, 659, 378

Reissner, H. 1916, Annalen der Physik, 355, 106

Richardson, W. H. 1972, Journal of the Optical Society of America (1917-1983), 62, 55

Rubilar, G. F. & Eckart, A. 2001, A&A, 374, 95

Sabha, N., Eckart, A., Merritt, D., et al. 2012, A&A, 545, A70

Schneider, M. 1996, Himmelsmechanik. Band III: Gravitationstheorie. (Spektrum Akademischer Verlag)

Schödel, R., Ott, T., Genzel, R., et al. 2003, ApJ, 596, 1015

Schödel, R., Ott, T., Genzel, R., et al. 2002, Nature, 419, 694

Schwarzschild, K. 1916, Abh. Konigl. Preuss. Akad. Wissenschaften Jahre 1906,92, Berlin,1907, 1916

Serabyn, E. & Morris, M. 1996, Nature, 382, 602

Shahzamanian, B., Eckart, A., Valencia-S., M., et al. 2015, A&A, 576, A20

Shahzamanian, B., Zajaček, M., Valencia-S., M., et al. 2017, in IAU Symposium, Vol. 322, The Multi-Messenger Astrophysics of the Galactic Centre, ed. R. M. Crocker, S. N. Longmore, & G. V. Bicknell, 233–234

Shapiro, I. I. 1964, Physical Review Letters, 13, 789

Sjouwerman, L. O., Messineo, M., & Habing, H. J. 2004, PASJ, 56, 45

Tremaine, S., Gebhardt, K., Bender, R., et al. 2002, ApJ, 574, 740

Valencia-S., M., Eckart, A., Zajaček, M., et al. 2015, ApJ, 800, 125

Weinberg, N. N., Milosavljević, M., & Ghez, A. M. 2005, ApJ, 622, 878

Weinberg, S. 1972, Gravitation and cosmology: principles and applications of the general theory of relativity, Vol. 1 (Wiley New York)

Will, C. M. 1993, Theory and Experiment in Gravitational Physics (Cambridge University Press), 396

Will, C. M. 2008, ApJ, 674, L25

Will, C. M. & Maitra, M. 2017, Phys. Rev. D, 95, 064003

Witzel, G., Eckart, A., Bremer, M., et al. 2012, ApJS, 203, 18

Witzel, G., Ghez, A. M., Morris, M. R., et al. 2014, ApJ, 796, L8

Yelda, S., Ghez, A. M., Lu, J. R., et al. 2014, ApJ, 783, 131

Zajaček, M., Valencia-S., M., Shahzamanian, B., et al. 2017, in IAU Symposium, Vol. 322, The Multi-Messenger Astrophysics of the Galactic Centre, ed. R. M. Crocker, S. N. Longmore, & G. V. Bicknell, 231–232

Zhang, F. & Iorio, L. 2017, ApJ, 834, 198

Zhang, F., Lu, Y., & Yu, Q. 2015, ApJ, 809, 127

Zucker, S., Alexander, T., Gillessen, S., Eisenhauer, F., & Genzel, R. 2006, ApJ, 639, L21

List of Figures

1.1 IR image of the GC from the Spitzer Space Telescope . . . 3
1.2 Dynamical Components in the GC Close to Sgr A* . . . 5
1.3 Multi-Wavelength Image of the GC . . . 6
1.4 NIR Image of the Central Parsec of the GC . . . 7
1.5 S-stars with known orbits . . . 9
1.6 Keplerian Orbital Elements . . . 11
1.7 VLT . . . 16
1.8 Principle of the Adaptive Optics . . . 18
1.9 Lucy-Richardson Deconvolution of the Central Arcsec of the GC . . . 21

2.1 Positions of the SiO Masers in the NIR K_s-band . . . 26
2.2 Locations of the Reference Stars in the NACO 13 mas pix^{-1} Image in 2011 28
2.3 Locations of the Overlapping Stars in the NACO 27 mas pix^{-1} Image in 2011 . . . 29
2.4 Single Epoch Statistics for the Offset Between the Infrared and Radio Positions. . . . 30
2.5 Location of S2, S38, and S0-102/S55 in the K_s-band Between 2002 and 2005 . . . 32
2.6 Location of S2, S38, and S0-102/S55 in the K_s-band Between 2006 and 2009 . . . 33
2.7 Location of S2, S38, and S0-102/S55 in the K_s-band Between 2010 and 2013 . . . 34
2.8 Location of S2, S38, and S0-102/S55 in the K_s-band in 2015 . . . 35
2.9 Proper Motion of the NIR Counterpart of Sgr A* . . . 37
2.10 Relativistic Orbit of S2, S38, and S55/S0-102 . . . 42
2.11 Results of the MCMC Simulations for Gravitational Potential Parameters of the SMBH . . . 45

3.1 Comparison between the Newtonian and the Post-Newtonian Orbits . 50
3.2 Comparison Between the Newtonian and Relativistic Orbits with Respect to the Orbital Phase . . . 51
3.3 Distribution of the S-stars and the Simulated Stars . . . 52
3.4 Correlation Between Υ and the Ratio of the Goodness of the Fit . . . 55
3.5 Applied Method for the Observation of the PN Effects Using the Squeezed State . . . 56
3.6 Method for the Observation of the PN Effects by Means of Measuring $\Delta\omega$ 58
3.7 Comparison Between the Methods . . . 59

3.8 Comparison Between the Post-Newtonian and the Newtonian Fit to the Combined Data Set of S2 . . . 60
3.9 Correlations Between Υ and the Orbital Parameters . . . 62
3.10 Correlation Between Υ and the Relativistic β at the Periapse . . . 63
3.11 Correlation Between Υ and the Changes in the Semimajor Axis . . . 65
3.12 Correlation Between Υ and the Changes in the Eccentricity . . . 66
3.13 Correlation Between Υ and the Changes in the Argument of Periapse . 67

5.1 Results of MCMC for S2 Using Newtonian Model (1) . . . 80
5.2 Results of MCMC for S2 Using Newtonian Model (2) . . . 81
5.3 Results of MCMC for S2 Using Newtonian Model (3) . . . 82
5.4 Results of MCMC for S2 Using Post-Newtonian Model (1) . . . 83
5.5 Results of MCMC for S2 Using Post-Newtonian Model (2) . . . 84
5.6 Results of MCMC for S2 Using Post-Newtonian Model (3) . . . 85

List of Tables

1.1 CONICA List of the Cameras . . . 17

2.1 List of the Observations . . . 25
2.2 Equation of Motion of the Reference Stars . . . 36
2.3 Astrometric Measurements of S2 . . . 38
2.4 Astrometric Measurements of S38 . . . 39
2.5 Astrometric Measurements of S0-102/S55 . . . 40
2.6 Results of the MCMC Simulations . . . 46

3.1 Simulated Stars . . . 49
3.2 Relativistic Parameter of S2 at the Periapse . . . 68

List of Acronyms

AO Adaptive Optics

AGN Active Galactic Nuclei

BH Black Hole

CDF Cumulative Distribution Function

CND Circum-Nuclear Disk

DM Deformable Mirror

DSO Dusty S-cluster Object

E-ELT European Extremely Large Telescope

EHT Event Horizon Telescope

ESO European Southern Observatory

FoV Field of View

GC Galactic Center

GMC Giant Molecular Cloud

GR General Relativity

GW Gravitational Wave

HVS Hypervelocity Star

IMBH Intermediate Black Hole

IR Infrared

kpc kilo parsec

LF Luminosity Function

LGS Laser Guide Star

NSC Nuclear Star Cluster

NS Neutron Star

mad Median Absolute Deviation

mas milliarcsecond

MCMC Markov Chain Monte Carlo

mpc milli parsec

NACO Nasmyth Adaptive Optics System/Coude Near Infrared Camera

NIR Near-Infrared

pc parsec

PDF Point Spread Function

PN Post-Newtonian

PSF Point Spread Function

rms Root Mean Square

RTC Real-Time Computer

RR Resonant Relaxation

SR Strehl Ratio

Sgr A* Sagittarius A*

SKA Square Kilometre Array

SMBH Supermassive Black Hole

UV Ultraviolet

VLBI Very Long Baseline Interferometry

VLT Very Large Telescope

VLTI Very Large Telescope Interferometer

WF Wavefront

WFS Wavefront Sensor

WD White Dwarf

YSO Young Stellar Object

Acknowledgements

I would first like to give my thanks and express my gratitude to my supervisor, Prof. Dr. Andreas Eckart, who was there continuously to aid me from my first days of my PhD work. I thank him for all the support in all aspects from the guidance in my project to helping me planning my present and future, interesting scientific career, for all the encouragement and providing me with the opportunity to work on an enchanting topic. Especially I would like to thank him for all our exciting morning discussions and great ideas without which I could not conclude my work.

Thanks to Prof. Dr. Andreas Eckart, Prof. Dr. J. Anton Zensus, Dr. Behrang Jalali, for being members of my IMPRS PhD thesis committee. This work is partially supported by the International Max Planck Research School (IMPRS) for Astronomy and Astrophysics at the MPIfR and the Universities of Bonn and Cologne. Thanks to Prof. Dr. Vladimir Karas for the Cologne-Prague exchange programm and his suggestions and fruitful discussions. I thank the IMPRS coordinator Priv.-Doz. Dr. Rainer Mauersberger and Dr. Simone Pott for organizing state of the art and useful blackboard lectures in particular the statistical methods lectures, which was my motivation in applying new statistical methods in my project.

I am grateful to Dr. Banafsheh Shahzamanian who introduced me to observation and observational data and helped me with the data reduction. For her time and readiness to answer all my questions. Also, my thanks to Dr. Nadeen Sabha and Dr. Banafsheh Shahzamanian for teaching me about observation with the Very Large Telescope NACO instrument and to Florian Peißker for introducing me to observations in practice on our trip to Chile. I thank Dr. Lydia Moser and Dr. Semir Smajic for their support during my first year of PhD work and introducing me to the working procedures in the work group.

I am grateful to all my colleagues in the aegroup for all their support and the friendly and positive atmosphere, for the friendly chats, the technical support, and helping with German translation especially Dr. Gerold Bosch, Dr. Semir Smajic and Dr. Lydia Moser without whom I could not find accommodations in Cologne. I thank all my past and present friendly officemates, especially Dr. Lydia Moser and Nastaran Fazeli who made me feel comfortable everyday. I am thankful to Matthias Subroweit for all the intersting statistical discussions. Thanks to Dr. Gerold Bosch and Michal Zajacek for the scientific discussions and their suggestions. I am also grateful to the secretaries of the 1. Physikalisches Institut for their assistance, which made all the bureaucratic procedure go more smoothly.

I thank all my friends in Cologne who made these three years of my life full of joy, for all the moments we spent together, for all the chats and lunches and cakes and cookies we shared together. Thanks For all the support during sickness and problems and stressful times and for all the encouragements during desperate times.

I thank my highschool friends with whom I made an oath to get a PhD in physics before I am thirty.

A special thanks goes to Dr. Banafsheh Shahzamanin, Dr. Nadeen Sabha, Dr. Gerold Busch, Nastaran Fazeli, Dr. Semir Smajic, Matthias Subroweit, and Fabio Eupen for their comments and suggestions about the contents of this thesis.

Last but not least, I would like to thank my family for all their support and encouragements to follow what I am passionate about. For my Mother who gave me lenses and prisms and magnets as gifts when I was a child and sparked my interest in physics. And finally, I thank Dr. Semir Smajic for being patient and supportive and encouraging. For listening to me every night and understanding. For being with me in my most joyful and stressful times of my PhD.

Selbständigkeitserklärung

Ich versichere, dass ich die von mir vorgelegte Dissertation selbständig angefertigt, die benutzten Quellen und Hilfsmittel vollständig angegeben und die Stellen der Arbeit – einschließlich Tabellen, Karten und Abbildungen –, die anderen Werken im Wortlaut oder dem Sinn nach entnommen sind, in jedem Einzelfall als Entlehnung kenntlich gemacht habe; dass diese Dissertation noch keiner anderen Fakultät oder Universität zur Prüfung vorgelegen hat; dass sie – abgesehen von unten angegebenen Teilpublikationen – noch nicht veröffentlicht worden ist, sowie, dass ich eine solche Veröffentlichung vor Abschluss des Promotionsverfahrens nicht vornehmen werde. Die Bestimmungen der Promotionsordnung sind mir bekannt. Die von mir vorgelegte Dissertation ist von Prof. Dr. Andreas Eckart betreut worden.

Köln, den 16.04.2018

(Marzieh Parsa)

Teilpublikationen

- *Investigation the Relativistic Motion of the Stars Near the Suppermassive Black Hole in the Galactic Center*; **M. Parsa**, A. Eckart, B. Shahzamanian, V. Karas, M. Zajaček, J. A. Zensus, C. Straubmeier; ApJ 845, 22 (2017).

Weitere Publikationen

- *Nature of the Galactic centre NIR-excess sources. I. What can we learn from the continuum observations of the DSO/G2 source?*; M. Zajaček, S. Britzen, A. Eckart, B. Shahzamanian, G. Busch, V. Karas, **M. Parsa**, F. Peißker, M. Dovčiak, M. Subroweit, F. Dinnbier, J. A. Zensus; A&A 602, A121 (2017).

- *Detection of polarized continuum emission of the Dusty S-cluster Object (DSO/G2)*; B. Shahzamanian, M. Zajaček, M. Valencia-S., F. Peißker, A. Eckart, N. Sabha, **M. Parsa**; The Multi-Messenger Astrophysics of the Galactic Centre, Proceedings of the International Astronomical Union, IAU Symposium 322 (2017).

- *Nature of the Dusty S-cluster Object (DSO/G2): Pre-main-sequence star with non-spherical dusty envelope*; M. Zajaček, M. Valencia-S., B. Shahzamanian, F. Peißker, A. Eckart, A. **M. Parsa**; The Multi-Messenger Astrophysics of the

Galactic Centre, Proceedings of the International Astronomical Union, IAU Symposium 322 (2017).

- *Polarized near-infrared light of the Dusty S-cluster Object (DSO/G2) at the Galactic center*; B. Shahzamanian, A. Eckart, M. Zajaček, M. Valencia-S., N. Sabha, L. Moser, **M. Parsa**, F. Peißker, C. Straubmeier; A&A 593, A131 (2016).

- *Nuclear Activity and the Conditions of Starformation at the Galactic Center*; A. Eckart, M. Valencias-S, B. Shahzamanian, M. Zajaček, L. Moser, **M. Parsa**, M. Subroweit, F. Peißker, N. Sabha, M. Horrobin, C. Straubmeier, A. Borkar, D. Kunneriath, V. Karas, C. Rauch, S. Britzen, J. A. Zensus, M. Garcia-marin; PoS-SISSA Proceedings of the Frontier Research in Astrophysics – II (2016).

- *Experimental Indicators of Accretion Processes in Active Galactic Nuclei*; A.Eckart, M. Valencias-S., B. Shahzamanian, M. Zajacek, L. Moser, G. Busch, **M. Parsa**, M. Subroweit, F. Peißker, N. Sabha, S. E. Hosseini, M. Horrobin, C. Straubmeier, N. Fazeli, A. Borkar, D. Kunneriath, V. Karas, C. Rauch, S. Britzen, J. A. Zensus, M. Garcia-Marin, Y. E. Rashed; Proceeding of Accretion Processes in Cosmic Sources - APCS2016 (2016).

- *Monitoring the Dusty S-cluster Object (DSO/G2) on its Orbit toward the Galactic Center Black Hole*; M. Valencia-S,; A. Eckart, M. Zajaček, F. Peißker, **M. Parsa**, N. Grosso, E. Mossoux, D. Porquet, B. Jalali, V. Karas, S. Yazici, B. Shahzamanian, N. Sabha, R. Saalfeld, S. Smajić, R. Grellmann, L. Moser, M. Horrobin, A. Borkar, M. García-Marín, M. Dovčiak, D. Kunneriath, G. D. Karssen, M. Bursa, C. Straubmeier, H. Bushouse; ApJ 800, 125 (2015).

- *Variable and Polarised Near-infrared Emission from the Galactic Centre*; B. Shahzamanian, A. Eckart, M. Valencia-S., G. Witzel, M. Zamaninasab, M. Zajaček, N. Sabha, M. García-Marín, V. Karas, F. Peißker, G. D. Karssen, **M. Parsa**, N. Grosso, E. Mossoux, D. Porquet, B. Jalali, M. Horrobin, R. Buchholz, M. Dovčiak, D. Kunneriath, M. Bursa, J. A. Zensus, R. Schödel, J. Moultaka, C. Straubmeier; The Messenger 159 (2015).

- *The Center of the Milky Way from Radio to X-rays*; A. Eckart, M. Valencia-S., B. Shahzamanian, M. García-Marín, F. Peißker, M. Zajaček, **M. Parsa**, B. Jalali, R. Saalfeld, N. Sabha, S. Yazic, G. D. Karssen, A. Borkar, K. Markakis, J. A. Zensus, C. Straubmeier; PoS-SISSA Proceedings of the Frontier Research in Astrophysics Workshop (2014).

Lebenslauf

Persönliche Angaben

Name:	Marzieh Parsa
Anschrift:	I.Physikalisches Institut, Universität zu Köln Zülpicher Str. 77, 50937 Köln, Deutschland
Email:	parsa@ph1.uni-koeln.de
Geburtsdatum und -ort:	25.01.1988 in Shiraz, Iran
Staatsangehörigkeit:	Iranisch

Ausbildung

Seit 2014	Promotionsstudium (Experimentalphysik), Universität zu Köln und Max-Planck-Institut für Radioastronomie wissenschaftlicherin Mitarbeiter (WMA) am I. Physikalischen Institut
2011 - 2013	Master of Science (Physik), Eastern Mediterranean Universität, Famagusta, Zypern
2006 - 2011	Bachelor of Science (Physik), Khaje Nasir Universität der Technologie, Tehran, Iran

Stipendium

2015 - 2017	Stipendium der International Max Planck Research School (*IMPRS*) of Astronomy and Astrophysics